CZECH TECHNICAL UNIVERSITY IN PRAGUE
FACULTY OF MECHANICAL ENGINEERING
DEPARTMENT OF MATERIALS ENGINEERING

MASTER THESIS

PLASMA SPRAYING OF CERAMICS COATINGS FOR HIGH TEMPERATURE TRIBOLOGICAL APPLICATIONS

AUTHOR: Kristýna Petelová

STUDY PROGRAM: Double Degree of Material and Production Engineering

SUPERVISOR: Ing. Ladislav Cvrček, Ph. D.

                   Dr. Ir. Husaini Ardy

PRAGUE 2018

ČVUT

ČESKÉ VYSOKÉ
UČENÍ TECHNICKÉ
V PRAZE

ZADÁNÍ DIPLOMOVÉ PRÁCE

I. OSOBNÍ A STUDIJNÍ ÚDAJE

Příjmení: **Petelová**   Jméno: **Kristýna**   Osobní číslo: **408787**

Fakulta/ústav: **Fakulta strojní**

Zadávající katedra/ústav: **Ústav materiálového inženýrství**

Studijní program: **Strojní inženýrství**

Studijní obor: **Výrobní a materiálové inženýrství**

II. ÚDAJE K DIPLOMOVÉ PRÁCI

Název diplomové práce:

Plazmový nástřik keramických povlaků pro vysokoteplotní tribologické aplikace

Název diplomové práce anglicky:

Plasma spraying of ceramics coatings for high temperature tribological applications

Pokyny pro vypracování:

High temperature applications in abrasive and corrosive aggressive environment require chemically stable and wear resistant surfaces. Plasma spraying coatings based on oxides (for example Al2O3, Cr2O3, TiO2, ZrO2) will be deposited on heat resistant P91 steels. The effect of increased temperature on wear and microstructure of coatings will be tested using the high temperature pin-on-disk tribometer.
Approach:
1. Literature review, 2. Preparation of the test samples from alloy P91 and plasma spraying of oxide coatings,
3. High-temperature tribological tests with increasing temperatures up to 750 °C, 4. Evaluation of structure, mechanical and chemical properties at dependence on increasing temperature, 5. Results and discussion

Seznam doporučené literatury:

[1] P.L. Fauchais, Thermal spray fundamentals: from powder to part, Springer Science, New York, 2013.
[2] N. Cinca, J.M. Guilemany, Thermal spraying of transition metal aluminides: An overview, Intermetallics. 24 (2012) 60-72.
[3] G. Bolelli, A. Candeli, L. Lusvarghi, T. Manfredini, A. Denoirjean, S. Valette, et al., 'Hybrid' plasma spraying of NiCrAlY+Al2O3 + h -BN composite coatings for sliding wear applications, Wear. 378-379 (2017) 68-81.

Jméno a pracoviště vedoucí(ho) diplomové práce:

Ing. Ladislav Cvrček, Ph.D.,   ústav materiálového inženýrství   FS

Jméno a pracoviště druhé(ho) vedoucí(ho) nebo konzultanta(ky) diplomové práce:

Dr. Ir. Ardy Husaini,   Bandung Institute of Technology, Faculty of Mechanical and Aerospace Engineering, Bandung Institute of Technology (FMAE ITB)

Datum zadání diplomové práce: **03.04.2018**   Termín odevzdání diplomové práce: **30.07.2018**

Platnost zadání diplomové práce: _____

_____
Ing. Ladislav Cvrček, Ph.D.
podpis vedoucí(ho) práce

_____
prof. RNDr. Petr Špatenka, CSc.
podpis vedoucí(ho) ústavu/katedry

_____
prof. Ing. Michael Valášek, DrSc.
podpis děkana(ky)

III. PŘEVZETÍ ZADÁNÍ

Diplomantka bere na vědomí, že je povinna vypracovat diplomovou práci samostatně, bez cizí pomoci, s výjimkou poskytnutých konzultací.
Seznam použité literatury, jiných pramenů a jmen konzultantů je třeba uvést v diplomové práci.

_____1. 4. 2018_____
Datum převzetí zadání

_____
Podpis studentky

Declaration

I declare that I have done this work independently and solely using the sources and literature listed in the list of cited sources.

In Prague on: ...30.7. 2018...

....
Signiture

Anotace

Tato diplomová práce se zaměřuje na plazmou stříkané keramické povlaky pro vysokoteplotní tribologické aplikace. Budou uvedeny různé materiály pro vysokoteplotní tribologické aplikace. Bude popsán vodou stabilizovaný plasmatický nástřik. Budou popsány keramické materiály a jejich vlastnosti. Opotřebení plazmou nanášených keramických povlaků bude testováno při různých teplotách od pokojové teploty až do 750 ° C. Bude hodnocen vliv vysokých teplot na vlastnosti opotřebení.

Klíčová slova

Plazma, keramika, povlaky, vysoké teploty, opotřebení, odolnost, povlakování

Annotation:

This master thesis focuses on the plasma sprayed ceramic coatings for high temperature tribological applications. Different materials for high temperature tribological applications will be listed. Water-stabilized plasma spraying will be described. Ceramic materials and their properties will be described. Wear behavior of plasma sprayed ceramic coatings will be tested at different temperatures from room temperature up to 750 °C. The influence of high temperature on wear properties will be evaluated.

Key words:

Plasma, ceramics, coatings, high temperature, wear, resistant, spraying

Acknowledgement

I would like to thank to my parents, who made me finish the started work, who supported me. Special thanks to my father, who helped me with the technical side of study a lot.

TABLE OF CONTENTS

1. INTRODUCTION

The aim of this thesis is to evaluate tribological properties of different plasma sprayed ceramic coatings tested at different temperatures.

Tribological applications have high demands on the material properties, especially if they are used at high temperatures. These materials need to withstand abrasive or erosive wear and corrosion. High demands have nuclear and space industries, energy sectors or transportation industry. The applications can be for example superheater boiler tubes, oil- or coal-fired steam turbines in power plants, fusion reactors or turbines in aerospace industry. These applications work up to around 700 °C, sometimes even more. There are present also corrosive, abrasive and erosive media in these applications such as CO, CO_2, SO_2, SO_3, SO_4, NO_X gases, Al_2O_3, SiO_2, Fe_2O_3, CaO, SiC and others. [1, 2, 3]

The heat resistant high-alloy steels can be used as a base material. These steels have good hot-strength properties and excellent creep resistance. These steels have high content of chromium and nickel. The steels are usually austenitic, and the stability of austenite is enhanced by addition of nitrogen. Heat resistant high-alloy steels are for example A 376, A 213, B 407 or B 167. [4]

To enhance the properties of the steel, the coatings can be used. There are many types of coatings as metal coatings, composite coatings or ceramic coating, which can withstand high temperatures and abrasive environment.

Especially ceramics are interesting choice since they form oxidic layer, which is chemically stable and thus corrosion resistant. Ceramics have unique combination of properties. They have good mechanical properties as strength and hardness and excellent wear resistance.

Coatings, which were chosen for testing in this thesis are Al_2O_3, Al_2O_3- 40 TiO_2, $ZrSiO_4$, $ZrSiO_4$-Y_2O_3, Olivine and composite $NiCr$-Cr_2O_3. The last two coatings, mineral olivine and composite $NiCr$-Cr_2O_3 were chosen for comparison between different types of coatings.

The coatings will be plasma sprayed on heat resistant steel T91 (P91). Plasma spraying is the most suitable method to apply the ceramics. Ceramics have high melting temperatures and plasma spraying works with temperatures around 24 000 °C.

Thickness of plasma sprayed coating can vary from 0.1 mm up to 1 mm, but usually used thickness is from 0.3 to 0.7 mm. All depends on the purpose of the coating.

The wear test at different temperatures was chosen to simulate the corrosive-wear environment. The test will be performed at 23 °C, 200 °C, 400 °C, 600 °C and 750 °C.

The $ZrSiO_4$ coating is standardly used as protective coating against high temperatures. The $ZrSiO_4$-Y_2O_3 will be tested, since the Y_2O_3 has stabilizing effect on ZrO_2. This could improve the wear resistance of $ZrSiO_4$ at higher temperatures.

2. THEORETICAL PART

2.1 WATER-STABILIZED PLASMA SPRAYING

There are many types of thermal coating methods such as oxy-fuel wire spray, oxy-fuel powder spray, electric arc wire spray, high velocity oxy-fuel spraying, plasma spraying and others. However, plasma spraying is the most suitable method for ceramics since it provides high temperatures necessary for melting ceramic materials.

There are various applications of plasma sprayed coatings. The applications are chosen according to the different mechanical, chemical, thermal and other properties. The coating properties, which have the highest influence on the mechanical properties are: thickness, porosity, microstructure, number of unmelted particles, oxides and impurities, heterogeneity, cracks and bond strength. [5] Varying of plasma spraying parameters has high influence on the final structure of the coatings. Main parameters for final structure of the coating are the temperature, velocity and the size of the powder particles. [6] To obtain the best properties of the coatings, continuous research of plasma spraying is needed.

All the powder particles should be melted during plasma spraying. These melted particles have a shape of droplets. When they hit the surface of the base material, they will flatten into splats. Heat of the melted particles is absorbed by the substrate. The droplets cool down quickly. The cooling rate of this process is around 10^6 K/s. Unmelted particles do not stick to the substrate. They could be caught to the substrate by other melted particles. Partially melted particles adhere to the coating. However, they have more spherical shape than the splats from melted particles. [6]

The structure contains two interfaces. The first interface is a transition between two lamellae and the second one is a structure inside the lamellae caused by the solidification. [6]

The thermally sprayed coatings have porosity in the range of a few percent up to about 20 %. The increase of plasma power input can lower the size of pores from 3-10 µm to 0.1 µm for aluminum coatings. A schematic structure of plasma sprayed coating is shown in the Pic. 1. [6]
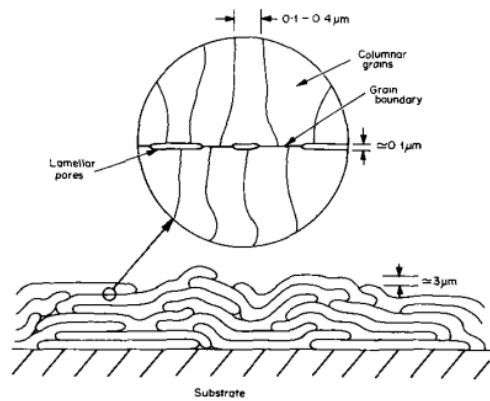
Pic. 1 Schematic picture of sprayed coating structure [6]

The Water-stabilized plasma (WSP®-H 500) spraying is an improved method, in comparison to gas-stabilized plasma (GSP) spraying. Water-stabilized plasma torch (hybrid plasma torch) combines stabilization of plasma torch by water and gas stream. Water-stabilized plasma torch has a very high plasma enthalpy up to 272 MJ/kg. The gas-stabilized plasma torch has its plasma enthalpy around 25 MJ/kg. [7] This improvement increases powder feed rates up to few tens of kg/h. Also, high throughput ability is expected. Plasma density of WSP is lowered from 0.0292 kg/m^3 to 0.0027 kg/m^3. However, the velocity is increased from 1-2 km/s to 5-7 km/s. [8, 7, 9] The WSP has also low consumption of argon. It starts from 12 slpm. The consumption of water is 3 l/h. Power varies from 80 to 160 kW. Current is from 300 to 550 A. Temperature of plasma is up to 24 700 °C. Continual burning lasts up to 12 hours. The Water-stabilized plasma is shown in the Pic. 2.
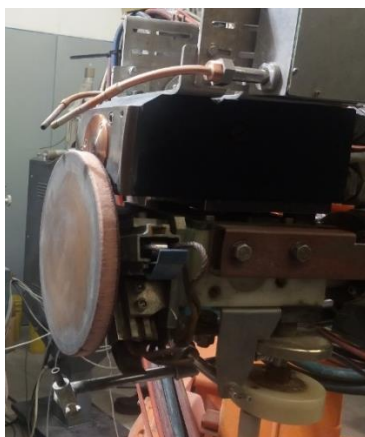
Pic. 2 Water-stabilized plasma WSP®-H 500

2.2 MATERIALS

2.2.1 SUBSTRATE MATERIAL

T91/P91

ASTM A213 T91 Standard covers seamless ferritic and austenitic steel tubes used for boilers, superheaters and heat-exchanger. Tubes from this material are widely used in many industrial spheres such as oil and gas, power, fertilizers, heat-exchangers, paper and pulp, pharmaceuticals, chemicals, water treatment etc. ASTM A213 T91 tubes shall be made by seamless process and hot finished or cold finished. Immediately after hot forming, they can be quenched in water or oil. [10] Hot forming of the steel is performed at temperature from 1100 °C up to 950 °C. Austenitization takes place at 920-980°C, annealing at 680-760 °C. The resulting structure is bainitic/ferritic. The annealing temperature must be held through the whole cross-section for at least 30 minutes. Stress relieving annealing is at 600-650 °C. The holding time should be minimum 30 minutes plus 1-2 minutes per mm plate thickness. [10]

There are three types of this steel. There is T91, P91 and X10CrMoVNb9-1. There is small difference in chemical composition. These differences are shown in the Tab. 1. Mechanical properties of these steel variants are shown in the Tab. 2.

Tab. 1 Chemical Composition of P91 (T91, X10CrMoVNb9-1) according to ASTM A213 [11]

Name	P91	T91	X10CrMoVNb9-1
UNS Designation/Material No.	K91560/	K90901/	/1.4903
Carbon	0.08-0.12	0.07-0.14	0.08-0.12
Silicon	0.20-0.50	0.20-0.50	0.20-0.50
Manganese	0.30-0.60	0.30-0.60	0.30-0.60
Phosphorus	≤0.020	≤0.020	≤0.020
Silicon	≤0.010	≤0.010	≤0.010
Aluminum	≤0.040	≤0.020	≤0.040
Chromium	8.0-9.5	8.0-9.5	8.0-9.5
Molybdenum	0.85-1.05	0.85-1.05	0.85-1.05
Nickel	≤0.040	≤0.040	≤0.040
Vanadium	0.18-0.25	0.18-0.25	0.18-0.25
Nitrogen	0.030-0.070	0.030-0.070	0.030-0.070
Niobium	0.06-0.1	0.06-0.1	0.06-0.1
Copper	-	-	≤0.30

Tab. 2 Mechanical properties for ASTM A213 T91, P91, X10CrMoVNb9-1 [11]

Material	P91	T91	X10CrMoVNb9-1
Tensile strength [MPa]	585≤	585≤	620-850
Yield strength min. [MPa]	415	415	415
Elongation min. [%]	20[2)4)]	20[2)4)]	19[2)]
Impact energy (KV)	-	-	40 (20°C)

[2)]Longitudinal test piece
[4)]For wall thicknesses ≤ 8 mm the values of the transverse test piece apply

Other properties of T91/P91/ X10CrMoVNb9-1 are written in the
Attachment 1,
Attachment 2, Attachment 3 (yield strength at different temperatures) and
Attachment 4 (physical properties).

2.2.2 COATINGS

The steel P91 can be coated by many types of material. Different coatings have different impact on the resulting mechanical and chemical properties of the steel. Coatings for this type of steel should ensure better high temperature corrosion resistance and oxidation resistance. For example, coatings used for heat transfer applications, Accelerator Driven System (ADS) or Generation IV nuclear concepts need to be compatible with liquid metals. In this case, four different coatings, applied with CVD technique, can be used. First is a superficial $M_{23}C_6$ (M=Cr+Fe) compound covering a thick layer of $Cr_{1-y}Fe_y$ (0<y<weight %) solid solution. Second is a superficial layer of $(Fe,Cr)_2B$ compound over (Fe,Cr,B) one. Another possibility is single layer of FeAl or thin layer of $FeAl_3$ covering thick layer of Fe_2Al_5 under which a FeAl layer grows afterwards. [12]

First two coatings are ceramic and are very stable in high temperatures but are also sensitive to oxidation when oxygen is present in working space. During isothermal annealing in air at 815°C, the iron solid solution, enriched in chromium and covered by $M_{23}C_6$ carbide coating, forms a protective Cr_2O_3 layer with slow growing rate, around 50 h. For iron boride coating, a mix, $(Fe,Cr)_2O_3$, appears after 4 h. For the second two, the presence of aluminum allows spontaneous formation of alumina protective layer in low oxygen environment. T91 steel was normalized at 1050 °C, air quenched and

6

tempered at 750 °C for 1 h. For the first two coatings, the forming temperature of the aluminum-based coating is 650 °C. This temperature is lower than transformation temperature of the tempered T91 steel. There is no heat treatment needed after this coating. For the second two coatings the formation temperature (950 °C and 980 °C) is higher than the transformation temperature of T91. This changes the phase composition in the steel. Standard heat treatment needed to be performed because of this. [12]

Other standard coating materials are Cr_3C_2-NiCr and WC-Co. Problem with WC-Co is usually in higher working temperatures from 550 °C up to 650 °C, where the corrosion starts easier. Coating Cr_3C_2-NiCr can also corrode when it is sprayed with wrong parameters of plasma spraying. Better is to spray with HVOF technology. [13]

Now standardly used coatings for boiler pipes, which work in elevated temperatures, are also NiCr, FeCr, TAFA 95MXC, and Inconel 625 [14]

Other coating materials applied with plasma spraying for increased wear resistance are Mo/Ni-Cr-B-Si and Ni-Cr-B-Si. [84]

The Ni-Cr-B-Si coating has good corrosion resistance. It is caused by protective oxide layers. Chromium oxide and silicon oxide forms along the boundaries of splats. Those oxides are blocking the entry of other corrosive media. This coating resists also to high temperature corrosion. The corrosion usually starts along the boundaries of the splats. Thanks to high number of splats in the coating, the distance from surface to the base material is long. That ensures the lower corrosion. This coating has higher corrosion resistance than Stellite 6. The coating is dense, compact, and does not show any cracking. Heat treatment can lower the porosity. [15]

Other coatings, which can be plasma sprayed are [84]:

- Mo/Ni-Cr-B-SiC
- Titan oxide
- Chromium oxide
- Aluminum oxide
- Aluminum oxide (Al_2O_3) + Titan oxide (TiO_2) 97/3
- Aluminum oxide (Al_2O_3) + Titan oxide (TiO_2) 87/13

The Al_2O_3 + TiO_2 (97/3) coating has a good corrosion resistance, wear resistance, heat shock resistance, good electrical insulating properties. The Al_2O_3 + TiO_2 (87/13) coating has good corrosion resistance, relative high ductility and hardness. [84]

- Zirconium dioxide (ZrO_2) + Calcium oxide (CaO) 90/10

The ZrO_2 + CaO (90/10) coating has good wear and oxidation resistance. [84]

- Chromium oxide (Cr_2O_3) + Titan oxide (TiO_2) + Silicon oxide (SiO_2) 92/3/5

The Cr_2O_3 + TiO_2 + SiO_2 (92/3/5) coating has high wear resistance, high corrosion and oxidation resistance. [84]

- Zirconium oxide (ZrO_2) + Magnesium oxide (MgO) 97/3

The ZrO_2 + MgO (97/3) coating has good wear resistance and oxidation resistance at elevated temperatures. The Cr_3C_2 coating has similar properties. [84]

- Boron carbide (B_4C)/Ni
- Silicon carbide (SiC)

Boron carbide has high hardness, heat resistance up to 1000°C and consumes neutron radiation. Silicon carbide has also high hardness and is heat resistant up to 1500°C. [84]

- Tungsten carbide (WC) + Titan carbide (TiC) 85/15

The WC + TiC (85/15) coating is corrosion resistant. [84]

- Tungsten carbide (WC) +cobalt (Co) 94/6

The WC + Co (94/6) coating has high hardness, is partially corrosion resistant and abrasion resistant. When WC + Co is applied on base material, it is dissolved first. WC and Co go through an oxidation process before dissolution. The oxidation of WC to WO_3 causes accelerated dissolution of cobalt and corrosion of hard phase, leading to its removal. The corrosion of this material is very complex and corrosion rate increases with temperature. [16]

- Tungsten carbide
- Al-Al_2O_3

The Al-Al_2O_3 has improved wear and corrosion resistance. [84]

- Stellite 6

The Stellite 6 (CoCrWC) coating provides good corrosion resistance through formation of silicon oxides and chromium oxides. Also, the $CoCr_2O_4$ is good diffusion barrier through the Cobalt oxide (CoO) and (Co_3O_4). The corrosion rate of the coating is high at the first few cycles. After repeating another cycle, the corrosion rate decreases and stabilizes. [84]

I. OLIVINE

Olivine is a naturally occurring mineral, magnesium iron silicate $(Mg,Fe)_2SiO_4$. It composes of a solid solution of magnesium ortho silicate (forsterite - Mg_2SiO_4) and iron ortho silicate (fayalite - Fe_2SiO_4). It is the iron, that causes the green color of olivine. Olivine crystals are angular with sharp edges. [18] Properties of olivine are written in the Tab. 3

Tab. 3 Properties of Olivine

Density [g·cm^{-3}]	From 3.2 (forsterite) to 4.4 (fayalite) [19]
Melting temperature [°C]	1760 (1900 (forsterite), 1200 (fayalite)) [18]
Thermal expansion coefficient [µm·m^{-1}·K^{-1}]	9.7 [20]
Thermal conductivity [W·m^{-1}·K^{-1}]	2.65 [21]
Micro-hardness [GPa]	10 [22]

Olivine is soluble in HNO_3. The composition of olivine is usually 25.37 wt. % of magnesium, 14.57 wt. % of iron, 18.32 wt. % of silicon and 41.74 wt. % oxygen. Usually distributed as follows: 42.06 % MgO, 18.75 % FeO and 39.19 % SiO_2. Olivine has very brittle fracture producing small, conchoidal fragments. [19] It has good insulating properties due to low heat conductivity. It is essentially inert and has a high chemical stability. [18] Olivine coatings sprayed by water stabilized plasma were observed to prolong fatigue life of the steel substrate. [22]

Annealing can be used for the plasma sprayed olivine coatings to change properties, if needed. The temperature of annealing is from 850 to 1250°C. After annealing, coating gets fully crystalline. Forsterite-fayalite partly transforms to other phases such as protoenstatite $MgSiO_3$ and ferro-periclase $MgFe_2O_4$. The quantity of transformed phases grows with increasing annealing temperature. Protoenstatite crystallizes from amorphous structure first. If the coating is Fe-rich, after annealing at 1400 °C, also the magnetite phase (Fe_3O_4) can form. [22]

Properties of olivine coating sprayed by water-stabilized plasma were already examined in Prague. Two types of olivine were tested, Mongolian and Norwegian. These two powders varied by purity. Olivine coatings were applied with feed stock around 22-24 kg/hour, stand-off distance 450 mm and feeding distance 90 mm. Powder size was about 63-125 μm. Substrate was preheated to 250 °C. [22]

Wear resistance was measured by the slurry abrasion response method (SAR). It is expressed in Inverse wear rate (IWR). It represents a distance passed by the samples in the slurry to remove one cubic millimeter of the coating. Accuracy of measurement is ± 5 %. For the Norwegian coating the inverse wear rate was 62.8 m/mm^3 for the Mongolian coating the was the inverse wear rate 85 m/mm^3. [22]

Microhardness for Norwegian coating was 10.65 ± 1.43 GPa. The microhardness for Mongolian coating was 8.72 ± 1.24 GPa. [22]

Mg_2SiO_4:

Forsterite (Mg_2SiO_4) is a magnesium-rich member of olivine minerals. It is an orthosilicate ceramic compound with a melting temperature of ~1900°C. It has been found, that plasma-sprayed forsterite coatings have a high coefficient of thermal expansion (CTE) value (11 x 10^{-6} /°C) comparable to that of some metals (steel-13.5 x 10^{-6} /°C). Because of the high CTE, this coating has smaller mismatch with metallic substrates and adheres better to it. [23]

When forsterite is plasma sprayed to the substrate, it is cooled very quickly. This process makes the final structure of forsterite amorphous. Crystallinity of the coating is much lower than of the starting powder. The crystallinity of the coating can be enhanced by preheating the substrate. Then the cooling rate is not as high and there is more time for the crystallization. [22]

The forsterite is now investigated again for plasma-spraying as potential inter-layer coating between the metallic substrate and the spinel or mullite top coats to be used in thick thermal barrier coatings. It was also determined that an in-flight particle history and a residence time of forsterite powder, of different sizes, in the plasma plume has a major effect on the microstructure of the coating. Finer particles of powder are preferable for plasma spraying. Large particles do not melt completely, and the coating contains voids and other structural defects leading to high porosity. To improve the

powder feeding, the powder can be heated up to 1200 °C for 2 hours in air. It strengthens the agglomerates and the flowability of the powder. [23]

The influence of the forsterite powder size on resulting microstructure was investigated. The powder size of three different coatings are shown in the Tab. 4. The coatings were plasma-sprayed on grit-blasted 3x3 inch mild steel substrate. In-flight particle diagnostic measured the temperature necessary for the particles to melt. The temperature was above 2600 °C. Particles velocity was about 390 m/s. The plasma spray process parameters are listed in the *Attachment 5*. The coating temperature was monitored with pyrometer and held below 150 °C. [23]

Tab. 4 Powder granulometries used to deposit forsterite coatings and identification of the coatings analyzed [23]

Powder granulometry	Size distribution; d_{50} (median) [μm]	Coating
A	-160+44; 116	Forsterite A
B	-86+1; 16	Forsterite B
C	-53+1; 15	Forsterite C

The SEM micrograph pictures show the microstructure of the sprayed coatings. The microstructure type-A forsterite is shown in the Attachment 6 (a). The coating appeared to adhere well on the substrate but was highly porous. The coating had large amount of un-melted and partially melted particles that are indicated by arrows. Structure of A forsterite powder can be seen in the Attachment 6 (b). EDX analysis identified Mg, Si, Sr, O and C due to MgO, SiO_2, SrO and wax-like organic structure. Some of these particles were deposited during spraying and entered the coating. [23]

Coating B showed smaller amount of un-melted particles and less voids. The porosity present in coating B was 15%. The coating adhered also well and there were no vertical or horizontal cracks. This is shown in the Attachment 7 (a). The coating deposited on the pre-heated substrate via 5 passes of the torch (substrate temperature was about 350 °C) and with the use of different variant of cooling (276 kPa instead of 345 kPa) is shown in the Attachment 7 (b). The density did not improve significantly. The heated substrate reduces the amount of the amorphous phase entrapped in the coating due to prolonged time of quenching. [23]

The type-C forsterite exhibited the densest microstructure due to finest granulometry. This is shown in the Attachment 8. Porosity remained at higher level about 13 %. The type-C coatings had the highest degree of crystallinity. [23]

X-ray diffraction revealed a mixture of forsterite, enstatite ($MgSiO_3$), magnesium oxide (MgO) crystalline phase and also the amorphous $nMgO:mSiO_2$ glassy phase. The forsterite phase was obtained at about 58 wt.% MgO. If the powder particles are richer in MgO, droplets re-solidity on the side of the eutectic periclase (MgO)-forsterite (Mg_2SiO_4) (T~1850°C). If the powder is richer in SiO_2 a mixture of enstatite and SiO_2 is favored. These residual phases are unwanted. These phases are the result of melting the non-homogeneous and broad-sized powder particles during spraying process. [23]

II.   ZrSiO$_4$

ZrSiO$_4$ is a ceramic, which is chemically inert and stable to very high temperatures. [24] It has a moderately high tensile strength and a moderately high density, relative to other oxide-based engineering ceramics. [25]The ZrSiO$_4$ has excellent resistance to thermal shocks and good corrosion resistance. Properties of ZrSiO$_4$ are written in the Tab. 5. [25]

Tab. 5 Properties of ZrSiO$_4$ [24, 25]

Chemical composition	ZrO$_2$- 65.9 wt. % [24]
	SiO$_2$- 32 wt. % [24]
Molecular weight [g/mol]	183.1 [24]
Melting point [°C]	2200-2550 [24]
Mohs hardness	7.5-8 [24]
Thermal expansion coefficient [10^{-6}/K]	5 [25]
Density [g/cm^3]	From 3.9 to 4.56 [25]
Ultimate tensile strength [MPa]	290 [25]

When the ZrSiO$_4$ powder is plasma sprayed, it can decompose to ZrO$_2$ and SiO$_2$. The thermal dissociation of ZrSiO$_4$ appears at the temperature of 1673 ± 10 °C. At this temperature the ceramic decomposes by solid-state reaction releasing SiO$_2$. The SiO$_2$ is a metastable intermediate phase. Depending on impurities, the dissociation temperature can vary from 1285 to 1700 °C. The formation process of zircon (ZrO$_2$) should be only nucleation controlled, not diffusion controlled. The formation of ZrO$_2$ can be observed at 1200 °C after 13 hours of annealing. [26]

The phase diagram of ZrO$_2$-SiO$_2$ is shown in the Attachment 9.

The ZrO$_2$ can occur in three modifications [27]:

- Monoclinic (m-ZrO$_2$) – Density is 5.6 g/cm^3. This phase is thermodynamically stable at room temperature up to 950 °C. [27]
- Tetragonal (t- ZrO$_2$) – Density is 6.1 g/cm^3. This metastable phase can be achieved by transformation at 1150 °C from monoclinic phase. (transition start temperature). Transformation back to monoclinic phase ends with cooling to 950 °C. This is martensitic transformation with high hysteresis. When monoclinic phase transforms to tetragonal, zirconium becomes denser and volume decreases by 5 %. [27]

- Cubic (c- ZrO_2) – density is 6.1 g/cm^3. Transformation of this metastable phase occurs above 2300 °C. Hysteresis is about max. 30 °C. Cubic phase melts at 2700 °C. [27]

When ZrO_2 is cooled slowly, first the tetragonal structure appears under the 2400 °C. By further cooling under 900 °C, the monoclinic structure grows with significant volume change. [28]

The SiO_2 can appear in the form of α-quartz (trigonal crystal system), Tridymite (meaning alpha, triclinic crystal structure), Cristobalite (meaning alpha, tetragonal crystal structure), β-quartz (hexagonal crystal structure).

Production of $ZrSiO_4$ by sintering ZrO_2 – SiO_2:

A formation of $ZrSiO_4$ depends on a type of ZrO_2 used for sintering with SiO_2. If regular ZrO_2 is used for sintering, zircon can be found after 4 hours at 1200 °C. If yttria-stabilized ZrO_2 (is described in $ZrSiO_4$-Y_2O_3 part of this thesis) is used, no $ZrSiO_4$ is found after 6 hours at 1200 °C. Different types of SiO_2 have no effect on the starting temperature of zircon formation. The formation of small crystallites of $ZrSiO_4$ between ZrO_2 particles starts after 4 hours at 1200 °C. Large amount of Y-stabilized ZrO_2 particles transforms to $ZrSiO_4$ after 5 hours at 1500 °C. The newly formed zircon ($ZrSiO_4$) particles surround the residual zirconia dioxide (ZrO_2) particles. An interconnecting sinter necking can be observed. Residual amorphous silica is located between the zircon. This implies to diffusion reaction of ZrO_2-SiO_2. Formation of zircon ($ZrSiO_4$) is possible up to 1500 °C. At higher temperatures then 1500 °C, the amount of ZrO_2 starts to increase again. [26]

An increase of the substrate temperature before plasma spraying increases the amount of monoclinic zirconia, which was observed to occur after plasma spraying in the coating of $ZrSiO_4$. The amount of zircon is increased with preheating the substrate. [29]

Heat-treatment after plasma spraying at 1000 °C causes formation of small amount of monoclinic zirconia and zircon. These phases increase significantly after heat treatment at 1200 °C. Zircon becomes dominant phase after heat treatment at 1400 °C. [29]

A porosity can increase slightly after heat treatment at 1200 °C and significantly after heat treatment at 1400 °C due to high volume shrinkage. The porosity was also observed to decrease when heat treatment was done on coatings, which were sprayed on substrate with lower pre-heat temperature. This was seen up to 1200 °C. But porosity increased up to 10 % after heat treatment at 1400 °C, regardless the pre-heat temperature of the substrate. [29]

For the lower porosity of the coating it is possible to shorten the spraying distance, or to preheat the substrate. This causes smaller difference in temperature between the droplets and the substrate. Droplets have then longer time before solidification on the surface. They tend to spread wider on the substrate and create denser microstructure, meaning lower porosity. Also, the residual thermal stress is decreased and lower cracking in the coating is observed. [29]

Porosity of the plasma sprayed $ZrSiO_4$ is written in the *Tab. 6.* Phase composition changes were obtained by the X-ray diffraction method using Cu Kα radiation. The results are written in the Tab. 7. Change of Young's modulus is shown in the Attachment 10. The microstructure of plasma-sprayed $ZrSiO_4$ as sprayed and annealed for 3 hours at 1300 °C is shown in the Pic. 3. [30]

Tab. 6 Porosity of plasma sprayed $ZrSiO_4$ [30]

Annealing		Pore size distribution		
Temperature [°C]	Time [h]	Size [µm]	Portion [%]	Total range [µm]
As sprayed, no annealing		0.32-0.55	32	0.032-2.0
		0.55-1.0	22	
1100	2	0.32-0.55	30	0.032-2.5
		0.55-1.0	33	
1300	3	0.55-1.0	16	0.055-3.5
		1.0-1.8	45	

Tab. 7 Results of X-ray phase analysis for plasma-sprayed zirconium silicate. [30]

Annealing		Intensity ratio of phase changes	
Temperature [°C]	Time [h]	$ZrSiO_4$ to ZrO_2	t-ZrO_2 to m-ZrO_2
As sprayed	No annealing	0.01	2.92
1300	3	0.01	3.20
1400	1	1.35	0.15
1400	3	2.92	0.20
1400	9	3.55	0.15
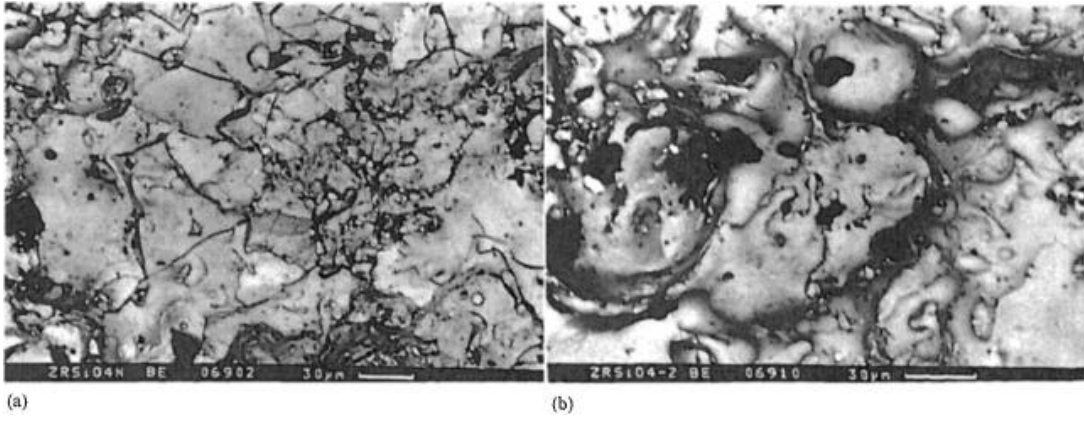
Pic. 3 Typical microstructure of plasma-sprayed ZrSiO₄; (a) as sprayed; (b) annealed for 3 h. at 1300 °C. [30]

III. $ZrSiO_4 + Y_2O_3$

The silicate $ZrSiO_4$ has high stability in oxidative and corrosive environment, low thermal expansion and low thermal conductivity. Problems with this material are the technologies for applying the coating. Plasma coating is suitable for refractory coatings with high melting point. However, $ZrSiO_4$ may decompose into SiO_2 and ZrO_2 during spraying process. The decomposition may be accompanied with volume shrinkage around 25 %. This causes formation of voids (up to 10 %). This causes the failure of the material. [28]

Zirconia ceramics are known for the characteristic, that their microstructure can be controlled by addition of cubic oxides as CaO, CeO_2, MgO, Y_2O_3. The amount, added to zirconia, can be changed, so that the tetragonal and cubic phases become stable at the room temperature. That means, that martensite start temperature (M_s) is decreased to ambient temperature. [27] M_s can be also reduced by decreasing grain size in the tetragonal ZrO_2 solid solution. Monoclinic transformation can later start by applying stress. This can increase the fracture toughness. [6]

Zirconia ceramics can be fully stabilized, partially stabilized and tetragonal. [27]

Cubic zirconia at room temperature is fully stabilized. Partially stabilized zirconia (PSZ) contains two phases: cubic grains with tetragonal and/or monoclinic precipitates. The PSZ composes of about 58 % cubic, 37 % tetragonal, 5% monoclinic phase and has usually about 8 % MgO or CaO. The tetragonal zirconia polycrystal can be formed by addition of 2-3 % Y_2O_3 or CeO_2 . [27]

The addition of Y_2O_3 will cause formation of Y_2O_3-stabilized ZrO_2 and SiO_2 during oxidation at 1550 °C. [28]

Addition of yttria to zircon powder shows improved stability of zircon coating at elevated temperatures. Silica and zirconia combined to produce zircon after heat treatment at 1200 °C. Higher amount of yttria lowered amount of zircon. This caused less open porosity of the coating at high temperatures. Coatings with the addition of yttria showed better adhesion to the substrate. [31]

The tetragonal ZrO_2 has higher thermal expansion coefficient and thermal conductivity then cubic phase. This structure is more thermal shock resistant on

superalloy substrates then cubic phase. The thermal shock resistance can be enhanced also by finely distributed porosities. [6]

Properties of Y_2O_3:

Properties of Y_2O_3 are written in the Tab. 8.

Tab. 8 Properties of Y_2O_3 [25]

Density [g·cm^{-3}]	5
Melting temperature [°C]	2440
Thermal expansion coefficient [µm·m^{-1}·K^{-1}]	8
Thermal conductivity [W·m^{-1}·K^{-1}]	0.3
Modulus of elasticity [GPa]	120
Specific heat capacity [J·kg^{-1}·K^{-1}]	440
Thermal diffusivity[m^2·s^{-1}]	0.14
Compression strength [MPa]	390

Different properties of $ZrSiO_4$ coatings prepared with different mole ratios of Y_2O_3 (5 mol%, 10 mol%, 15 mol% and 20 mol%) were obtained. This coating was sprayed on interlayer SiC. The size of the powder $ZrSiO_4$-Y_2O_3 was 10-15 µm.

During plasma spraying the powder $ZrSiO_2$ quickly melted and partly decomposed in air to ZrO_2 and SiO_2. The inner layer SiC was oxidized and produced glassy SiO_2. The glassy SiO_2 filled the micro-cracks in $ZrSiO_4$. In addition, the Y_2O_3 stabilized the ZrO_2 and reacted with SiO_2 to form $Y_2Si_2O_7$, which increased the oxidation resistance of the coating. From the XRD image could be seen, that intensities of $Y_2Si_2O_7$ increased with the Y_2O_3 content. When 5 % of Y_2O_3 was added, no $Y_2Si_2O_7$ was detected. Just two different phases of ZrO_2 (Y_2O_3 -stabilized tetragonal phase (t-ZrO_2) and Y_2O_3-stabilized cubic phase (c-ZrO_2) were detected. When the Y_2O_3 content increased the phase t-ZrO_2 decreased. Phase c-ZrO_2 remained the same. [28]

The resulting microstructure can be observed in the Pic. 4. The open porosity is shown in the Pic. 5. [28]
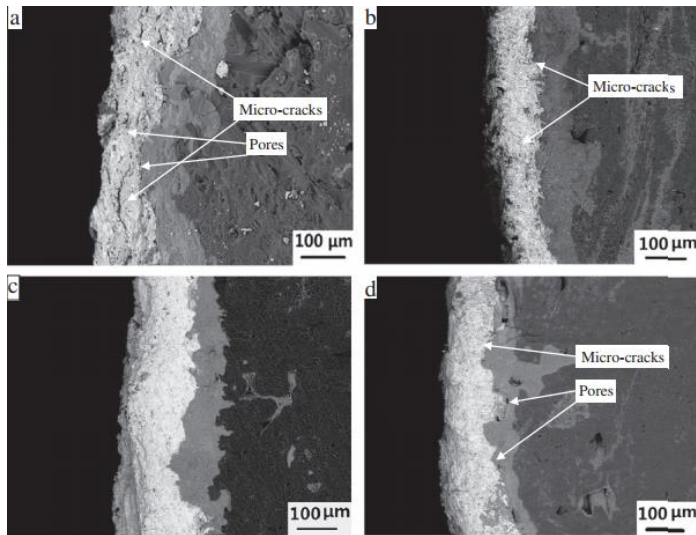
Pic. 4 Backscattered electron image of cross-section micrographs of $ZrSiO_4 - Y_2O_3$ coatings, sprayed on SiC interlayer, prepared at different Y_2O_3 mole ratios: (a) 5%, (b) 10%, (c) 15%, (d) 20% [28]
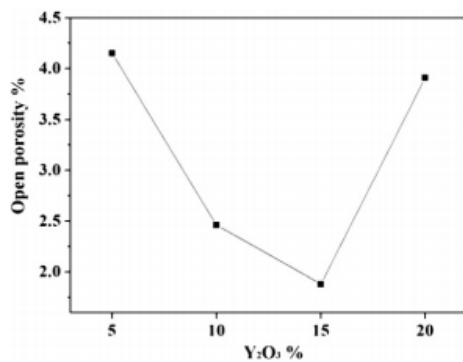
Pic. 5 Open porosity of $ZrSiO_4 - Y_2O_3$ coatings prepared at different Y_2O_3 mole ratios [28]

The behavior of the coatings $ZrSiO_4 - Y_2O_3$ with different mole ratio was tested at temperature 1550 °C. The coatings were heat treated before the test at 1600 °C for 2 hours. The specimens were thermally cycled at the temperature of 1600 °C for several hours. The oxidation stage of sample was observed. The pure $ZrSiO_4$ was taken as a reference. [28]

The $ZrSiO_4 - Y_2O_3$ (15 mol%) coating behavior was divided into two stages. At the first stage (less than 55 hours), the specimen exhibited mass increase. It was due to the existence of pores and microcracks, which where the entrance for the oxygen into the inner layer. [28]

The coating $ZrSiO_4 - Y_2O_3$ (15 mol%) exhibited the lowest mass increase in early 55 hours. After the oxidation for 210 hours at 1550 °C the mass loss was 1.54 %.

Coatings with different amount of Y_2O_3 then 15 % exhibited higher mass loss. The mass loss of the coatings is shown in the Pic. 6. [28]
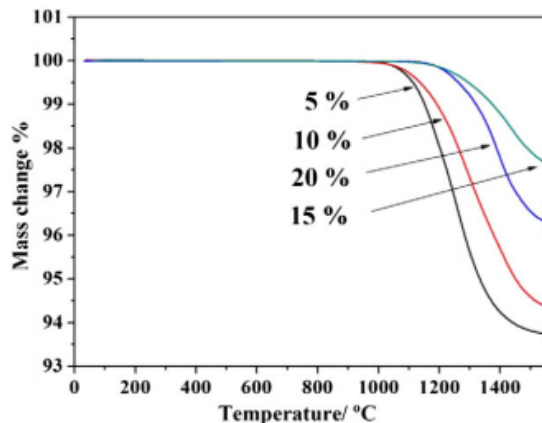
Pic. 6 The mass change of the coated specimens with different Y_2O_3 content in ZrSiO$_4$ in the air condition from room temperature to 1550 °C [28]

IV.   Al$_2$O$_3$

This Al_2O_3 ceramic material is probably the most used ceramic due to its low cost and good properties. The good properties are the result of strong ionic interatomic bonds. Aluminum oxide can exist in several crystalline phases, which revert to the most stable one, hexagonal alpha phase, at elevated temperatures. This phase is the strongest and stiffest of the oxide ceramics and consequently the most desired for many applications. The properties can vary based on purity of aluminum. Alumina of high purity can be used in oxidizing or reducing atmospheres to 1925 °C. It resists to all gases except wet fluorine. It is resistant to all reagents except the hydrofluoric acid and the phosphoric acid. It is degradable also in the presence of alkali metal vapors at elevated temperatures, especially, if the coating has lower purity. [33] Aluminum oxide can have quite high thermal conductivity and moderately high heat capacity compared to other oxide ceramics. Purer aluminum oxides have higher thermal conductivity in order of tens. Also, they have slightly higher coefficient of thermal expansion in tenths. [25] Properties of Al_2O_3 are written in the Tab. 9.

Tab. 9 Properties of Al_2O_3 [25, 34, 35]

Density [g/cm^3]	3.4-4.1
Hardness [GPa]	15-19
Hardness Vickers (HV50) [Kg/mm^2]	1600
Hardness HRC	60-70
Ultimate tensile strength [MPa]	210-630
Compressive strength [MPa]	1920-4000
Elastic modulus [GPa]	220-370
Specific heat capacity [J·kg^{-1}K^{-1}]	900
Fracture toughness [MPa/m^2]	3.7-7.2
thermal expansion [10^{-6}/°C]	6.7-8.2
Thermal conductivity [W·m^{-1}K^{-1}]	14-30
Maximum thermal shock °C	200-300
Maximum use temperature °C	1600-1700
Coefficient of friction	0.15-0.17 [36]
Melting point °C	2072

Al_2O_3 can occur in many phases. Most important are alpha and gamma. The α-Al_2O_3 phase is stable at room temperature. It has hexagonal close-packed structure. The γ-Al_2O_3 phase is metastable with cubic structure. [37]

The content of α-Al_2O_3 (stable phase) and γ-Al_2O_3 (metastable phase) depends on cooling rate. The crystallization of molten particles occurs by nucleation and growth. When the molten particles are undercooled by the impact to the substrate, the nucleation starts. Since the γ-Al_2O_3 has the lowest energy barrier to nucleation, it is the first one to nucleate. The as-sprayed alumina coatings usually contain γ-Al_2O_3 phase and at least small amount of α-Al_2O_3 phase. This can be because of the retained nuclei during the spraying. This can be influenced by spraying parameters. [6]

The γ-Al_2O_3 phase transformation to α-Al_2O_3 can be ensured by preheating the substrate. It can be also formed by additional heating of the sprayed coating. [38] The α-Al_2O_3 phase has higher density than γ-Al_2O_3 phase. That is why α-Al_2O_3 phase has higher thermal conductivity. [6] When γ-Al_2O_3 transforms to α-Al_2O_3, the volume decreases of about 15 %. This results in microcracking in the coatings. [39]

A torch power has the effect on coating microstructure. The coating Al_2O_3 was tested with the different torch power of 38.7, 42.0 and 45.8 kW. Average plasma temperature in the injection place of the powders was 4296.85 ± 50 °C, 4506.85 ± 50 °C and 4706.85 ± 50 °C, respectively. The mean plasma temperatures

and velocities at nozzle outlet were 4257 ± 50 °C, 4587 ± 50 °C and 4877 ± 50 °C and 1460 ± 25 m/s, 1530 ± 25 m/s and 1590 ± 25 m/s, respectively. The composition stayed the same with increased power. The roughness R_q of the coatings decreased from 5.05 µm to 4.40 µm and to 3.65 µm, respectively to the torch power. The γ-Al_2O_3 phase content increased from 15.0% to 16.5% and 18.3%, respectively. The content of β-Al_2O_3 also increased from 28.3% to 34.6% and 41.2%, respectively. The α-Al_2O_3 content decreased. [40]

The increase of the β- Al_2O_3 phase indicates, that most of the powders were melted and because of the sodium existence, the α-Al_2O_3 phase transformed to β- Al_2O_3 phase during the solidification. With the increasing particle velocity, the in-flight time of particles inside the plasma jet shortens. The shorter is the in-flight time of the particle to the substrate, the lower is the particle temperature at the moment of impact. The increase of the substrate temperature improves the lamellar bonding but also increases the α-Al_2O_3 phase content. [40]

There was also observed the decrease of the coating thickness from 35 to 25 µm with increase of plasma temperature. The decreased thickness is caused by excessive vaporization of the particles during the flight. [40]

Plasma sprayed coatings Al_2O_3, ZrO_2, Al_2O_3 / ZrO_2 and ZrO_2/ Al_2O_3 were examined on corrosion resistance. Coatings were fabricated on stainless steel using 9 MB Metco plasma spray system (80kW). Before coating, the samples were grit blasted using 20 µm alumina grits. [41]

Parameters for spraying Al_2O_3 were: Plasma current- 660 A, Plasma voltage- 50 V, Ar gas flow pressure- 45 (NLPM), H_2 gas flow pressure- 9 (NLPM), Carrier gas flow 400 kPa, Spray passes- 4, Spraying distance- 20 cm.

Parameters for spraying ZrO_2 were: Plasma current- 700 A, Plasma voltage- 55 V, Ar gas flow pressure- 42 (NLPM), H_2 gas flow pressure- 8 (NLPM), Carrier gas flow 400 kPa, Spray passes- 4, Spraying distance- 20 cm. [41]

Porosity of the coatings was: Al_2O_3 - 9.2 %, ZrO_2 - 14,1 %, Al_2O_3 / ZrO_2 -7,3 % and ZrO_2/ Al_2O_3 - 2,4 %. Hardness of the Al_2O_3 coating was 825±8 $(HV)_{0.2}$ and a surface roughness was 8.25 µm. [41]

Results showed a high level of severe corrosion for monolayers Al_2O_3 and ZrO_2 coating. Better results had bilayer systems of (Al_2O_3 / ZrO_2 and ZrO_2/ Al_2O_3). The better oxidation resistance was due to the lower porosity. [41]

V. Al_2O_3 – 40 wt. % TiO_2

The addition of 40 wt. % of TiO_2 into Al_2O_3 creates a wear resistant and chemically stable coating. The coating should have a moderate hardness. Fracture toughness should be higher, when compared to coatings with lower amount of TiO_2. This coating should withstand temperatures up to 540 °C. [42]

The addition of TiO_2 in to the Al_2O_3 powder decreases the melting temperature. TiO_2 also helps to reduce porosity. The measured porosity of Al_2O_3 with 40 wt. % of TiO_2 is lower than with 3 % or 13 % of TiO_2. [43]

Most occurring forms of TiO_2 are rutile and anatase. Both phases are tetragonal but the anatase has octahedrons, that share four edges forming the four-fold axis. Most stable is rutile phase. [44]

In Al_2O_3-TiO_2 coatings also the phases α-Al_2O_3, β-Al_2O_3 and Al_2TiO_5 can be found. [45]

Properties of TiO_2 are written in the Tab. 10

Tab. 10 Properties of TiO_2 [46]

Density [g/cm^3]	3.8±0.3
Hardness Vickers	830±114
HRC	50-55
Tensile strength [MPa]	333-367.5
Compressive strength [MPa]	660-3675
Elastic modulus	228±52
Fracture toughness MPa/m^2]	2.4-3.3
Melting temperature [°C]	1843
Maximum service temperature °C	1566-1634
Thermal expansion [10^{-6}/K]	9±0.7

The Al_2O_3 – 40 wt% TiO_2 coating was tested on tribometer under different loads. The track diameter was 40 mm, sliding speed was 1 m/s and sliding distance 2010.88 mm (time was 20 min.). Under the load of 5 N, the coating wear rate was 4 mm^3/Nm.

Under the same conditions $Al_2O_3 - 13$ wt% TiO_2 was tested. The wear rate was about 5,5 mm^3/Nm. [45]

Sliding wear and coefficient of friction of $Al_2O_3 - 40$ wt% TiO_2 coating compared with NiCr - Cr_2O_3 coating is shown in the Attachment 15 and Attachment 16, respectively. The surface morphology before sliding wear is shown in the Attachment 18. Surface morphology after sliding wear is shown in the Attachment 19. The EDS analysis of the surface after sliding wear under the load 10 N is shown in the Attachment 20.

Another study is investigating the corrosion behavior of ceramic coating Al_2O_3 (denoted as A), composite ceramic coating 13 wt.% TiO_2- Al_2O_3 (denoted as 13TA) and gradient composite ceramic coating NiAl- 13 wt.% TiO_2- Al_2O_3 (denoted as NA-13TA).

The average grain size of the TiO_2 and Al_2O_3 powder was 40 ~60 μm. The average size of the Ni-Al grain was 80~100 μm. First there was applied the nickel-aluminum alloy bond layer to increase the adhesive strength of the ceramic coating to the steel substrate. The thickness of the A, 13TA and NA-13TA coatings was 0.3, 0.4 and 3.6 mm, respectively. Pores were defined as open pores. The corrosion weight loss of the samples with three ceramic coatings is shown in the Attachment 11. The corrosion weight loss of samples with NA-13TA coating can be seen in the Attachment 12. It is possible to see, that the lowest corrosion suffered the NA-13TA coating. There were no traces of damage seen in the coating even after 14 h. Bigger corrosion we could see for the 13TA coating. The rapid increase of corrosion for 13AT coating was after 23 h. The highest corrosion had the coating A. The corrosion of the coating A increased rapidly after 17 h. At the beginning the 13TA coating had higher corrosion weight loss due to TiO_2. [47]

The porosity is an important factor for the corrosion resistance. The highest open and connected porosity had the A coating. The 13TA coating had lower porosity due to the TiO_2 content, which has lower melting point. That is why, during the spraying, the TiO_2 filled the pores of Al_2O_3, which has higher melting point. [47] Also, the connected porosity decreases with increasing coating thickness. [48]

Because there were no connected pores in the gradient NA-13TA coating, the corrosion medium did not corrode the nickel-aluminum alloy layer and the substrate.

16

There was discovered just the partial corrosion of the surface ceramic coating and the interlayer coating. Different amount of connected porosity for the coatings are shown in the Pic. 7. [47]
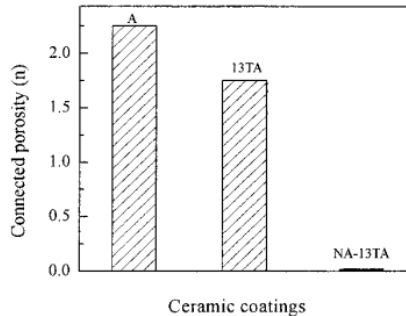
Pic. 7 Connected porosity of three ceramic coatings A, 13TA and NA-13TA [47]

Improvement of the Al_2O_3 - 13 wt.% TiO_2 coating properties is possible by electron beam modifying. The electron beam changes the microstructure, phase constituents and wear properties by re-melting the splats. [49]

The Al_2O_3-13 wt.% TiO_2 powder (5- 35 µm) was deposited by atmospheric plasma spraying. The coating thickness was 260 microns. It was grounded to 100 microns before the use of electron beam. [49]

Phase composition was investigated by X-Ray diffraction analysis. The sliding wear resistance was determined by pin-on-disk. The load for pin-on-disk method was 20 N, relative velocity between the ball (WC) and the surface was 20 cm/s and the sliding distance was 2000 m. The hardness was measured by micro Vickers hardness tester. [49]

Structure of as-sprayed Al_2O_3-13 wt.% TiO_2 coating is shown in the Pic. 8. The irregular structure of lamellar splats can be seen with some porosity and voids. The adherence of the coating is influenced by inclusions at the interface of the coating and the substrate. [49]
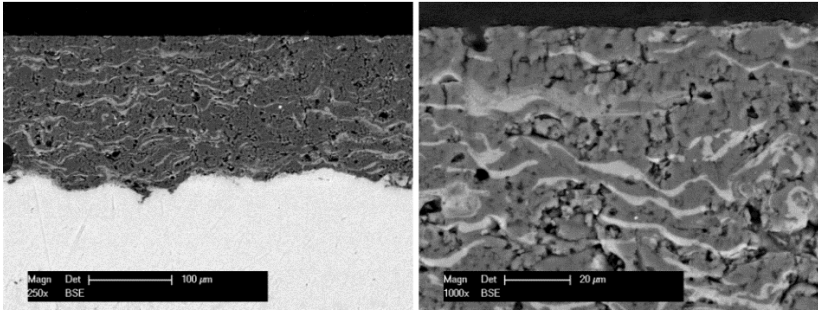
Pic. 8 SEM micrograph of the plasma sprayed Al_2O_3-13 wt.% TiO_2 coating [49]

After remelting of the coating by electron beam the structure of the coating is more compact. The oxides are removed, the lamellar defects eliminated. The diffusion zone of the titanium is clearly seen along the interface. The SEM micrograph of the coating after remelting by electron beam is shown in the Pic. 9. [49]
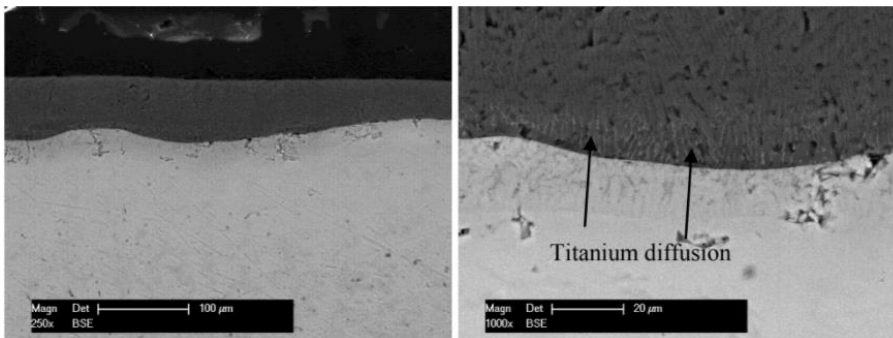
Pic. 9 SEM micrograph of the EB remelted Al_2O_3-13 wt.% TiO_2 coating [49]

The XRD pattern of the as-sprayed coating identified the phases like: η-Al_2O_3, α-Al_2O_3 and TiO_2. The XRD of the remelted coating showed that, metastable η-Al_2O_3 phase in the remelted region transferred into the stable α- Al_2O_3 phase. Because of the remelting and recrystallization of the coating. Also new phase tistarite Ti_2O_3 was formed. [49]

Microhardness of the as-sprayed coating was 850±30 $HV_{0.3}$. The hardness of the remelted coating was 1470±60 $HV_{0.3}$. The results from sliding test showed the remelted coating has higher sliding wear resistance. [49]

Another study compared wear between A40T and NiCr-Cr_2O_3 coatings. This will be described in the Cr2O3-25 wt.% NiCr chapter.

VI. Cr_2O_3-25 wt.% NiCr

Chromium oxide has excellent wear resistance and friction properties. It was often used as thermal protection and wear protection for piston engine rings. Properties of Cr_2O_3 are written in the Tab. 11. [50] The NiCr is ensuring the corrosion resistance of the coating. [51]

Cr_2O_3 can occur in more phases. The α-Cr_2O_3 is the most stable phase. It has similar crystal structure to alpha Al_2O_3, hexagonal close-packed. [52]

The Cr_2O_3 plasma sprayed coating can have higher porosity. [53] Porosity of Cr_2O_3 can be 3.1 % when plasma sprayed. [54]

The adhesion to the substrate needs to be ensured as the other coatings. The Cr_2O_3 has for example weaker bonds with the substrate 25CrMo4 steel. Chromium oxide is also used as interlayer for Cr, NiCr or NiCrAl coatings. [53] Cr_2O_3 increases the hardness of the material. [51]

Wear rate of Cr_2O_3 has been measured to 2.5×10^{-4} $mm^3 \cdot N^{-1} \cdot m^{-1}$. With the dry-ice blasting, it lowered to 5×10^{-7} $mm^3 \cdot N^{-1} \cdot m^{-1}$ [53]

Tab. 11 Properties of Cr_2O_3 [55, 54, 56, 57, 58, 59]

Density [g/cm^3]	5.22 (bulk), 4.65 (coating) [59]
Hardness Vickers [GPa]	11.18 – coating sprayed by plasma [57]
Tensile strength [MPa]	178-400 [58]
Compressive strength [GPa]	1.6-2.6 [58]
Fracture toughness MPa/m^2]	2.75 – coating sprayed by plasma [57]
Melting temperature °C	2435 [57]
Thermal expansion [10^{-6}/K]	18.6 [56]
Decomposition temperature °C	250-500 [54]

Cumulative wear rate of plasma sprayed Ni-20Cr coating is 0.589×10^{-4} $mm^3 \cdot N^{-1} \cdot m^{-1}$ at 30 N load with the sliding velocity of 1m/s and the distance of 2400m. For the load of 50 N the wear rate was 1.85×10^{-4} $mm^3 \cdot N^{-1} \cdot m^{-1}$. Coefficient of friction μ for Ni-20Cr was found to be 0.44 for the load of 30 N. For the load of 50 N the coefficient of friction μ was 0.4. [60]

Micrograph of Cr_2O_3 coating plasma sprayed is shown in the Attachment 13.

The surface morphology of the NiCr-Cr_2O_3 coating, before sliding wear, can be observed in the Attachment 14. The comparison between sliding wear of NiCr-Cr_2O_3

and A40T (Al_2O_3-40 %TiO_2) coatings is shown in the Attachment 15. The Cr_2O_3 particles from the top coat caused the wear enlargement of the coating. Different coefficient of friction for NiCr-Cr_2O_3 and A40T coatings are shown in the Attachment 16. The wear morphology is shown in the Attachment 17. [61]

Difference in mass loss and wear resistance of the nickel pin and A40T and NiCr-Cr_2O_3 coatings is shown in the Pic. 10 and the Pic. 11, respectively. [61]
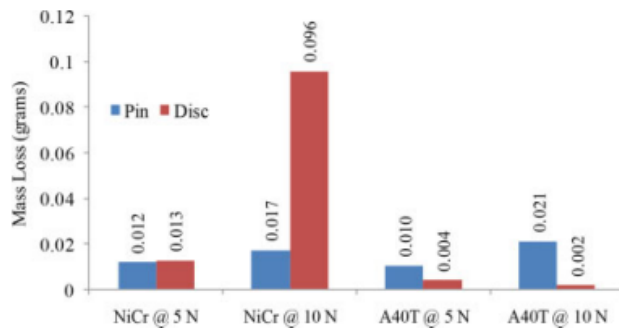
Pic. 10 Difference in mass loss measured in pin and coated disc for NiCr-Cr_2O_3 and A40T [61]
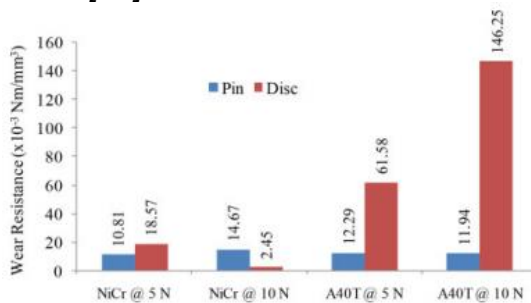
Pic. 11 Wear resistance of nickel pin and coated disc with respect to applied load [61]

The wear resistance of A40T coated disc is superior to NiCr-Cr_2O_3 coated disc. The mass loss of the A40T coating is five times less than that of the NiCr-Cr_2O_3. Surface morphology of A40T coating, before sliding wear test, is shown in the Attachment 18. Wear and surface morphology of A40T coating after sliding wear under the load of 10 N is shown in the Attachment 19. The composition of the coating after the sliding wear is shown in the Attachment 20. [61]

Wear studies of different coating materials:

Tribological behavior of plasma-sprayed Al_2O_3-20 wt.%TiO_2 coating with the 80Ni-20Al bonding layer was investigated in the study [62]. The size of the angular shaped powder particles was 20-35 μm. The parameters of plasma spraying are written in the Attachment 21.

The porosity of the as-sprayed coating was calculated by quantitative image analysis according to the ASTM E2109 standard. 3D morphology was examined by super depth-of-field 3D system (VHX-1000). Vickers hardness was performed on the as-sprayed matrix and the cross section by MHVD-30AP instrument. [62]

For the wear behavior, the pin-on-disc method was used. The substrate and the coating were studied by the tester HT-500, CAS at 20 °C. The Si_3N_4 ball with the diameter of 5 mm was used. The loads were 5, 10 and 15 N. Turning radius was 2 mm, velocity 0.117 m/s and time 120 min. The average wear widths were reported, and the wear-induced weight losses were assessed by measuring the width of the wear tracks from SEM images. [62]

Because of the high temperature during spraying some Al_2TiO_5 phase was formed, which is undesired due to anisotropic coefficient of thermal expansion which causes formation of internal cracks. This phase also reduced adhesion between the coating and the Ni-Al bonding layer. Some of the α- Al_2O_3 transformed during solidification to metastable γ- Al_2O_3, which was wanted due to lower interfacial energy. [62]

The porosity of the Al_2O_3-20 wt.%TiO_2 were around 2.83 %. The average Vickers hardness of the Al_2O_3-20 wt.%TiO_2 and the substrate were 1091.2 ± 176.8 and 151.4 ± 12.3 HV_3, respectively. The hardness can be enhanced using Al_2O_3 particles. The high standard deviations are due to inhomogeneous nature of the coating with different phases in different regions. The composition of the powder and the coating is shown in the Attachment 23. The morphology from SEM image is shown in the Attachment 24 [62]

The material Al_2O_3-20 wt.% TiO_2 was also tested under different loads (5, 10 and 15 N) at equal sliding distance. There was decrease in friction coefficients with increase in the load. The friction coefficient of the matrix rapidly increased in the first 10 min. and then remained stable until the end of the test. The maximum steady-state friction coefficients of the substrate and the coating were 0.42 and 0.36, respectively, at 15 N. This is shown in the Pic. 12. [62]
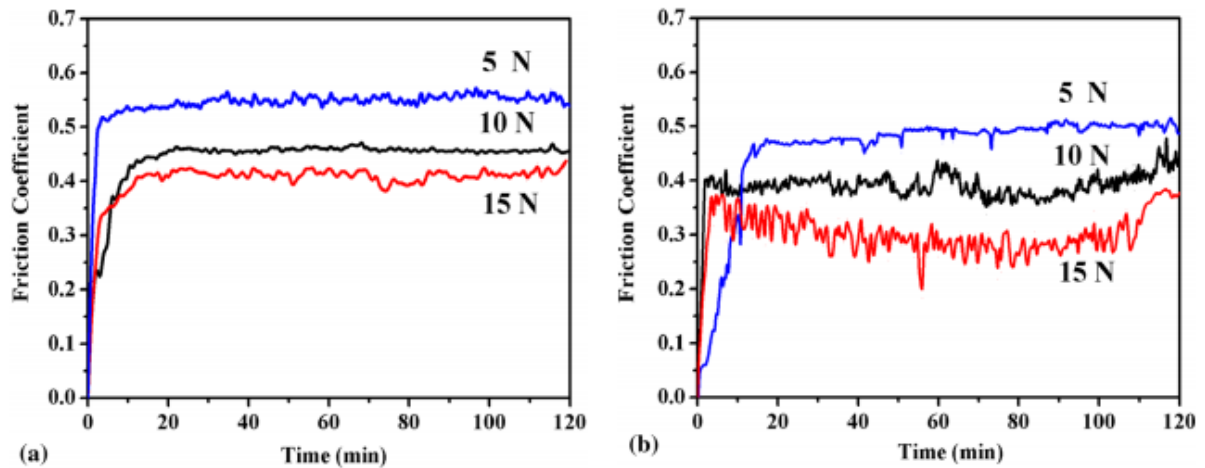
Pic. 12 The coefficient of friction for (a) the Grade D steel and (b) the Al_2O_3-20 wt.% TiO_2 coating [62]

The grinding crack width of the coating from the ball (4 mm diameter) was increased with the increase in the load: 1591.2, 1852.6 and 2009.8 μm at 5, 10 and 15 N, respectively.

The specific wear rate of the coating was the lowest (~3.3 x 10^{-6} mm^3/Nm) when the load was 5 N. For the Grade D steel, the specific wear rate was ~283.3 x 10^{-6} mm^3/Nm at 15 N. This value is approximately 70 times larger than for the coating. The volume loss and the specific wear rate is written in the *Attachment 25*. The SEM images of the worn surface and steel is shown in the Attachment 26. [62]

Coating Al_2O_3-ZrO_2, applied with higher Plasma electrolytic oxidation (PEO) voltage, shows higher roughness of the surface. That increases also the friction coefficient. Also, at higher PEO voltage, both tetragonal ZrO_2 and α- Al_2O_3 phases were increased, which led to higher hardness of the coating. The fracture toughness can be also determined as property for wear resistance. In alumina-zirconia composites, the zirconia particles suppress the crack initiation and propagation. [63]

Comparison of Forsterite, 8YSZ, Nano-8YSZ, Mullite, La2Zr2O7 coatings:

Some thermal barrier coatings (TBC) were examined for their thermal insulation properties, oxidation and spallation resistance. The examined coatings were mullite, forsterite, $La_2Zr_2O_7$, 8YSZ (yttrium stabilized zirconium), and nanostructured 8YSZ. Bond coat was made from NiCrAlY material with the thickness of 135±12 μm. Thickness of the top coatings is written in the Attachment 27. SEM images of the 8YSZ coating is shown in the Attachment 28. [64]

22

Coatings were thermally cycled. The thermal cycle included heating for 240 seconds with gas temperature 760 °C and cooling for 170 seconds with gas temperature 134 °C. The porosity of different plasma-sprayed coatings in as-sprayed condition, thermally cycled in air and thermally cycled in exhaust gas is shown in the Attachment 29. Vickers hardness (HV) for the same coatings in as-sprayed condition and thermally cycled in air and exhaust gas is shown in the Attachment 30. The hardness of Forsterite and 8YSZ decreased when tested in air and exhaust gas. The hardnes after air test was the worst.

Mullite seemed to have no cracks after spraying. It contained some small spheroidal pores. Forsterite showed small number of cracks connected to pores. The microstructures are shown in the Attachment 31. Both coatings show segregation of SiO_2. [64]

Forsterite coating exhibited merging of pores after thermal cycling. That resulted in lower porosity but higher thermal conductivity. Nano-8YSZ had as forsterite lower porosity after thermal cycling. The porosity of 8YSZ and $La_2Zr_2O_7$ increased due to increased crack density. Cracks were formed between the pores. The zirconia coatings 8YSZ, $La_2Zr_2O_7$, and nano-8YSZ had the lowest thermal conductivity (0.7, 0.8, and 1.3 W/m K, respectively). Mullite had higher thermal conductivity (2.7 W/m K). [64]

Differences were observed also for spallation resistance of the coatings. Mullite with the lowest coefficient of thermal expansion (5.3×10^{-6} K^{-1}) showed some spallation after cycling in air and complete spallation after cycling in diesel exhaust gas. Forsterite with the thermal expansion coefficient 9.5×10^{-6} K^{-1} showed cracks along the TBC/Bond coat interface in both tests. $La_2Zr_2O_7$ exhibited low spallation at the surface after thermal cycling in air. Based on the appearance of the crack structure, nano-8YSZ, and 8YSZ may have the best resistance to spallation. The SEM microstructures after cycling in air are shown in the Attachment 32 and Attachment 33. [64]

Another study shows the importance of the spraying distance and the coating thickness. The YSZ (ZrO_2 - 7 wt% Y_2O_3) coating had the best results when shock tested with the thickness of 377 ± 14 μm. The spraying distance was 80 mm. Coatings with the spraying distance of 120 mm showed worse results. The influence of the spraying distance and the thickness of the coating is compared in the Attachment 34. The feed rate was 54 g/min. [65]

2.3 EVALUATION OF COATINGS

Light microscopy

Stereo microscope is used to analyze the surfaces, wear tracks and the cross sections of the samples. Zoom ratio of this microscope is from 0.75x to 11,25x. The total magnification is from 3.75x to 540x. These ranges allow user to see and document samples from macro views to high-magnification micro visualization. [66] The stereomicroscope is shown in the Attachment 22.

For the metallographic observation, the samples can be embedded in epoxy resin to provide support for cutting the cross section. This avoids the detachments of the coating from the base material. The cross sections are usually polished with silicon carbide abrasive papers following sequence from 250 to 1000 grit. Final polish is done with 3 and 1 µm diamond suspensions. [67]

Electron microscopy

Microstructure of the coating cross section can be observed by emission scanning electron microscope (SEM). This microscope scans the specimens by focused electron beam with relatively low energy. The impact of the electron beam to the surface of the specimen causes emission of high-energy backscattered electrons and low-energy secondary electrons from the specimen. Variety of detectors can be used for different types of scattered electrons. The scattered electrons include the secondary electrons, backscattered electrons or x-rays.

Non-conductive specimens need to be sputter coated and other biological specimens need to be dehydrated before they are placed un the vacuum chamber. [68]

Thickness

The basic method to evaluate the thickness of the coating is Calotest. This method uses a hard ball which indents the coating with different spinning speed and different time. The size of the ball varies from 10-40 mm. The spin speed of the ball is from 10 – 2900 rpm and the time is from 1 second to 15 minutes. The thickness is then calculated by the ball canopy. This method is also good for finding the thickness of bond layers. [69]

Other methods used for an evaluation of the thickness are fractographic methods on the scanning electron microscope or on the stereo microscope.

Tribology

This test is carried out on the Tribometer. The spherical indenter is pressed into the surface of a rotating disc. According to the circular mark made by the indenter we discover the friction and the wear coefficient. Schematic picture of the apparatus is in the Pic. 13. This test can be performed in elevated temperatures up to 800°C.
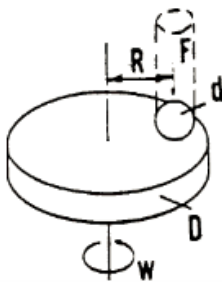
Pic. 13 Schema of the pin on disc test apparatus [70]

The linear wear is recorded by two separate devices, which register the wear depth up to 5 mm with resolution of 1 μm.

Different materials for pin can be chosen according to the suitability with the coating or substrate material. The material of the pin should be chemically stable since it is in the contact with the specimen material. The pin material is also chosen according to the hardness of the specimens. It is more convenient, when the pin material is harder, because the primary focus is the wear of the specimen.

The WC/Co pin (HV≈22 GPa) can be used for Al_2O_3-ZrO_2 coating. Other materials for pins can be for example Al_2O_3 or Si_3N_4. To keep the chemical stability at high temperature, Al_2O_3 balls are suitable. [63]

ASTM G 99-95a, Tribometer test:

The rotating speeds for the wear test are usually 60-600 r/min. This method can be applied to a variety of materials. The specimens should have specified dimensions and should withstand the stresses during the test without a failure or excessive flexure. The material tested shall be described by dimension, surface finish, material type, form, composition, microstructure, processing treatment and indentation hardness. The pin is cylindrical or spherical with diameter from 2 to 10 mm. Disk parameters are from 30

to 100 mm with the thickness from 2 to 10 mm. Surface is grounded to roughness 0.8 µm arithmetic average or less. [70]

Procedure:

The specimen should be cleaned by non-chlorinated, non-film-forming agents and solvents. Specimen dimensions should be measured to the nearest 2.5 µm or the specimen weight should be measured to the nearest 0.0001 g. The disk is insert to the tribometer, so that is perpendicular (±1°) to the axis of the resolution. Pin should be perpendicular to the disk. After the test, the specimens are cleaned off any loose wear debris. The condition of the wear scar as protrusion, displaced metal, discoloration, microcracking or spotting is noted. [70]

The equation to calculate Pin (spherical end) volume loss [mm^3] [70]:

$$V_p = (\pi \cdot \frac{h}{6}) \cdot (\frac{3d^2}{4} + h^2) \qquad \text{[70]}$$

Where $h = r - (r^2 - \frac{d^2}{4})^{1/2}$, d is wear scar diameter and r is pin end radius. This equation is used when there is no significant disc wear. [70]

The equation to calculate Disc volume loss [mm^3] [70]:

$$V_d = 2\pi R [r^2 \sin^{-1}(\frac{d}{2r}) - (\frac{d}{4})\sqrt{(4r^2 - d^2)}\,] \qquad \text{[70]}$$

Where R is wear track radius, d is wear track width and r is pin end radius. This equation is used when there is no significant pin wear. [70]

The wear of the specimen can also be described according to the wear rate. The equation for the specific wear rate is [63]:

$$K = \frac{V_d}{F \cdot s} \left(\frac{mm^3}{N \cdot m} \right)$$

where V_d is the wear volume of disc measured by means of surface profilometry or calculated according to ASTM 99-95a, F is applied load and s is the sliding distance. Some authors indicate a limit of 10^{-6} mm^3/Nm for K_w value. Above this value the material is no longer considered as wear resistant for unlubricated tribological application. [63]

Roughness

Roughness [μm] can be measured by roughness meter or with profilometer. Roughness can be evaluated as R_a, R_z or R_y. The R_a is an arithmetical average roughness, the R_y is the maximum height measured and the R_z is the ten-spot average roughness.

Hardness

The hardness can be measured according to Rockwell testing, Vickers testing or Brinell testing. For ceramic coatings with high porosity the Rockwell testing will be used. The hardness marked as HRA is a method, where diamante cone tip with the top angle of 120 ° is used. The force of indentation is 588 N, the force of preload is 98,1 N, the time of preload is 1 second and the time of load is 4 seconds.

Nano-hardness

Nano-hardness can be measured. With the higher imprint of the standard hardness test, there is a possibility, that not just the coating hardness but also part of the substrate hardness is measured. The nano-hardness test prevents this problem with the measurement. Nano-hardness is measured with low load forces (mN). If the substrate and the coating hardness wants to be measured together, a higher load up to 100 N needs to be applied. For the hardness the Vickers's quardrangular pyramid is used. It is also possible to measure the modulus of elasticity by nano-hardness test. [69]

Adhesion

Adhesion can be evaluated from metallography of cross section. Low adhesion of the coating may be due to porosity, cracks or other heterogeneities. [69]

Other possibility is to use scratch-test. In this test Rockwell's conical indenter is pushed with increasing load into the coated surface. The load varies from 1 to 200 N. It is possible to change the load, the velocity of the load, velocity of the indenter's move and the diameter of the indenter. It is possible to do also the Micro- and Nano-scratch tests. The results from the scratch test can be compared only with the results of materials with similar base material because the base material influences the results. [69]

Another evaluation of the coating properties can be the scratch test. The scratch test is performed through the contact of moving Rockwell diamante tip with the coating surface. This test is used for evaluation of the coating adhesion, depth of penetration or friction coefficient. This type of scratch test is, however, insufficient for thick coatings according to standard testing method ASTM C 633. A new method of scratch test was developed. This method is described in draft ISO/WD 27307. This method is using the scratch test on the cross-section of the thick coating. [71] This standard is suitable for thick coatings from 50 µm up to 1000 µm. It can be used for thermally sprayed ceramic coatings. [72]

Corrosion

Salt spray test is type of corrosion testing. The test is performed in a closed chamber, that can be adjusted, to create a variety of corrosive environments. Testing time and salt concentration in the chamber are chosen according to the type of product and its intended use.

The 5% NaCl solution is typical for the test. In addition, another condition can be changed to simulate the corrosion environment as humidity or temperature. [73]

3. PRACTICAL PART

3.1 PLASMA SPRAYING DATA

Before coating with the water stabilized plasma, the specimens needed to be prepared. Small round samples of T91 steel with the diameter of 25 mm were cut. The width of the specimens was 4 mm. The specimens were grinded. The surface of the specimens was too smooth for the coating and the powder would not stick on the samples correctly. The samples needed to be blasted with Al_2O_3 particles to increase the roughness of the surface. Granulometry of the Al_2O_3 particles was F 240- F 280. The blasting took place just before the coating. The arithmetical mean of roughness (Ra) was 6 μm. After blasting, the samples needed to be cleaned in ultrasonic cleaner Pic. 14. Cleaning time was 5 minutes.

Pic. 14 Ultrasonic cleaner Bandelin Sonorex

After blasting and cleaning, samples were attached to the rotating support head. The samples placed in the support head can be seen in the Pic. 15.

Pic. 15 Support head with the T91 steel specimens prepared for plasma coating

Al$_2$O$_3$

Producer of the powder was Koltex CZ. Spraying parameter are written in the Tab. 12.

Tab. 12 Spraying parameters of Al$_2$O$_3$

powder feed rate [kg/h]	10
Spraying distance [mm]	360
Stand-off distance [mm]	55
Current [A]	500
Preheat temperature [°C]	150
Number of plasma crossings	27
Cooling medium	Air
Granulometry of the powder	AB 230
Thickness of coating [μm]	524.57

Al$_2$O$_3$-40 wt% TiO$_2$ (AT40)

Producer of the powder was Prachovice. Spraying parameters are written in the Tab. 13.

Tab. 13 Spraying parameters of Al$_2$O$_3$-40 wt% TiO$_2$

powder feed rate [kg/h]	10
Spraying distance [mm]	370
Current [A]	500
Stand-off distance [mm]	75
Preheat temperature [°C]	150
Number of plasma crossings	12
Cooling medium	Air
Granulometry of the powder [μm]	25-50
Thickness of coating [μm]	530.74

Olivine

Producer of the powder was Sand Team. Spraying parameters are written in the Tab. 14. The composition of the powder was MgO 49 %, SiO$_2$ 41 % and Fe$_2$O$_3$ 7,4 %.

Tab. 14 Spraying parameters of Olivine

powder feed rate [kg/h]	10
Spraying distance [mm]	400
Current [A]	500
Stand-off distance [mm]	80
Preheat temperature [°C]	150
Number of plasma crossings	12
Cooling medium	Air
Granulometry of the powder [μm]	40-130
Thickness of coating [μm]	672.69

ZrSiO$_4$

Producer of the powder was glazurka Roudnice. Spraying parameters are written in the Tab. 15.

Tab. 15 Spraying parameters of ZrSiO$_4$

powder feed rate [kg/h]	10
Spraying distance [mm]	350
Current [A]	500
Stand-off distance [mm]	65
Preheat temperature [°C]	150
Number of plasma crossings	9
Cooling medium	Air
Granulometry of the powder [μm]	40-70
Thickness of coating [μm]	619.2

ZrSiO$_4$- 30 mol% Y$_2$O$_3$

The producer of the powder ZrSiO$_4$ was glazurka Roudnice. Powder was mixed mechanically. The 30 mol% of Y$_2$O$_3$ is equal to approximately 38 wt%. SEM image of the powder is in the Pic. 16. Chemical analysis of the powder ZrSiO$_4$-Y$_2$O$_3$ was done with Scanning electron microscope. Chemical composition of spectrum 1 and spectrum 2, which are shown in the Pic. 17, is written in the Tab. 16. In the Pic. 17, spherical particles match the Y$_2$O$_3$ and the crystal particles match ZrSiO$_4$.
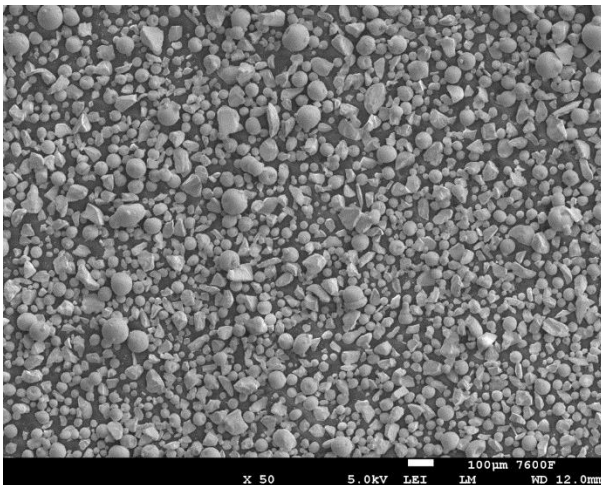
Pic. 16 SEM image of ZrSiO$_4$-Y$_2$O$_3$ powder
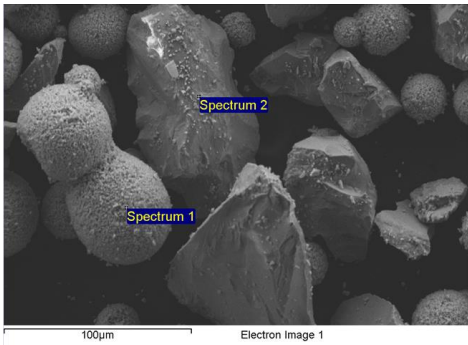
Pic. 17 SEM image of the ZrSiO$_4$- Y$_2$O$_3$ powder and spectrum of the powder

Tab. 16 Composition of Spectrum 1 and Spectrum 2

Spectrum 1		
Element	Weight %	Atomic %
Oxygen	27,98	68,34
Yttrium	72,02	31,66
Spectrum 2		
Element	Weight %	Atomic %
Oxygen	50,45	79,13
Silicon	11,71	10,46
Zircon	37,84	10,41

Spraying parameters of ZrSiO$_4$ -30 mol% Y$_2$O$_3$ are written in the Tab. 17.

Tab. 17 Spraying parameters of ZrSiO$_4$-30 mol% Y$_2$O$_3$

powder feed rate [kg/h]	10
Spraying distance [mm]	350
Current [A]	500
Stand-off distance [mm]	65
Preheat temperature [°C]	150
Number of plasma crossings	9
Cooling medium	Air
Granulometry of the powder [µm]	40-70
Thickness of coating [µm]	522.52

NiCr – Cr$_2$O$_3$

Chemical composition of the powder was NiCr (20% Cr) – 40% Cr$_2$O$_3$. Powders were mechanically mixed. Producers of the powders were CSSR and Amperit. Spraying parameters are written in the Tab. 18.

32

Tab. 18 Spraying parameters of NiCr-40 wt% Cr_2O_4

powder feed rate [kg/h]	10
Spraying distance [mm]	300
Current [A]	500
Stand-off distance [mm]	85
Preheat temperature [°C]	100
Number of plasma crossings	18
Plasma gas	Ar + H_2
Cooling medium	Air
Granulometry of the powder NiCr [µm]	100-140
Granulometry of the powder Cr_2O_3 [µm]	22-45
Thickness of coating [µm]	523.66

3.2 TESTING

Specimens preparation

Prior to testing, the specimens needed to be cleaned from remaining powder from plasma spraying. Some of the powder was not melted completely and did not stick to the rest of the coating. For cleaning the specimens, the ultrasonic cleaner was used. The Nikon SMZ 1500 Stereo Microscope was used for evaluation of the structure.

3.2.1 STRUCTURE OF COATINGS

Al_2O_3

Cross sections of the Al_2O_3 coating are shown in the Pic. 18 and Pic. 19. The bonding strength of the coating is quite low. The adhesion to the substrate is good since the crack did not occur between the coating and the substrate. The coating cracked in the lower middle. The crack might be due to epoxy resin, in which it was put to. It could be caused by the different thermal expansion coefficients of the materials. The porosity of the coating is relatively high. Porosities can be observed as black spots in the cross section.
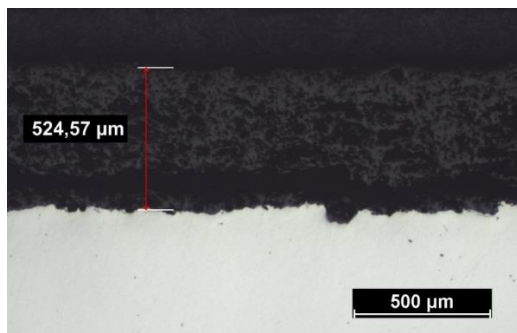
Pic. 18 Polished cross section of Al_2O_3 coating
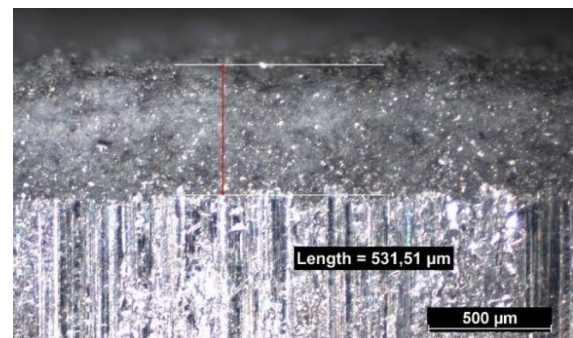
Pic. 19 Cross section of Al_2O_3 coating

Al_2O_3-40 wt % TiO_2 (AT40)

Cross sections of the AT40 coating are shown in the Pic. 20 and Pic. 21. When compared to the Al_2O_3 coating, the porosity of AT40 decreased significantly. The TiO_2, since it has lower melting temperature, could fill the porosities easier than Al_2O_3, when

plasma sprayed. This results in denser coating. There are no cracks present in the cross section.
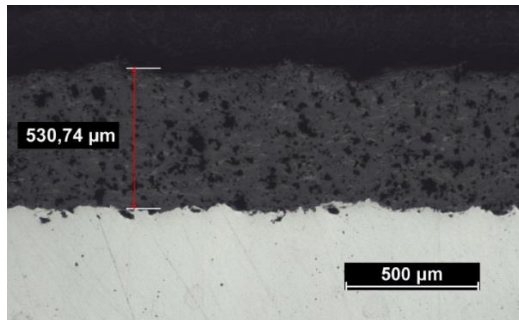
Pic. 20 Polished cross section of AT40 coating
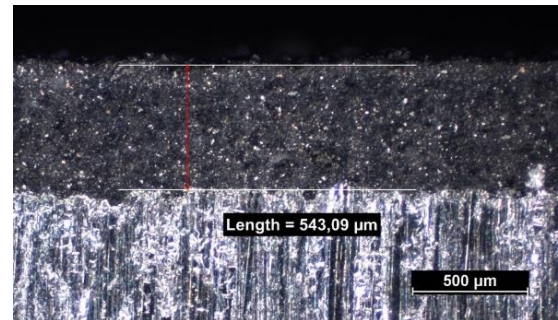
Pic. 21 Cross section of AT40 coating

Olivine

Cross sections of the olivine coating are shown in the Pic. 22 and Pic. 23. This coating, similarly to AT40, shows lower porosity. The pores are the black spots in the Pic. 22. The coating is dense without any signs of cracks.
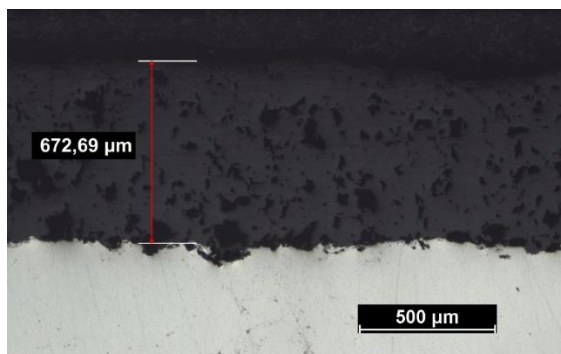
Pic. 22 Polished cross section of Olivine coating
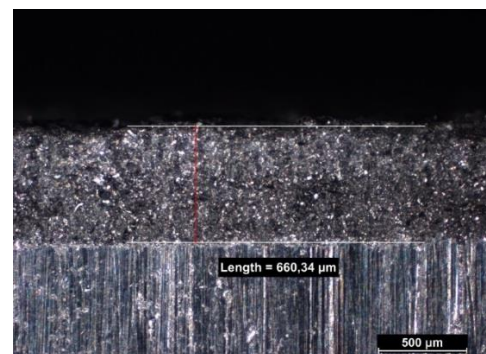
Pic. 23 Cross section of Olivine coating

ZrSiO$_4$

The cross sections of the ZrSiO$_4$ coating are shown in the Pic. 24 and Pic. 25. The porosity, which is represented by black marks, is quite high. It is also possible to see, that the coating did not adhere to the substrate well. The space between the coating and the substrate increased after it was put into the epoxy resin.
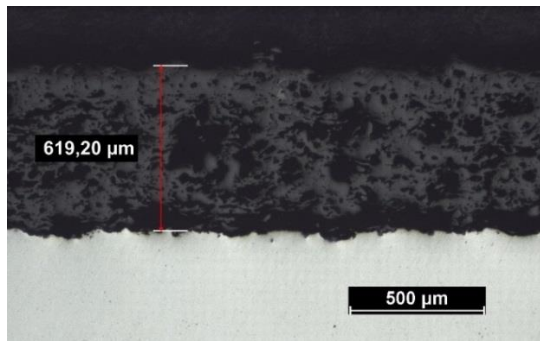
Pic. 24 Polished cross section of $ZrSiO_4$ coating
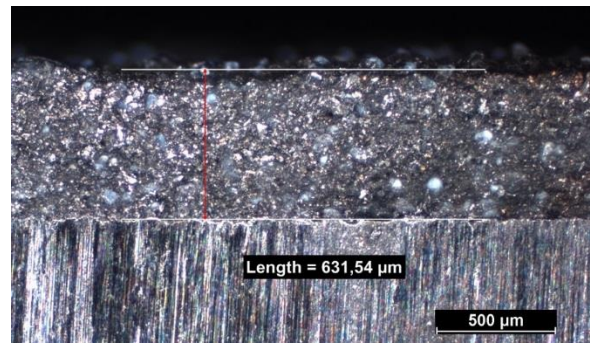
Pic. 25 Cross section of $ZrSiO_4$ coating

$ZrSiO_4$-Y_2O_3

The high porosity of the material can be observed from the cross-section of the $ZrSiO_4$-Y_2O_3. The porosity is seen as the black spots on the cross-section of the coating in the Pic. 26. The coating is not in the contact with the substrate. It might be due to insufficient adhesion to the substrate. The separation of the coating could be enhanced by the different coefficient of thermal expansion, when the sample was put into the epoxy resin. The cross-sections of the coating are shown in the Pic. 26 and Pic. 27. In the Pic. 27 it is clearly seen, that there are unmelted particles entrapped in the coating. This could have effect on the porosity, which could increase significantly. Unmelted particles could signify insufficient plasma power, with which would maybe the powder melt completely.
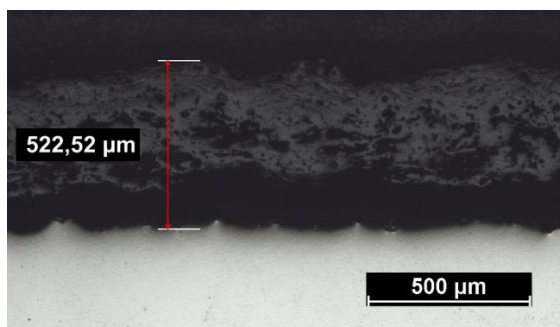
Pic. 26 Polished cross section of $ZrSiO_4$-33 mol% Y_2O_3 coating
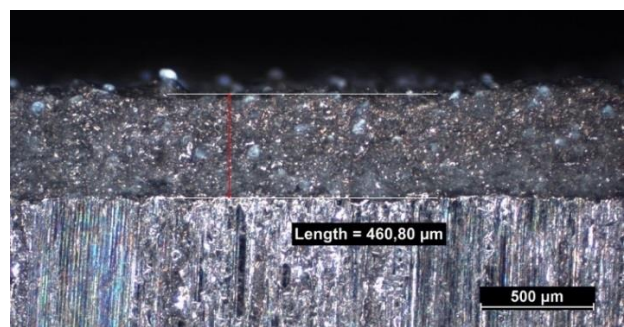
Pic. 27 Cross section of $ZrSiO_4$-33 mol% Y_2O_3 coating

NiCr-Cr_2O_3

The cross section of the NiCr-Cr_2O_3 coating is shown in the picture Pic. 28. The coating does not show signs of cracks through the whole cross section. The porosity appears low. It might be due to the presence of NiCr particles. These particles could fill out the potential pores.
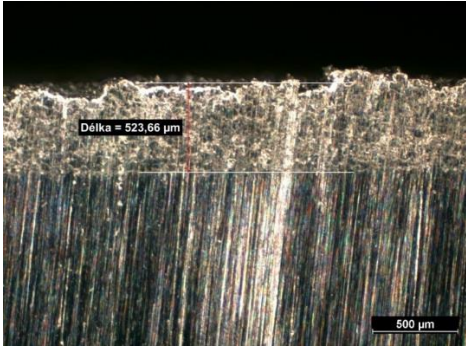
Pic. 28 Cross section of NiCr-Cr₂O₃

3.2.2 HARDNESS

Hardness Rockwell A

The samples, used for hardness measurement, were cleaned with ultrasonic cleaner. The highest hardness was found for the $ZrSiO_4$ coating with the mean value of 68 HRA. Lower hardness had olivine, $NiCr-Cr_2O_3$ and $ZrSiO_4-Y_2O_3$ coatings of around 64 HRA. Lowest value of the hardness was measured for the Al_2O_3 and AT40 coatings, which was 55 HRA and 54 HRA, respectively. The results from the measurements are shown in the Pic. 29. The hardness with the standard deviation are written in the Tab. 19. Whole data set is shown in the *Attachment 35*. Standard deviation of the measurement was high. The reason might be the high porosity of the coatings. The structure of the coatings was uneven, parts of the coatings aborted during the measurement and influenced the result. Because of the abortion of coating walls, it was not possible to use Vickers hardness testing method. The diagonal lines from Vickers indenter were not clearly seen. Standard deviations of $NiCr - Cr_2O_3$ and Olivine were low. This indicates lower porosity of the materials and thus more stable results of HRA.

Hardness of $ZrSiO_4$ and $ZrSiO_4-Y_2O_3$ were 67,6 and 63,6, respectively. The hardness of $ZrSiO_4-Y_2O_3$ in this thesis is less by 13 units, when compared to the 8YSZ hardness (HRA) from the study [64]. It might be due to higher porosity. Also, the olivine coating hardness in this thesis is less by 10 units, when compared to forsterite from the study [64]. The standard deviation of the hardness is also high in the study [64], so the results are quite comparable.
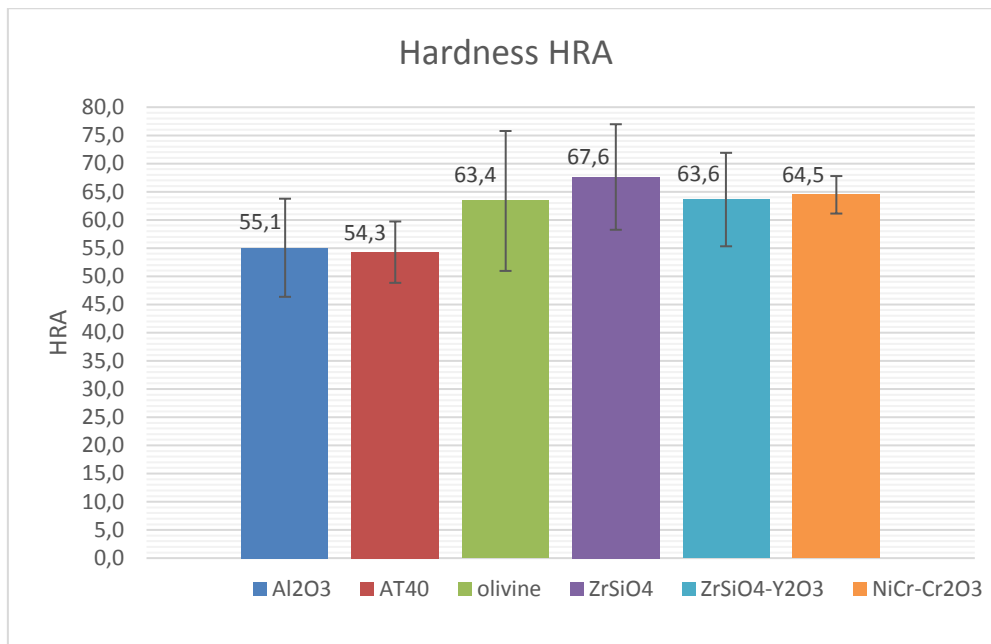
Pic. 29 Mean value of hardness HRA of the tested coatings

Tab. 19 Hardness and standard deviation of the coatings

Type of coating	Al_2O_3	AT40	Olivine	$ZrSiO_4$	$ZrSiO_4 - Y_2O_3$	$NiCr-Cr_2O_3$
HRA (Mean value)	55,1	54,3	63,4	67,6	63,6	64,5
Standard deviation of HRA	8,70	5,45	12,41	9,36	8,29	3,33

Hardness Rockwell A after heat treatment

To evaluate the stability of the coatings at high temperatures, a set of coated specimens was heat treated at work temperature around 650 °C for 10 hours, cooled on air. The hardness was expected to remain the same. However, some changes occurred. The hardness with standard deviation is written in the Tab. 20.

Hardness of olivine and $NiCr-Cr_2O_3$ increased. Their standard deviation remained the same as before the heat treatment. The hardness of the coating AT40 increased also, but the value of standard deviation increased two times. The high value of standard deviation could be the sign of remaining or increasing porosity and again the instability of the coating.

Lower hardness of $ZrSiO_4$ and $ZrSiO_4-Y_2O_3$ could be caused by higher porosity. Volume shrinkage could be present after heat treatment of the coatings. Standard deviation of hardness increased for these two coatings.

Hardness of Al_2O_3 remained at the same level.

39

Mean value of hardness is shown in the Pic. 30. The measured hardness data is in the *Attachment 36*.
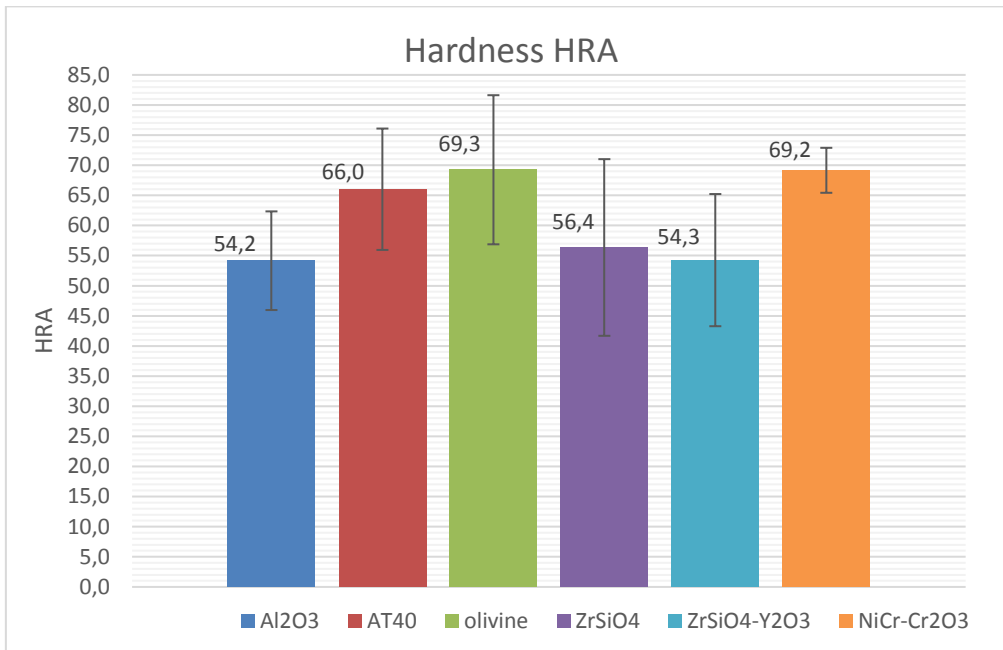
Pic. 30 Mean value of hardness HRA of the tested coatings after heat treatment at 650 °C for 10 hours

Tab. 20 Hardness and standard deviation of coatings after heat treatment at 650 °C for 10 hours

Type of coating	Al_2O_3	AT40	Olivine	$ZrSiO_4$	$ZrSiO_4$ - Y_2O_3	$NiCr$-Cr_2O_3
HRA (Mean value)	54,2	66,0	69,3	56,4	54,3	69,2
Standard deviation	8,19	10,08	12,38	14,66	10,97	3,73

More accurate results would be with lower standard deviation. High standard deviation signifies heterogeneities of the coatings and high porosity. Lower porosity can be achieved by adjustment of spraying parameters as smaller powder particles, spraying distance, power input or flow of inert gas.

3.2.3 ROUGHNESS

Roughness of the coatings was measured by an automatic roughness measurement instrument. The results are plotted in the Pic. 31. Roughness of $ZrSiO_4$ was the highest, 12.56 µm, The $NiCr-Cr_2O_3$ coating had the second highest roughness, 11.59 µm. Lower roughness had $ZrSiO_4-Y_2O_3$, AT40 and Al_2O_3 with 10.47 µm, 9.54 µm and 7.55 µm, respectively. Olivine coating had the roughness 7.55 µm as Al_2O_3. Standard deviation of measurements was high. High roughness of $ZrSiO_4$ and $ZrSiO_4-Y_2O_3$ could be caused by unmelted particles, which were observed in the coating by stereo microscope.
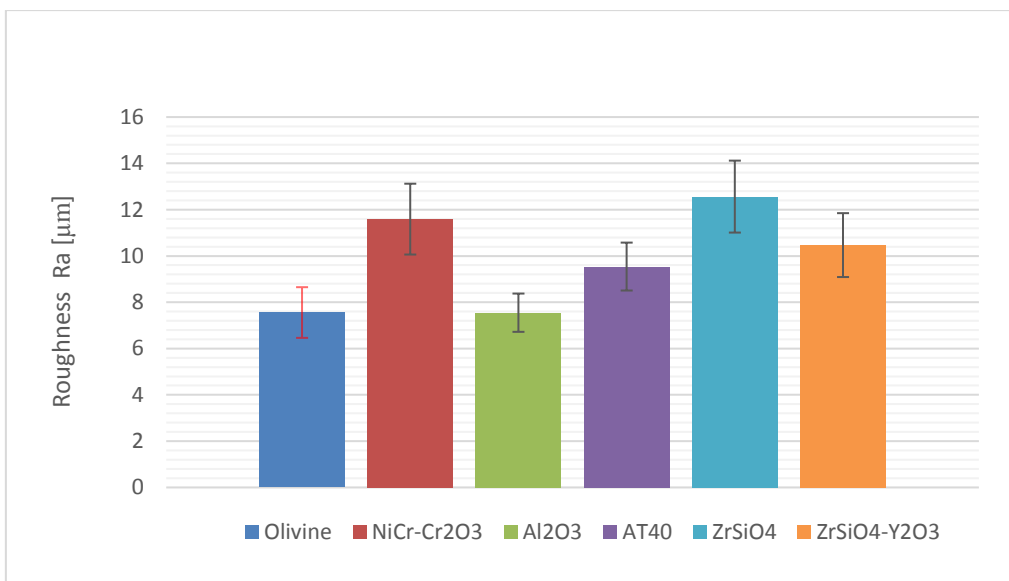
Pic. 31 Roughness of plasma sprayed coatings with standard deviation

3.2.4 TRIBOLOGY

Samples were tested at room temperature and at elevated temperatures of 200, 300, 400, 600 and 750 °C. The Tribometer THT-S-CE-0000 was used for the test. The tribometer is in the Pic. 32. This test can be performed in elevated temperatures up to 800°C. Sliding velocity is 0.02-5 m/s. Maximal rotational speed of the specimen is 500 rpm, maximal friction force is 10 N, maximal normal load is 10 N and the sphere diameters can be 1.5, 3, 6 and 10 mm.
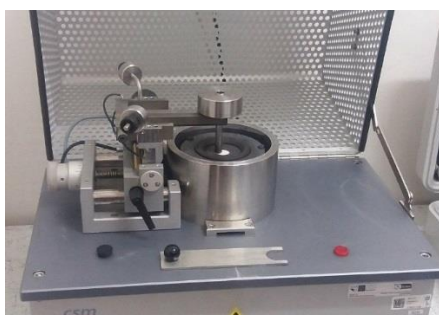
Pic. 32 Tribometer

Each sample was placed in the tribometer holder and secured by a nut to prevent the movement of the sample. Automatic arm holding the steel tube with Al_2O_3 pin was levered, so that there was no initial pressure on the sample. Afterwards, the load of 5 N was added before the test started. The setting of the tribometer test is written in the Tab. 21.

Tab. 21 The setting of the tribometer

Radius of wear [mm]	6
Linear speed [cm/s]	10
Normal load [N]	5
Number of laps	5000
Distance [m]	157.08
Time [s]	1570

Samples were tested unpolished. The difference between the coefficient of friction for polished and unpolished sample was just at the beginning of the test. The differences can be seen from the Pic. 33 and Pic. 34. The run-in period of the test was longer for polished sample. Polished sample showed lower initial friction. For the further testing, the unpolished samples were used.
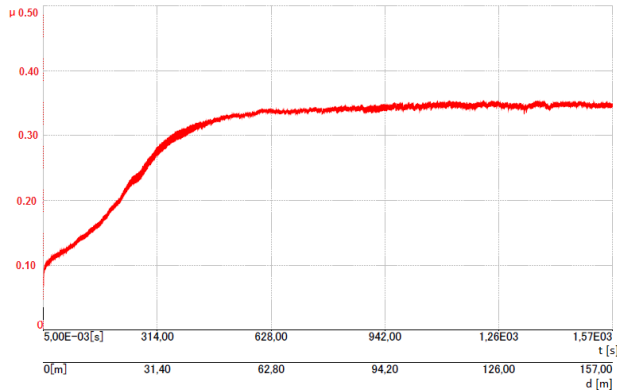
Pic. 33 The friction coefficient of polished Al₂O₃ coating
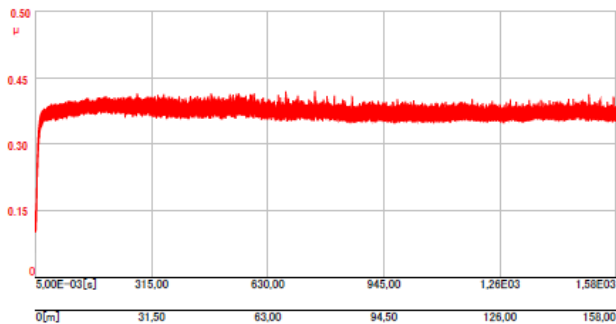
Pic. 34 The friction coefficient of unpolished Al₂O₃ coating

After the measurement was done. Samples were taken on the stereomicroscope. The width of the track was measured. The deviations in the measurements are negligible since the wear tracks were relatively wide and the porosity of the coatings also. A volume loss of the coatings was calculated from the width of the track according to the ASTM. The volume loss of the pin was calculated according to the ASTM also. Wear rates were calculated and are written in the attachments, which will be mentioned later. Wear rates are better for comparison with different studies since they are related to the force and distance of the test. To compare coatings in this thesis, the volume loss is used since the force and the distance was always the same for all the samples.

Results were compared with the results from profilometer. Unfortunately, not all the results from the profilometer corresponded with the results calculated according to ASTM equation. Some of the measured widths and depths were different from the stereo microscope values or actual worn samples. The deviation of the track depth

43

was sometimes in order of 0,5-1 mm. It might be due to decreased reflection of ceramic coatings.

I. Al_2O_3

For the Al_2O_3 coating, the measured coefficients of friction were higher than expected. High friction could be caused by porosity of the coating. The friction at different temperatures is shown in the Pic. 35. The measured start and stabilized coefficient of friction for different temperatures is written in the *Attachment 37* and the record from tribometer is shown in the Attachment 38. The coefficient of friction was 0.37, 0.4, 0.79, 0.73 and 0.75 at the temperatures 23 °C, 200 °C, 400 °C, 600 °C and 750 °C, respectively. The coefficient was increasing from the room temperature up to 400 °C. At the temperature 600 °C, the coefficient decreased slightly. Biggest change was between 200 and 400 °C. At 400 °C the coefficient was two times higher than at the temperature of 200 °C. This change could be caused by beginning of the oxidation. From the temperature 400 °C up to 750 °C the coefficient of friction remained quite the same.
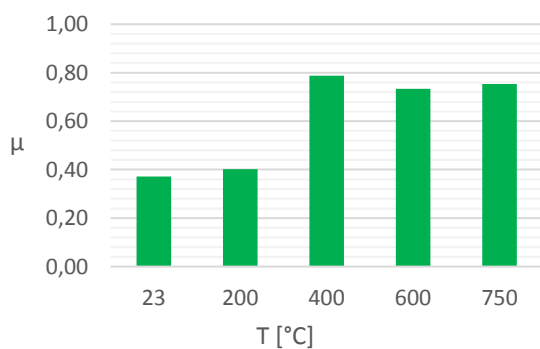
Pic. 35 Friction coefficient for Al_2O_3 coating at different temperatures

The coating volume loss, pin volume loss and the specific wear rate of the coating at different temperatures are written in the *Attachment 39*. Wear volume loss of Al2O3 coating at different temperatures is shown in the Pic. 36. The volume loss was higher as the temperature of the test increased. From the room temperature to 200 °C the coating volume loss increased 11 times, from 1.46 mm^3 to 18.1 mm^3. From 200 °C to 400 °C the coating volume loss increased to 26.84 mm^3. The coating volume

loss increased further to 28.96 mm^3 at the temperature 600 °C. The decrease of the coating volume loss was between 600 °C and 750 °C to the value of 22.16 mm^3. The difference between the volume losses was lower as the temperature increased and eventually started to decrease. The oxidation process could have influence on this result. The wear debris can also cause some changes in the testing. At higher temperatures, the debris can act differently, then at the room temperature.

As the coating volume loss changes, it signifies, that the material is quite unstable. This instability applied to all temperatures.
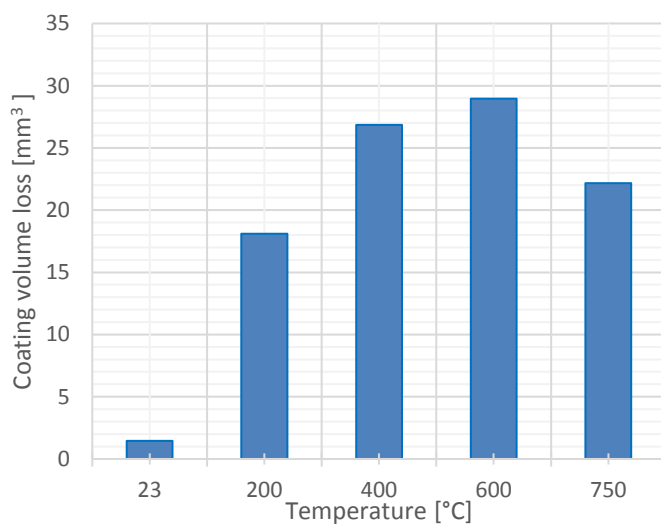
Pic. 36 Wear volume loss of Al$_2$O$_3$ coating at different temperatures

Pin volume loss from Al2O3 coating at different temperatures can be seen in the Pic. 37. It is possible to observe the increase of pin volume loss from 36.16 x10^{-3} mm^3 at room temperature to 301.02 x10^{-3} mm^3 at 200 °C. The pin volume loss decreased to 223.17 x 10^{-3} mm^3 when the temperature increased to 400 °C. The pin volume loss first decreased to 171.27 x 10^{-3} mm^3 and then increased to 211.48 x 10^{-3} mm^3 at the temperatures 600 °C and 750 °C, respectively. The wear of the pin from the coating Al$_2$O$_3$ is shown in the Attachment 40.
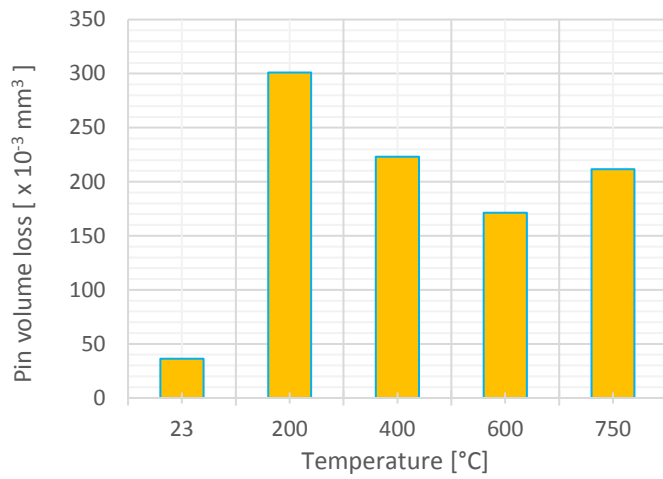
Pic. 37 Pin volume loss from Al$_2$O$_3$ coating at different temperatures

The wear tracks are shown in the Pic. 38. Wear mechanism for Al$_2$O$_3$ coating was mostly abrasive with a slight sign of adhesion. Wear debris from abrasion can be observed caught in the pores of the coating.

A)

B)

C)

D)

E)
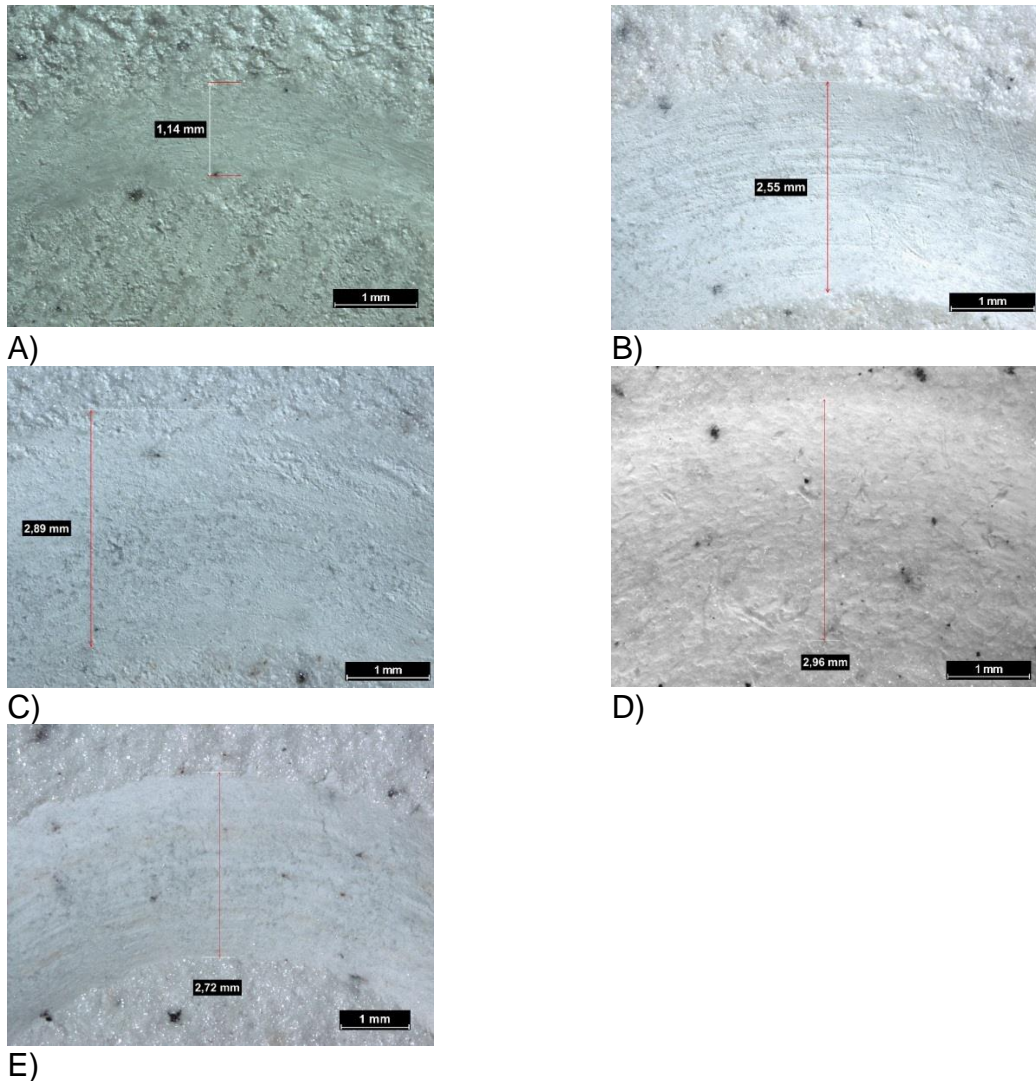
Pic. 38 Wear tracks of the Al_2O_3 coating at A) room temperature, B) 200 °C and C) 400 °C, D) 600 °C and E) 750 °C

II. Al_2O_3-TiO_2 (AT40)

The coefficient of friction for AT40 is also high. The results are shown in the Pic. 39. At the room temperature and at 200 °C it is two times higher than the coefficient of friction for Al_2O_3. The coefficient remains higher even at elevated temperatures. There is a slight increase of the coefficient of friction from 0.83 to 0.89 at the change of temperature from 23 °C to 200 °C. The coefficient starts to decrease above 200 °C. The coefficient of friction was 0.87, 0.82 and 0.81 at the temperature 400 °C, 600 °C and 750 °C, respectively. The coefficient even dropped under the starting value, from 0,83 at room temperature to 0.81 at 750 °C. The results are written

in the *Attachment 41* and the record of friction coefficient is shown in the Attachment 42.

During the test, the coefficient of friction remained quite stable. This implies to higher stability of the coating compared to Al_2O_3.
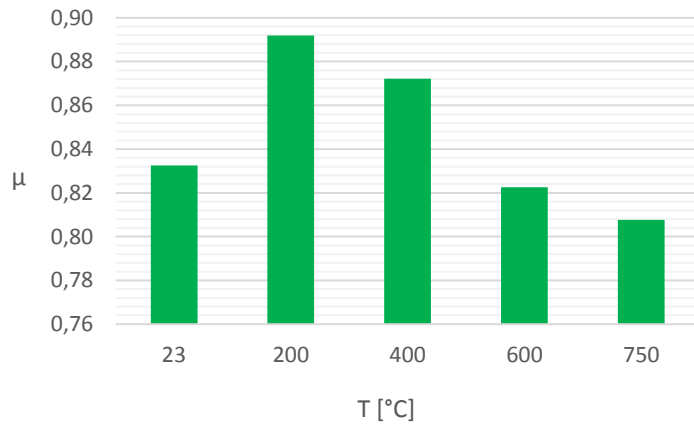
Pic. 39 Coefficient of friction for AT40 coating at different temperatures

Coating volume loss, pin volume loss and the specific wear rate of this coating at different temperatures is written in the Attachment 43. Wear volume loss of AT40 coating at different temperatures is shown in the Pic. 40. It is obvious that, as the coefficient of friction increased between the room temperature and 200 °C, the volume loss also increased. The change is comparable to the one of Al_2O_3. The change for TiO_2 is slightly bigger. At the room temperature, the coating volume loss was 1.63 mm^3. The coating volume loss increased to 10.66 mm^3 at 200 °C and decreased to 10.35 mm^3 at 400 °C. Afterwards, the coating volume loss increased slightly to 10.81 mm^3 and 11.44 mm^3 at the temperatures 600 °C and 750 °C. This shows quite a steady wear of the coating from 200 °C to 750 °C.
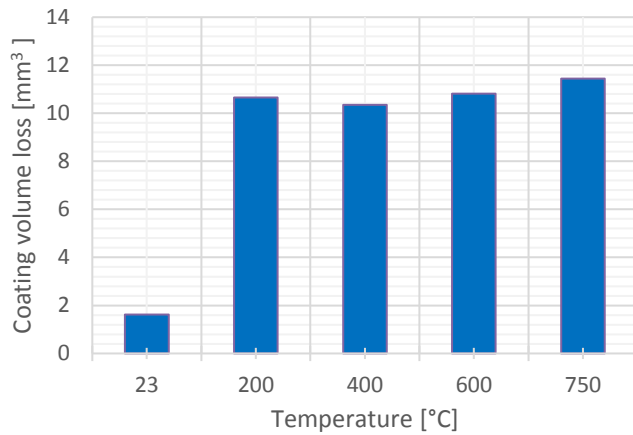
Pic. 40 Wear volume loss of AT40 coating at different temperatures

The pin volume loss was 26.52 x 10^{-3} mm^3, 159.88 x 10^{-3} mm^3, 97.9 x 10^{-3} mm^3, 130,7 x 10^{-3} mm^3 and 169.33 x10^{-3} mm^3 at the temperature 23 °C, 200 °C, 400 °C, 600 °C and 750 °C, respectively. The pin volume losses did not correspond to the disk volume losses at 400 °C, 600 °C and 750 °C. The pin volume loss decreased at 400 °C and then started to increase again at 600 °C and 750 °C. Pin volume loss from Al2O3 coating at different temperatures is shown in the Pic. 41.
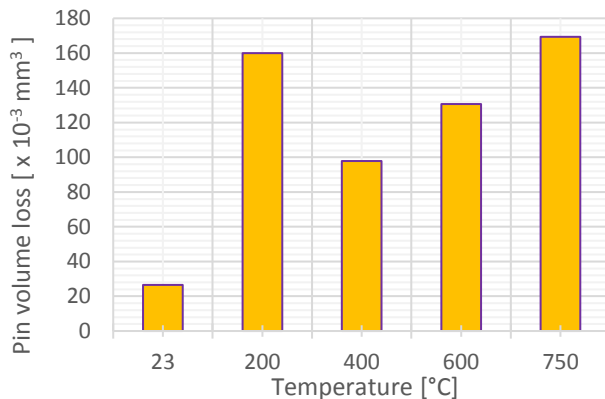
Pic. 41 Pin volume loss from AT40 coating at different temperatures

Wear tracks from the test for AT40 are shown in the Pic. 42. Wear mechanism of AT40 coating was abrasive. Abrasive particles were caught in the coating porosities. The abrasive grooves can be observed in the wear track.

On the pins, there are places, where the welded material can be observed. Some of the coating material was probably due to adhesive forces pulled out of the coating. This welded material usually signify the adhesion in the wear. These adhesive

spots can be mostly seen at higher temperatures. Wear of the pins from AT40 coating is shown in the Attachment 44.

A)

B)

C)

D)

E)
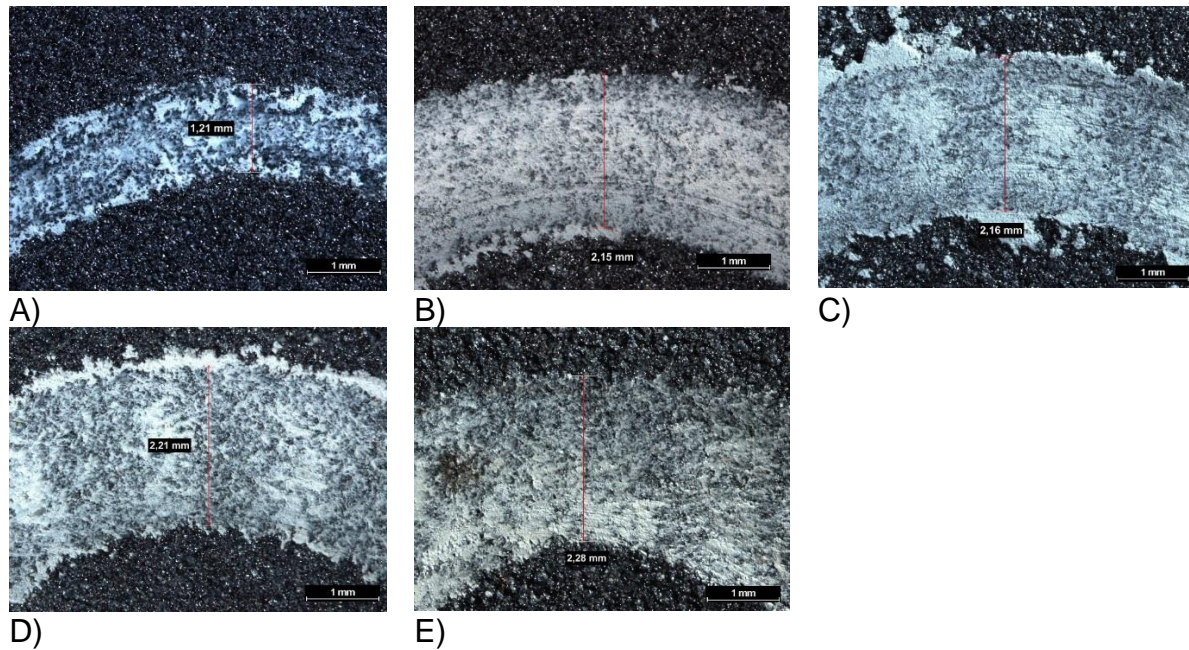
Pic. 42 Wear track of the AT40 coating at A) 23 °C, B) 200 °C, C) 400 °C, D) 600 °C and E) 750 °C

III.   Olivine

The coefficients of friction for olivine coatings were high and varied with the temperature nonlinearly. Coefficient of friction is shown in the Pic. 43. Coefficient of friction was 0.8 at the room temperature. This increased to 0.87 and 0.93, when the temperature increased to 200 °C and 400 °C, respectively. The coefficient decreased rapidly to 0.69 at the temperature of 600 °C. This decreasing tendency continued at 750 °C, when the value of the coefficient of friction dropped to 0.58. The results with the start friction coefficient and stabilized friction coefficient are written in the *Attachment 45* and the record is shown in the Attachment 46.

In higher temperatures, there could be a phase change from forsterite to protoenstatite or even to ferro-periclase.
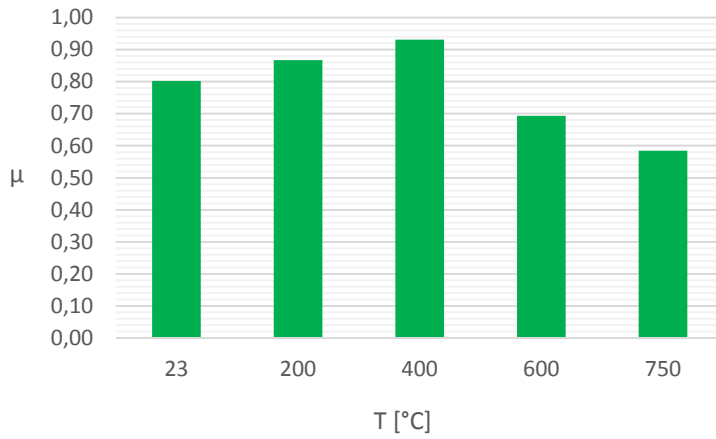
Pic. 43 Friction coefficient of olivine coating at different temperatures

The coating volume loss, pin volume loss and specific wear rate of the coatings at different temperatures are written in the Attachment 47. Wear volume loss of olivine coating at different temperatures is shown in the Pic. 44. The volume loss of the olivine coating at room temperature is 2.14 mm^3, which is higher than Al_2O_3 and AT40. There is an increase of the volume loss at 200 °C to 16.74 mm^3. After increase of the temperature to 400 °C, the volume loss decreased rapidly to 9 mm^3. This reduction of the volume loss continued to 3.26 mm^3 at 600 °C. At the temperature 750 °C, the coating volume loss increased again to 5,38 mm^3.
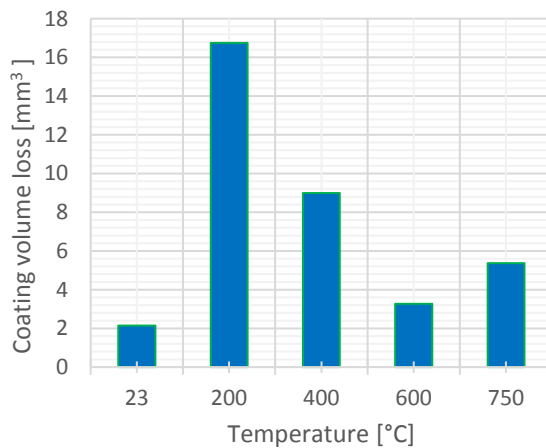
Pic. 44 Wear volume loss of olivine coating at different temperatures

Pin volume loss from olivine coating at different temperatures is shown in the Pic. 45. The pin volume loss increased and decreased at the similar character as the coating volume loss. When the volume loss of the coating increased, also the volume loss of the pin increased. As the wear volume of the coating decreased, the wear of

51

the pin decreased as well. The pin volume loss was 40.54 x 10^{-3} mm^3, 615.29 x 10^{-3} mm^3, 232.87 x 10^{-3} mm^3, 91.68 x 10^{-3} mm^3 and 126 x 10^{-3} mm^3 at the temperatures of 23 °C, 200 °C, 400 °C, 600 °C and 750 °C, respectively. It signifies a formation of some debris, which acts as lubricant between the coating and the pin. Wear of the pins is shown in the Pic. 47.
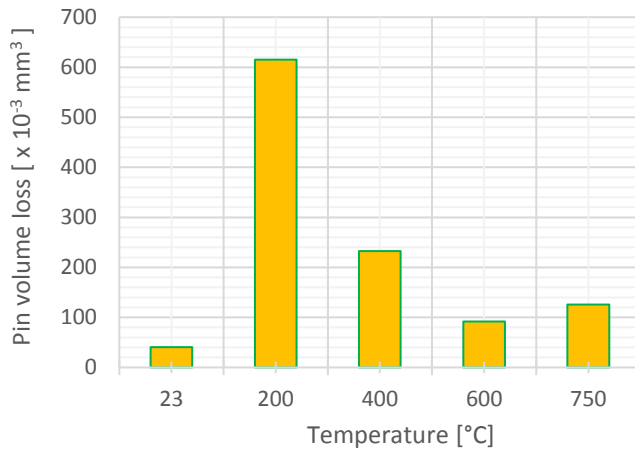
Pic. 45 Pin volume loss from olivine coating at different temperatures

Wear tracks of olivine coating can be seen in the Pic. 46. The grooves, consequence of the abrasive wear, can be seen at the 200 °C. Olivine coating at room temperature shows abrasive wear also. The grooves cannot be observed, but debris from abrasive wear can be clearly seen. At the temperature of 200 °C the wear was the most sever. With increasing temperature, the appearance of the grooves of abrasion decreases.

Olivine coating starts to show the adhesive wear at 200 °C and above. There can be observed places of the coating, which suffered from adhesion to the pin and consequential separation from the coating. The adhesion of the coating material to the pin is due to creation of local weld between these two materials. The occurrence of the local welds can be enhanced by higher temperatures. The zones of local welds are seen also on the worn pins in the Pic. 47.
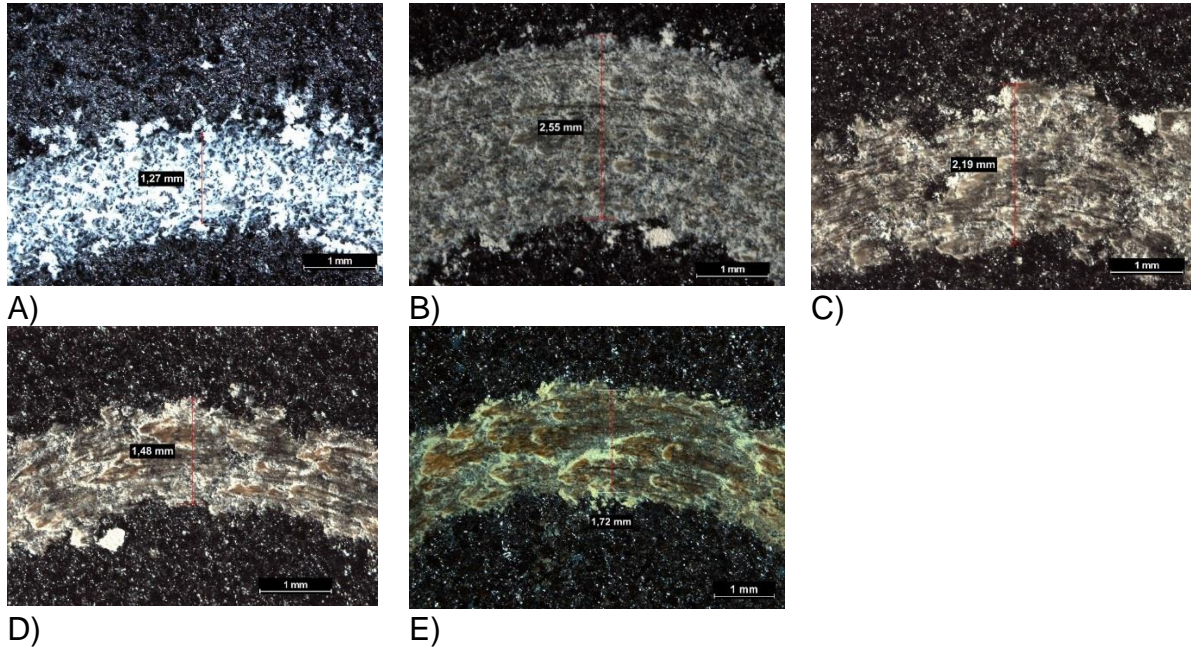
Pic. 46 Wear track of the olivine coating at A) 23 °C, B) 200 °C, C) 400 °C, D) 600 °C and E) 750 °C
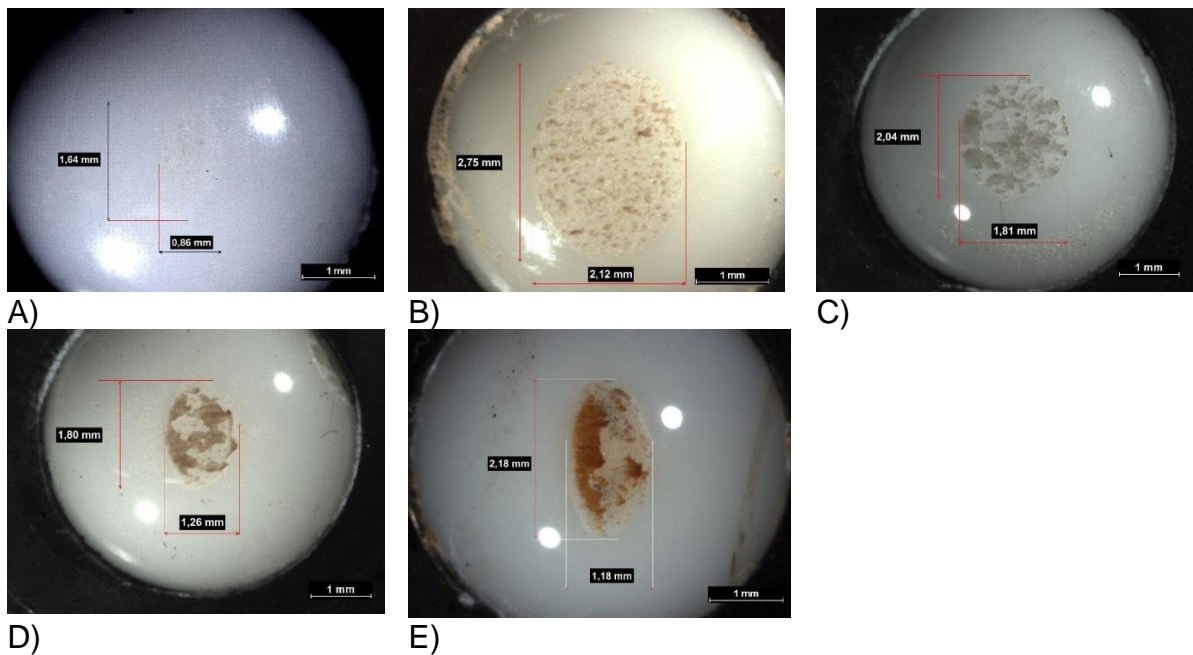
Pic. 47 Wear of the pin from olivine coating at A) 23 °C, B) 200 °C, C) 400 °C, D) 600 °C and E) 750 °C

IV. NiCr-Cr$_2$O$_3$

The coefficient of friction for the coating NiCr-Cr$_2$O$_3$ had decreasing tendency. Results of friction coefficient are shown in the Pic. 48. The coefficient of friction was 0.8, 0.63, 0.54, 0.38 and 0.35 at the temperatures 23 °C, 200 °C, 400 °C, 600 °C and 750 °C, respectively. The reduction rate of the friction remained similar up to 600 °C. There was slight decrease of the rate from the temperature 600 °C to 750 °C. The results with the start friction coefficient and stabilized friction coefficient are written in the *Attachment 48* and the record is shown in the Attachment 49.
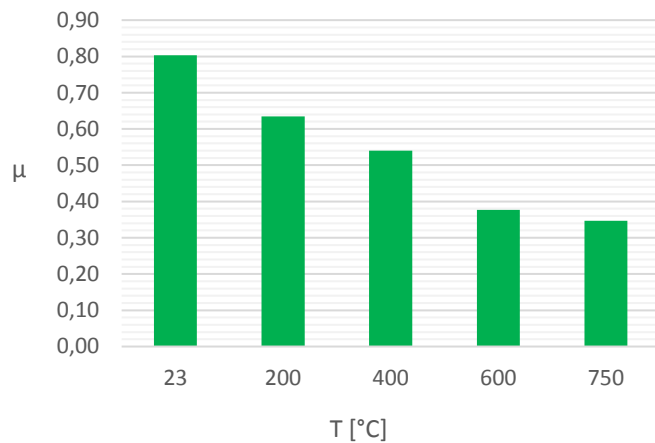
Pic. 48 Friction coefficient of NiCr-Cr$_2$O$_3$ coating at different temperatures

The coating volume loss, pin volume loss and specific wear rate of the coatings at different temperatures are written in the Attachment 50. Wear volume loss of NiCr-Cr$_2$O$_3$ coating at different temperatures is shown in the Pic. 49 The coating volume loss at the room temperature and 200 °C was 1.31 mm^3 and 0.65 mm^3, respectively. The coating volume loss increased further to 0.86 mm^3 at 400 °C and afterwards decreased to 0.51 mm^3 at 600 °C. At the temperature 750 °C, the volume loss decreased to 0.2 mm^3. Over all, the wear of the coating was the lowest from all the coating types.
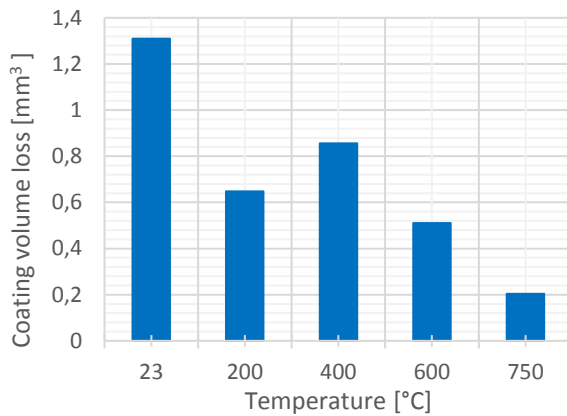
Pic. 49 Wear volume loss of NiCr-Cr$_2$O$_3$ coating at different temperatures

Pin volume loss from NiCr-Cr$_2$O$_3$ coating at different temperatures is shown in the Pic. 50. The wear of the pins did not correspond to the wear of the coatings. At the room temperature, the pin volume loss was 21.28 x 10^{-3} mm^3. This wear increased to 26.52 x10^{-3} mm^3 and 41.86 x10^{-3} mm^3 at 200 °C and 400 °C, respectively, even though the coating volume loss decreased. At the temperature 600 °C and 750 °C, the pin volume loss decreased to 30.53 x10^{-3} mm^3 and 28.98 x10^{-3} mm^3, respectively.
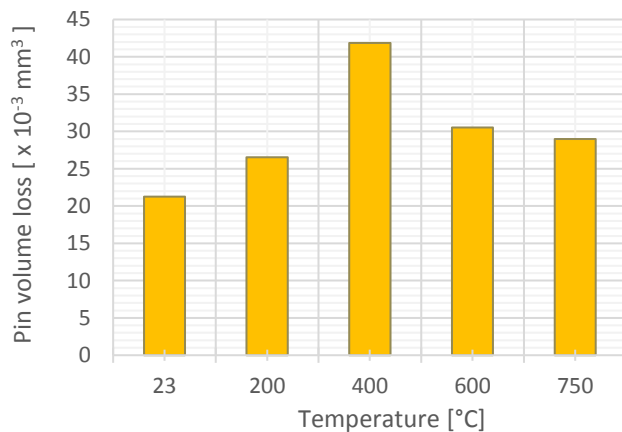
Pic. 50 Pin volume loss from NiCr-Cr$_2$O$_3$ coating at different temperatures

The wear tracks of the NiCr-Cr$_2$O$_3$ coating are shown in the Pic. 51. Wear of NiCr-Cr$_2$O$_3$ was partly abrasive and partly adhesive. Small grooves of the abrasive wear can be observed. The penetration of the pin in to the coating was not deep. This is the reason, why the abrasive grooves are hardly observed since the wear track is small. The adhesive wear can be seen at the room temperature. The signs of welded material, which was detached from the surface of the coating to the pin, can be observed. As the temperature increased, the wear became more abrasive. The wear

track is discrete at higher temperatures. This could be caused by vibrations of the pin on the coating. The vibrations might be due to high hardness and roughness of the NiCr-Cr$_2$O$_3$ coating.

The wear of the pins can be observed in the Attachment 51. Even though the biggest wear can be observed on the coating at room temperature, the highest wear of the pin was at 400 °C.

A)

B)

C)

D)

E)
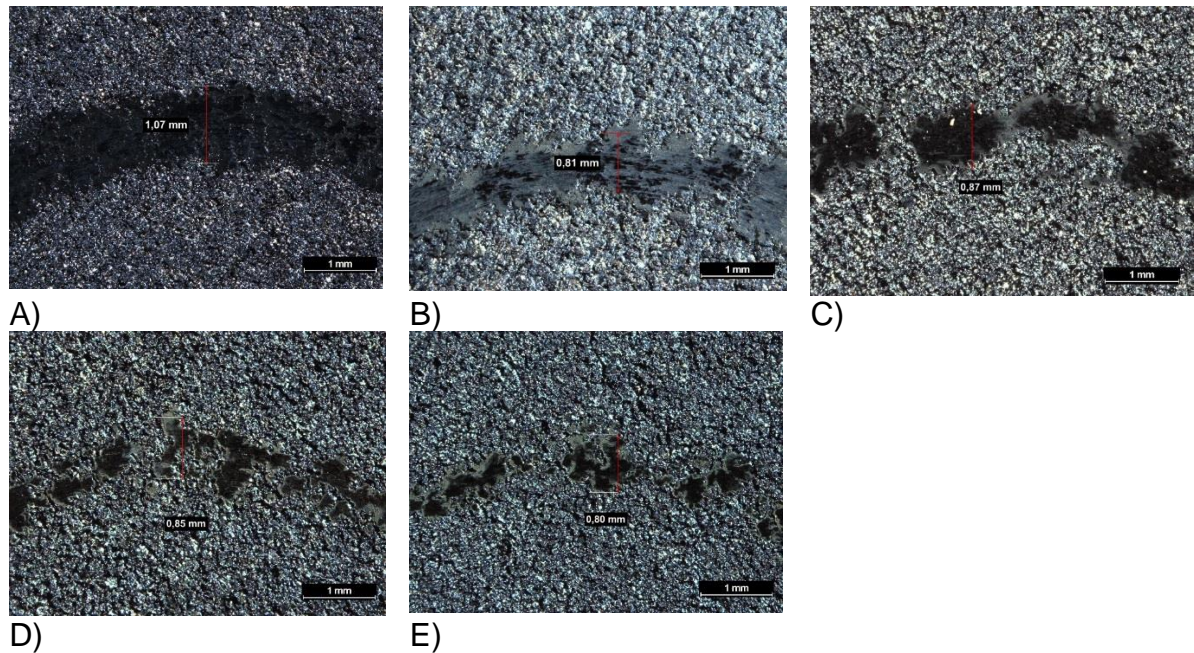
Pic. 51 Wear track of the NiCr-Cr$_2$O$_3$ coating at A) 23 °C, B) 200 °C, C) 400 °C, D) 600 °C and E) 750 °C

V.   ZrSiO$_4$

An analysis of the coating ZrSiO$_4$ was done on the scanning electron microscope. The coating in the as-sprayed condition is shown in the Pic. 52. Small pores can be observed on the right side in the picture. The splats are spread evenly. Small residual spherical droplets are observed on the coating. These are the particles, which separated from original droplets after the impact to the surface. These might be also the cause of porosity since they could be hardly covered by another splat. Some cracking on the splats can be also observed. This cracking starts on the edges of the splats. This can be due to quicker cooling, which causes stress in the splats. Also, this might be due to decomposition of ZrSiO$_4$ to ZrO$_2$ and SiO$_2$, as it was mentioned in the study [28], where the decomposition caused volume shrinkage up to 25 %. This process was marked as the cause of porosity up to 10 % in the study [28]. Also, the formation of monoclinic phase, which is formed by slow cooling, increases the volume of the splats. The splats sprayed first to the substrate also transforms first. This can lead to the stretching of the splats on the top, which are sprayed later.
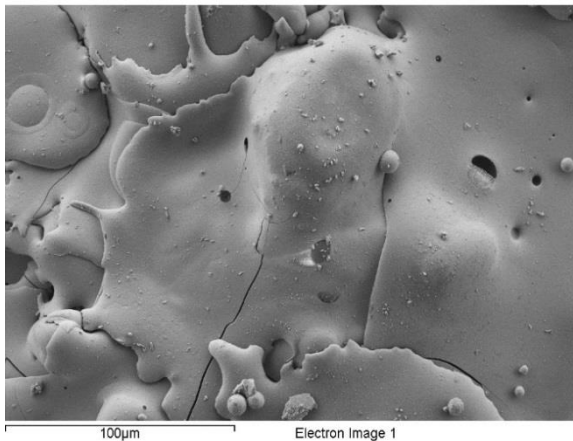
Pic. 52 SEM picture of as-sprayed ZrSiO$_4$ coating

The chemical analysis was done on the as-sprayed coating by the SEM. The results from the analysis are written in the Attachment 52. The analysis shows slightly higher atomic content of oxygen. This might signify oxidation process of the sprayed particles during the flight to the surface.

The wear tracks of the ZrSiO$_4$ coating, after the pin on disk test, are shown in the Pic. 53. The wear debris is present in the track. The chemical composition of the

wear track is written in the Attachment 53. From the composition, where the oxygen forms 69.5 atomic %, it is possible to say, there was no further oxidation of the coating during the wear test.
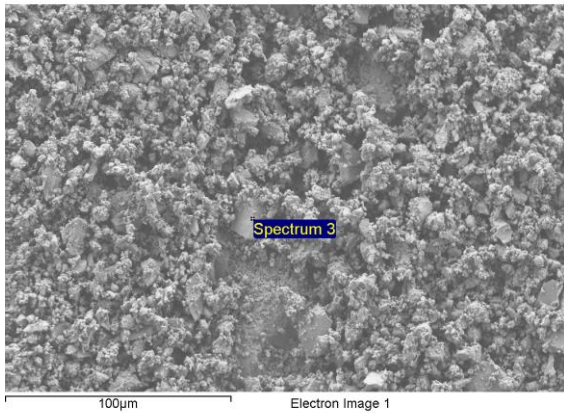
Pic. 53 SEM picture of wear track of ZrSiO$_4$ coating at 750 °C

The coefficient of friction was high for the coating ZrSiO$_4$. The results of friction coefficients are shown in the Pic. 54. At the room temperature, the coefficient of friction was 0.43. The coefficient doubled to 0.79 at 200 °C. This value also remained 0.79 at 400 °C. From the temperature 400 °C, the coefficient started to decrease to 0.74 and later to 0.71 at the temperature 600 °C and 750 °C, respectively. The same tendency of the coefficient of friction was observed for the second tested batch. The friction coefficient values were 0.56, 0.54, 0.53 and 0.5 for the temperatures 200 °C, 400 °C, 600 °C and 750 °C. The friction of the ZrSiO$_4$ coating was around 0.8 for all temperatures except the room temperature. The results with the start friction coefficient and stabilized friction coefficient are written in the *Attachment 54*. Records of friction are shown in the Attachment 55 for 1st batch and in the Attachment 56 for the 2nd batch.
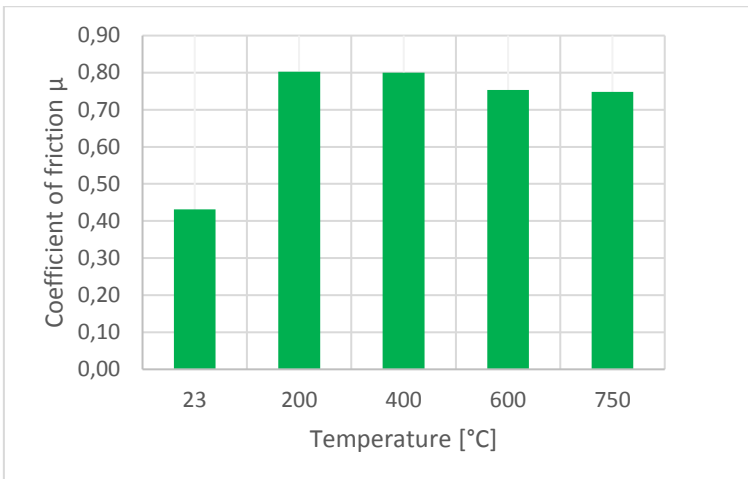
Pic. 54 Friction coefficient of ZrSiO$_4$ coating at different temperatures

The coating volume loss, pin volume loss and specific wear rate for ZrSiO$_4$ coating are shown in the Attachment 57 for the first batch and in the Attachment 58 for the second batch. Wear volume loss of ZrSiO4 coating at different temperatures is shown in the Pic. 55. The coating volume loss for first batch was 3.13 mm^3, 10.17 mm^3, 15.57 mm^3, 27.14 mm^3 and 26.2 mm^3 at the temperatures 23 °C, 200 °C, 400 °C, 600 °C and 750 °C, respectively. The coating volume loss for the second batch was 10.21 mm^3, 14.22 mm^3, 26.2 mm^3 and 43.62 mm^3 at the temperatures 200 °C, 400 °C, 600 °C and 750 °C, respectively.
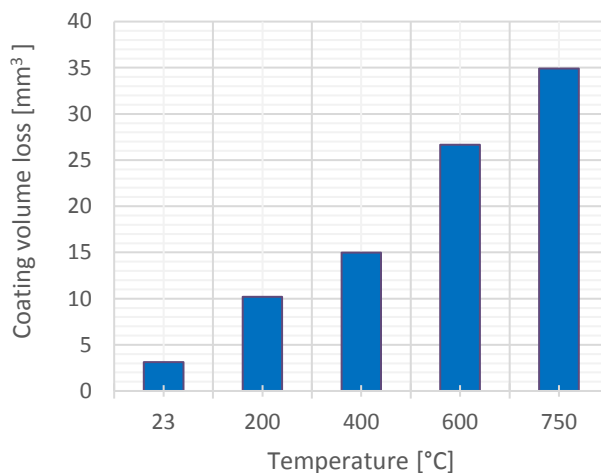
Pic. 55 Wear volume loss of ZrSiO$_4$ coating at different temperatures

Pin volume loss from ZrSiO$_4$ coating at different temperatures is shown in the Pic. 56.　The pin volume loss for the first batch was 45.31 x 10^{-3} mm^3, 119.95 x 10^{-3} mm^3,

181.23 x 10^{-3} mm^3, 230.42 x 10^{-3} mm^3 and 263.92 x 10^{-3} mm^3 at the temperatures 23 °C, 200 °C, 400 °C, 600 °C and 750 °C, respectively. For the second batch, the pin volume loss was 175.2 mm^3, 189.52 mm^3, 223.17 mm^3 and 289.21 mm^3 at the temperatures 200 °C, 400 °C, 600 °C and 750 °C, respectively.

The pin volume loss had increasing tendency similarly to the coating volume loss. This signifies quite instability of the ZrSiO$_4$ coating. The rate, which the wear increased with during increase of the temperature, remain quite the same. The same tendency was observed for the pins volume loss.
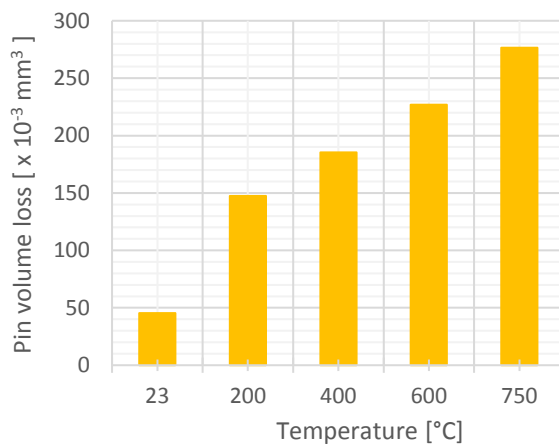
Pic. 56 Pin volume loss from ZrSiO4 coating at different temperatures

The wear track of the ZrSiO$_4$ coating is showing mainly the abrasive mechanism. The grooves with the remaining debris in the coatings can be easily observed in the Pic. 57 for the first batch and in the Attachment 59 for the second batch. There were not observed any deviations between the two batches.

The wear of the pins from the first batch is shown in the Attachment 60 and the wear of the pins from the second batch is shown in the Attachment 61. The surface of the pins showed mostly abrasive wear. The adhesive wear might be seen in the second batch at 750 °C. There are places, where the debris or the coating material welded to the pin surface. But, since the coating showed mainly the abrasive wear, it could be probably the bonded debris.
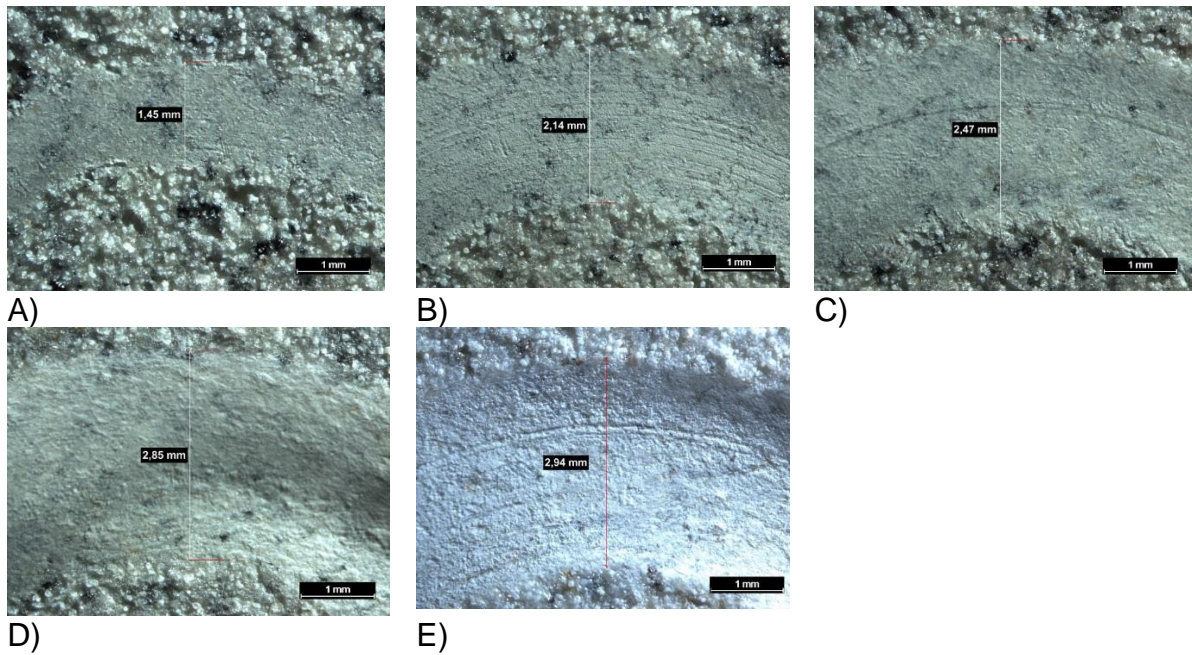
Pic. 57 Wear track of the ZrSiO₄ coating (1ˢᵗ batch) at A) 23 °C, B) 200 °C, C) 400 °C, D) 600 °C and E) 750 °C

VI.   ZrSiO₄-Y₂O₃

The coating $ZrSiO_4$-Y_2O_3 was evaluated by the SEM. The surface of the coating is shown in the Pic. 58. The surface morphology of the as-sprayed $ZrSiO_4$-Y_2O_3 coating is similar to the morphology of the $ZrSiO_4$ coating. The splats are evenly spread. There could be similar issue with the porosity, which could originate in the hardly accessible spots around the edges of the coating. There are cracks present in the coating as in the $ZrSiO_4$ coating. This signifies the thermal stress in the coating due to quick cooling. There is possibility to increase the preheating of the substrate before plasma coating.
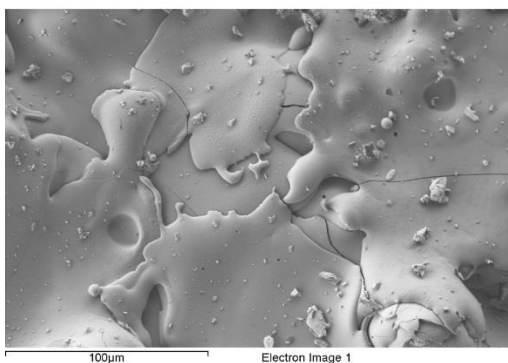
Pic. 58 SEM picture of ZrSiO₄-Y₂O₃ coating as-sprayed

The chemical composition of the as-sprayed coating is written in the Attachment 62. This chemical composition tells us, there might be more splats of $ZrSiO_4$ in the place, which were observed, and the Y_2O_3 particles are at different place or covered by the $ZrSiO_4$ splats.
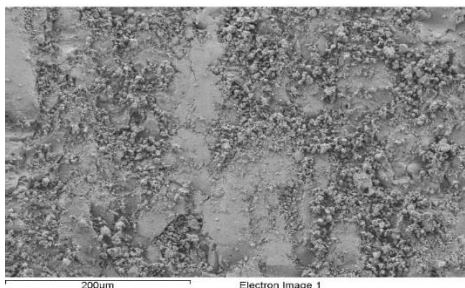
Pic. 59 SEM picture of wear track of ZrSiO$_4$-Y$_2$O$_3$ coating at 750 °C

The chemical composition was done on the worn surface, with remaining debris, after the wear test at 750 °C. The worn surface is shown in the Pic. 59. The amount of Yttrium increased. There is probably still more oxygen, then it should be. This shows on possible oxidation during the plasma spraying. The chemical composition of $ZrSiO_4$-Y_2O_3 after the wear test at 750 °C is written in the Attachment 63.

The coefficient of friction for $ZrSiO_4$-Y_2O_3 coating at different temperatures is shown in the Pic. 60. The coefficient did not change significantly at different temperatures as for the other coatings. The coefficient of friction for the first batch was 0.83, 0.79, 0.82, 0.78 and 0.85 at the temperatures 23 °C, 200 °C, 400 °C, 600 °C, 750 °C, respectively. The coefficient of friction for the second batch was 0.84, 0.83, 0.81 and 0.77 at the temperatures 200 °C, 400 °C, 600 °C and 750 °C, respectively. The average value for the coefficient of friction is 0.81 for all the temperatures. There is no exact tendency, which is followable for the coefficient of friction of $ZrSiO_4$-Y_2O_3. The results with the start friction coefficient and stabilized friction coefficient are written in the *Attachment 64*. Records of friction are shown in the Attachment 65 for 1st batch and in the Attachment 66 for the 2nd batch.
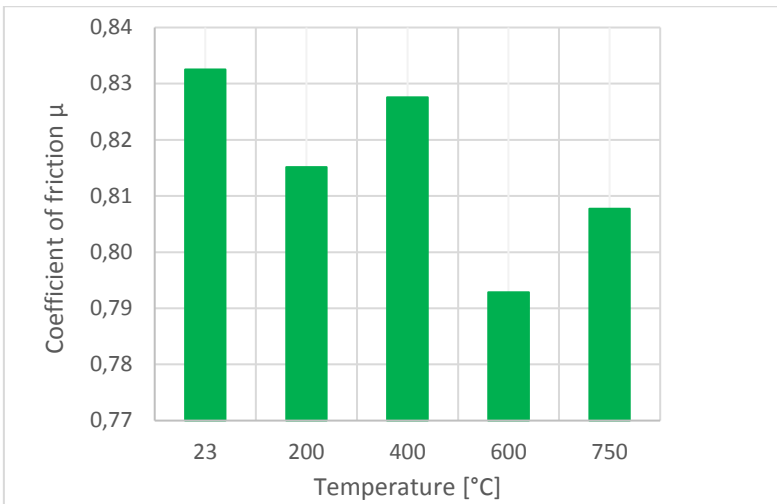
Pic. 60 Friction coefficient of ZrSiO$_4$-Y$_2$O$_3$ coating at different temperatures

The coating volume loss, pin volume loss and specific wear rate for ZrSiO$_4$-Y$_2$O$_3$ coating at different temperatures are written in the Attachment 67 for the first batch and in the Attachment 68. for the second batch. The coating volume loss for the first batch was 6.07 mm^3, 14.74 mm^3, 15 mm^3, 15.98 mm^3 and 8.18 mm^3 at the temperatures 23 °C, 200 °C, 400 °C, 600 °C, 750 °C, respectively. The coating volume loss of the second batch was 10.24 mm^3, 17.12 mm^3, 16.13 mm^3, 9.62 mm^3 at the temperatures 200 °C, 400 °C, 600 °C and 750 °C, respectively. At the beginning, the volume loss increased twice from the room temperature to 200 °C. Then, the volume loss remained the same, meaning, there was no change in the coating. The volume loss of the coating then dropped at the 750 °C. The value at the beginning and at the end were different only by 2 mm^3. Wear volume loss of ZrSiO$_4$-Y$_2$O$_3$ coating at different temperatures is shown in the Pic. 61.
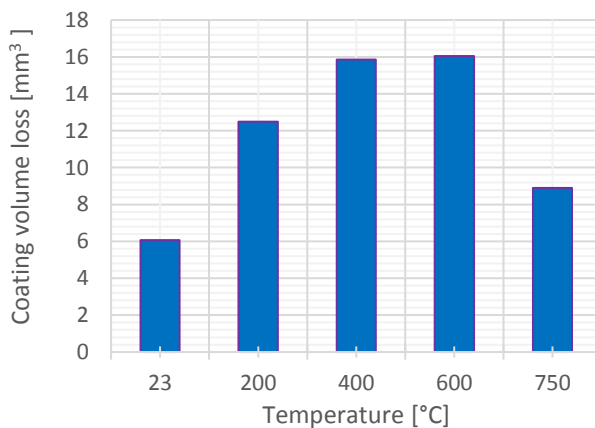
Pic. 61 Wear volume loss of ZrSiO$_4$-Y$_2$O$_3$ coating at different temperatures

Pin volume loss from $ZrSiO_4$-Y_2O_3 coating at different temperatures is shown in the Pic. 62. The pin volume loss for the first batch and second batch corresponded to the coating volume loss for the matching batches. At 23 °C the pin volume loss was 41 x 10^{-3} mm^3. It increased to 165.5 x 10^{-3} mm^3, 165.5 x 10^{-3} mm^3 and 159.88 x 10^{-3} mm^3 at the temperature 200 °C, 400 °C and 600 °C, respectively. Then, the value dropped to 90.48 x 10^{-3} mm^3 at 750 °C. For the second batch, the values were similar. The pin volume loss was 159.87 x 10^{-3} mm^3, 175.2 x 10^{-3} mm^3, 145.59 x 10^{-3} mm^3 and 112.69 x 10^{-3} mm^3 at the temperatures 200 °C, 400 °C, 600 °C and 750 °C.
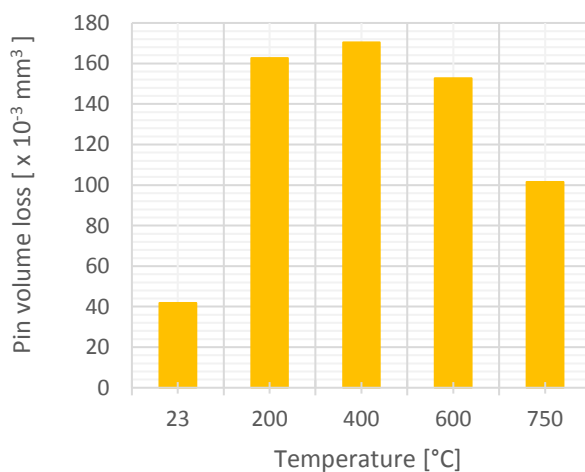
Pic. 62 Pin volume loss from ZrSiO₄-Y₂O₃ coating at different temperatures

Wear of the $ZrSiO_4$-Y_2O_3 coating from the first batch is shown in the Pic. 63 and wear of the coating from the second batch is shown in the Attachment 69. At the beginning, the coating shows more abrasive wear. Abrasive grooves can be observed. As the temperature increases to 750 °C, signs of adhesive wear can be observed. This might signify again some kind of lubricating debris. This debris might work as a preventing factor against the wear since it may prevent the contact of the coating and the pin.

The similar wear can be observed for the pin wear in the Attachment 70 (1st batch) and in the Attachment 71 (2nd batch).
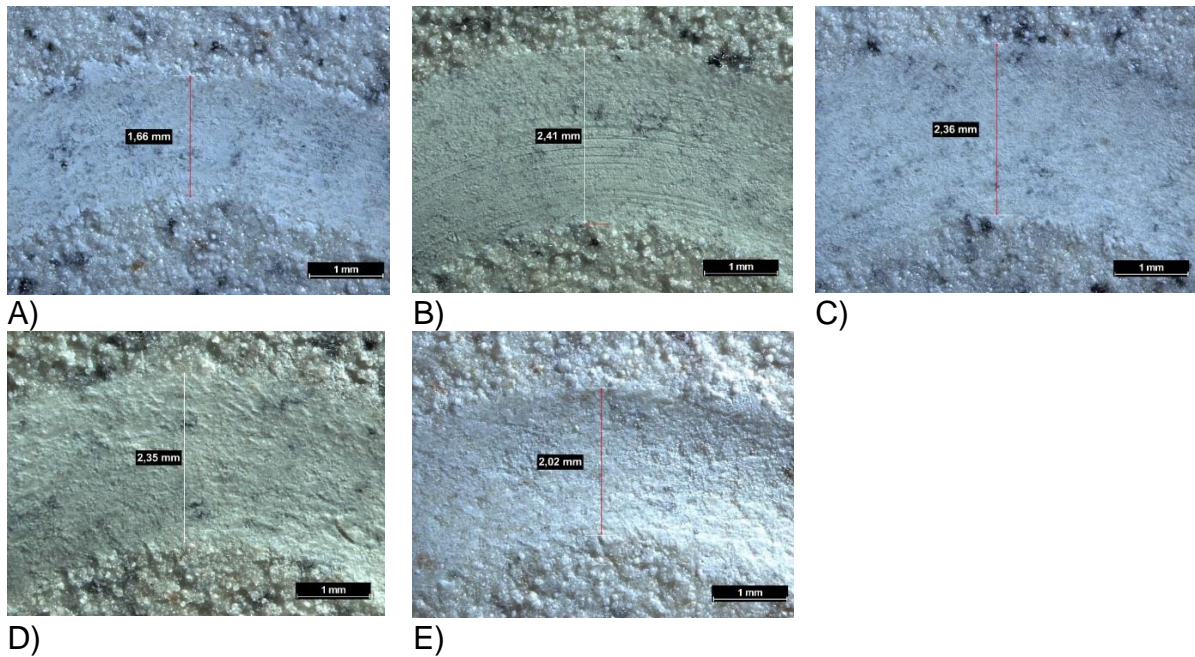
Pic. 63 Wear track of the ZrSiO$_4$-Y$_2$O$_3$ coating (1st batch) at A) 23 °C, B) 200 °C, C) 400 °C, D) 600 °C and E) 750 °C
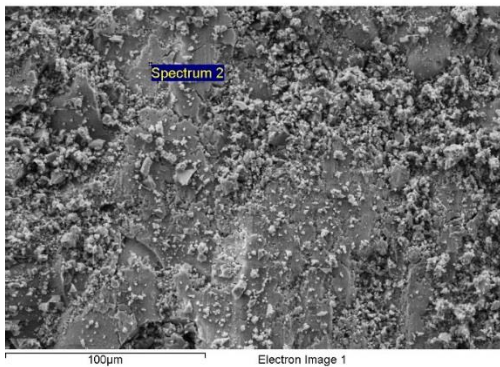
Pic. 64 SEM picture of ZrSiO$_4$-Y$_2$O$_3$ coating wear track after wear test at 750 °C

The chemical composition was done on the wear debris from the wear test at 750 °C. The composition showed higher amount of the yttrium than it was observed before. This debris seems as adherent one which forms a lubricating layer on the surface. It might be some form of oxide layer. This might be the reason, why the wear at higher temperatures was lower for the ZrSiO$_4$-Y$_2$O$_3$ than for the ZrSiO$_4$. The area, where the chemical composition was done, is shown in the Pic. 64. The chemical composition is written in the *Attachment 72*.

3.3 SUMMARY

The samples, used for wear testing, were not polished to simulate the sever wear conditions of dusty environment at elevated temperatures. The severity of the wear can be observed by elevated volume loss of the tested coatings. The results of the coatings volume loss are shown in the Pic. 65.
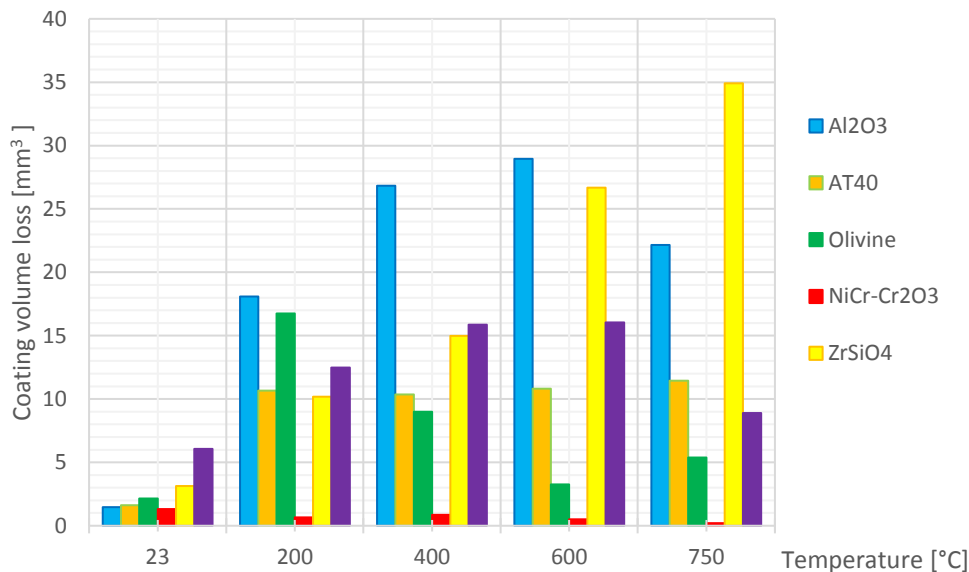
Pic. 65 Coating volume loss for tested coatings at different temperatures

The highest wear and correspondingly lowest wear resistance showed the Al_2O_3 coating. The wear increased rapidly at the beginning, when compared to other coatings. The highest increase of the wear was in between the room temperature and the 200 °C. After 200 °C, the rate, which the wear increased with, started to drop. The wear tended to decrease between 600 °C and 750 °C.

On the other side, there was the $NiCr-Cr_2O_3$ coating. This composite coating was chosen for comparison with the ceramic coatings. This coating had the lowest wear volume loss from all the tested coatings and remained almost the same. There was not seen high increase or decrease of the wear, when compared to the rest of the coatings.

The coating AT40 was expected to have improved wear resistance compare to the Al_2O_3 material. These expectations were fulfilled. The AT40 had two times lower

wear than A_2O_3 from the temperature 200 °C and higher. The wear remained quite same with just slightly increasing tendency.

Olivine coatings had unexpected evolution. The wear increased significantly when the temperature changed from 23 °C to 200 °C. Similar increase of wear had Al_2O_3 coating. Afterwards, the wear of olivine started to decrease up to the temperature of 600 °C and increased again in the end, when the temperature increased from 600 °C to 750 °C. Olivine had the second lowest wear at elevated temperatures above 400 °C after the $NiCr-Cr_2O_3$ coating.

The wear of $ZrSiO_4$ coating had increasing tendency. The increase was steady. The $ZrSiO_4$ coating had the highest wear from all the coatings at elevated temperatures.

Opposite to the $ZrSiO_4$ coating, the $ZrSiO_4-Y_2O_3$ had in the elevated temperatures decreasing tendency. The wear was for these two coatings the most similar at 400 °C.

The difference in pin volume loss for each material is shown in the Pic. 66. The highest wear experienced the pin from Olivine coating at 200 °C. At this temperature, the wear was two times higher than any other pin wear. At the same temperature the second biggest wear had the pin from Al_2O_3 coating. The pin from $ZrSiO_4$ coating had increasing wear as the coating itself. The wear of pin from $ZrSiO_4-Y_2O_3$ coating was first increasing and then it started to drop from 400 °C and higher. The wear of the pins from Al_2O_3 and AT40 coatings increased from room temperature to 200 °C significantly. It started to drop from 200 °C to 400 °C and above 400 °C it started to increase again.
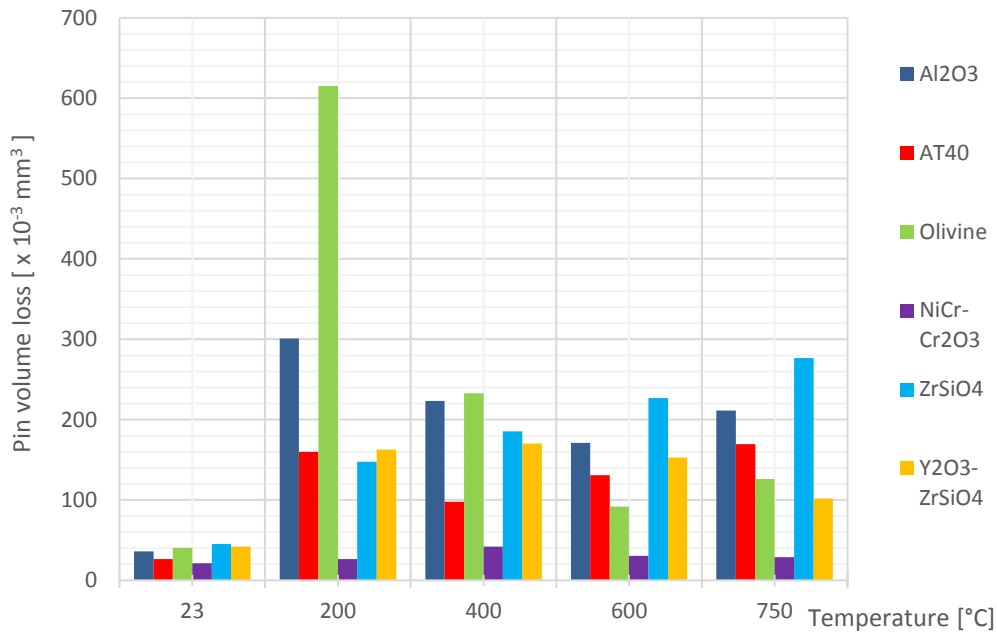
Pic. 66 The comparison of Al₂O₃ pin volume loss for different coating materials at different temperatures.

The coefficient of friction for each coating is shown in the Pic. 67. The lowest friction had the NiCr-Cr₂O₃ coating at higher temperatures. The lowest friction had the Al₂O₃ and ZrSiO₄ at room temperature. The friction of the Al₂O₃ coating remained lower also at 200 °C. the ZrSiO₄ coating already increased at 200 °C. The friction of olivine increased from 0.8 to 0.93 from room temperature to 400 °C and then decreased to 0.585 at 750 °C. The rest of the coefficients of friction held around 0.7-0.8.
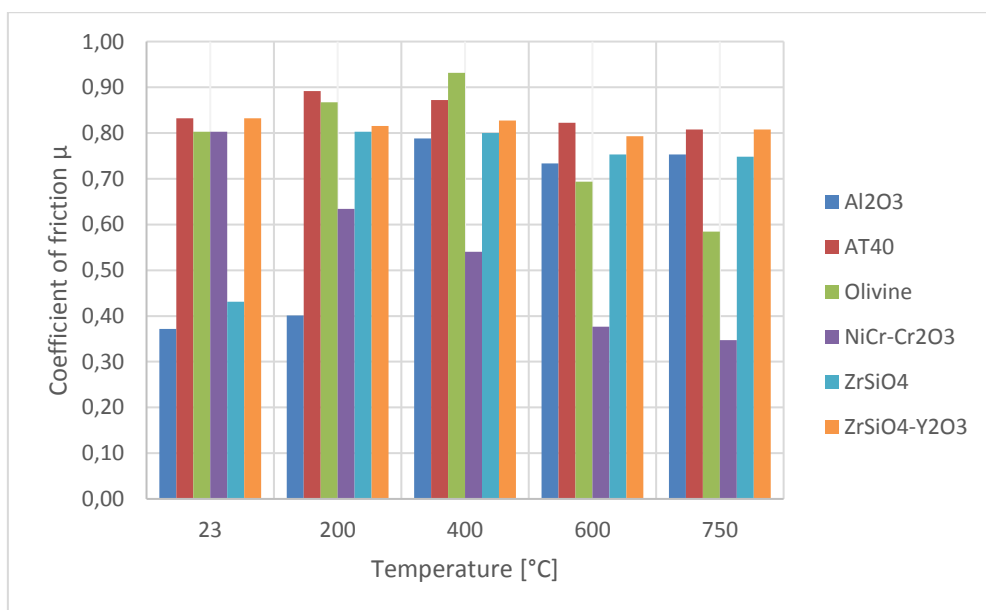
Pic. 67 The coefficient of friction of different coatings

68

The differences between the $ZrSiO_4$ and $ZrSiO_4$-Y_2O_3 coatings are shown in the Attachment 73. From the picture it is possible to say, that the structure is more complex for the $ZrSiO_4$ coating. There are less particles, which separated from the droplets after the impact to the surface during plasma spraying. There can be observed also the imperfectly melted particles. This can cause the porosities of the coatings, causing cracking and heterogenic properties of the coatings. The unmelted particles are visible in the Attachment 74. Part of the powder was melted, and some particles stayed in unmelted state. Since these particles are in both coating, the Y_2O_3 powder can be excluded. The unmelted particles could be the decomposed ZrO_2 particles. The melted particles called splats are observed as well. Other coatings were also porous. Lower porosity had NiCr-Cr_2O_3 coating.

4. CONCLUSION

In this thesis, there were 6 different coatings tested for wear properties at different temperatures. The tested coatings were Al_2O_3, AT40, Olivine, $NiCr-Cr_2O_3$, $ZrSiO_4$ and $ZrSiO_4-Y_2O_3$. These coatings were tested at room temperature, 200 °C, 400 °C, 600 °C and 750 °C. The wear tracks of the coatings after the test were evaluated. Volume loss from the tribometric test was calculated for the coatings and for the pins. The coefficient of friction was recorded for each coating at all testing temperatures. These values were compared. Hardness of the coatings was measured in as-sprayed condition and after the heat treatment at 650 °C, at which the samples stayed for 10 hours. The heat treatment had an impact on the hardness of the coatings. The roughness of the coatings was also measured in as-sprayed condition. The structure of the as-sprayed coatings was evaluated.

The wear test temperature significantly influenced the wear of the coatings. The wear increased at elevated temperatures.

The highest wear had coatings Al_2O_3 and $ZrSiO_4$. Successful increase of wear resistance was observed for Al_2O_3 by addition of TiO_2 and for $ZrSiO_4$ by addition the stabilizing Y_2O_3. Steady wear had the coating AT40. Olivine coating showed improved wear resistance in higher temperatures. The lowest wear had $NiCr-Cr_2O_3$ coating.

Further increase of wear resistance could be improved by lowering the porosity of the coatings. The coatings would be more compact. This could prevent the wear of the coatings. Also, the corrosion could be improved by lower porosity.

Change of spraying parameters could help decrease the porosity. Spraying distance could be shorter, so that particles are completely melted when they impact the substrate. Higher preheating temperature of the substrate could lower the porosity. These parameters could lead to a phase change in the coatings, which also influence the stability and porosity of the coatings.

BIBLIOGRAPHY

[1]   Meetham G. W., "High-temperature materials- a general review," *Journal of Materials Science, Chapman and Hall Ltd., Derby, UK,* no. 26, pp. 853-860, 1991.

[2]   Vickers L., A. Riessen , W. D. A. Rickard, fire-Resistant Geopolymers: Role of Fibres and Fillers to Enhance Thermal Properties, New York: Sprienger Briefs in Material, 2015, pp. 13.

[3]   Ergun H., K. Aydinol, et. al., „Design of a high temperature erosion apparatus for testing of boiler tubes," *Turkish Journal of Engineering and Environmental Sciences,* pp. 178-185, 29 07 2013.

[4]   Group S., „High-alloy Materials for Boiler Tubes," Mannesmann Stainless tubes, 02 2009. [Online]. Available: https://www.mannesmann-stainless-tubes.com/files/smst-tubes_boiler_brochure_2009.pdf. [Přístup získán 29 7 2018].

[5]   Erickson L. C., a et. al., „Cohesion in plasma sprayed coatings -a comparison between evaluation methods," *Wear,* 2214 (1), Vol.. 30-7, 1998, Elsevier.

[6]   McPherson R., A review of microstructure and properties of plasma sprayed ceramic coatings, Department of Materials Engineering, Monash University, Clayton, Victoria 3168: Surface and coating technology, 39/40, 173-181, 1989.

[7]   Hrabovsky M., „Water-stabilized plasma generators," *Pure Applied Chemistry,* sv. 70, Vol.. 2, pp. 1157-1162, 1998.

[8]   Pawlowski L., „Suspeension and solution thermal spray coatings," *Surface and Coating Technology,* sv. 203, Vol.. 19, pp. 2807-2829, 2009.

[9]   Mušálek R., et. al., „Feasibility of suspension spraying of yttria-stabilized zirconia with water-stabilized plasma torch," *Surface and Coatings Technology,* sv. 268, pp. 58-62, 2015.

[10]   International A., Material data sheet P91/T91, Essen: ThyssenKrupp Material International, 2011. Available at http://www.s-k-h.com/media/de/Service/Werkstoffblaetter_englisch/Kesselrohre_ASTM/P91_T91_engl.pdf

[11] „ThyssenKrupp Material International, Werkstoffblatter, Stahlkontor Hahn," Stahlkontor Hahn, 2011. [Online]. Available: http://www.s-k-h.com/media/de/Service/Werkstoffblaetter_englisch/Kesselrohre_ASTM/P91_T91_engl.pdf. [Přístup získán 17 10 2017].

[12] Serre P., e. al., „Mechanical behavior of coated T91 steel in contact with lead–bismuth liquid," *Surface & Coatings Technology, ScienceDirect, No.* 205, Vol.. 19, June 25 2011.

[13] Z. Česánek, Žárově stříkané povlaky používané v korozně působícím prostředí, Plzeň: Západočeská Universita v Plzni, 2015.

[14] Branagan D.J., e. al., „High Performance Nanoscale Composite Coatings For Boiler Applications," 2017. [Online]. Availabe at https://nanosteelco.com/images/uploads/resources/high_performance_coat_boiler_apps.pdf. [Přístup získán 19 9 2017].

[15] Sidhu T. S., S. Prakash, R. D. Agrawal, „A comparative Study of Hot Corrosion Resistance of HVOF Sprayed NiCrBSi and Stellite 6 Coated Ni-Base Superalloy at 900 °C," *Journal of Thermal Spray Technology,* 2006.

[16] Souza V. D., A. Neville, „Mechanisms and Kinetics of WC-Co-CrHigh Velocity," *Journal of Thermal Spray Technology,* sv. 1, Vol.. 15, pp. 1, 15, 106-117, 2006.

[17] Uusitalo M. A., e. al., „ElevatedTemperature Erosion-Corrosion of Thermal Sprayed Coatings in Chlorine Containing Environments,," *Wear,* sv. 252, pp. Vol. 252, p. 586-594, 2002.

[18] „Olivine Powder and Olivine Sand ((MgFe)2SiO4)," Reade Inetrnational Corp., 2016. [Online]. Available at: http://www.reade.com/component/zoo/olivine-powder-and-olivine-sand-mgfe-2sio4. [Přístup získán 11 11 2017].

[19] David B., „Olivine Mineral Data, Mineralogy Database," 1997-2014. [Online]. Available: http://webmineral.com/data/Olivine.shtml#.WiEUhlvWyM_. [Přístup získán 2 5 2018].

[20] Suzuki I., „Thermal expansion of Periclase and olivine, and their anharmonic properties," 27 January 1975. [Online]. Available at: https://www.jstage.jst.go.jp/article/jpe1952/23/2/23_2_145/_pdf. [Přístup získán 7 July 2018].

[21]   Eppelbaum L., „Thermal properties of Rocks and Density of fluids," v *Applied Geothermics*, Berlin Heidelberg, Springer-Verlag, 2014, pp. 99-144.

[22]   Ctibor P., et. al., „Dielectric and mechanical properties of plasma-sprayed olivine," *Romanian Reports in physic, no.* 67, Vol.. 2, pp. 600-616, 2015.

[23]   Cojocaru C., et.al., „Atmospheric Plasma Sprayed Forsterite (Mg2SiO4) Coatings: An Investigation of the Processing-Microstructure-Performance Relationship," *Journal of Thermal Spray Technology, no.* 22, Vol.. 2-3, pp. 145- 152, 2013.

[24]   „Zirconium Silicate (ZrSiO4) Zircon powder," Reade International Corp., 2016. [Online]. Available: http://www.reade.com/products/zirconium-silicate-zrsio4-zircon-powder. [Přístup získán 3 2 2018].

[25]   „Zircon (Zirconium Silicate, ZrSiO4)," 18 9 2009-2017. [Online]. Available: https://www.makeitfrom.com/material-properties/Zircon-Zirconium-Silicate-ZrSiO4. [Přístup získán 20 3 2018].

[26]   Kaiser A., et. al., „Thermal stability of zircon (ZrSiO4)," *Journal of the European Ceramic Society, Science Direct,* Vol.. 28, pp. 28, 2199-2211, 2008.

[27]   Jahanmir S., Friction and wear of ceramics, Gaithersburg, Maryland: National Institute od Standards and Technology, 1994.

[28]   Sun C., et. al., „Effect of Y2O3 on the oxidation resistant of ZrSiO4/SiC coating prepared by supersonic plasma spraying technique for carbon/carbon composites," *Surface and Coatings Technology,* sv. 235, pp. 127-133, 2013.

[29]   Suzuki M., et. al., „Structure Control of Plasma Sprayed Zircon Coating by Substrate Preheating and Post Heat treatment," *Material Transactions, Japan Thermal Spraying Society,* Vol.. No. 3, Vol. 46, No. 3,pp. 669-674, 2005.

[30]   Alexandra R., „Thermal properties of plasma-sprayed ZrSiO4 material," *Surface and Coating Technology,* Vol.. 64, pp. 47-51, 1994.

[31]   Suzuki M., S. Sodeoka, et. al., „Zircon-Based Ceramics Composite Coating for Environmental Barrier Coating," *Journal of Thermal Spray Technology,* Vol.. 3, pp. 17, pp. 404-409, September 2008.

[32]   „Material product data sheet, Yttrium Oxide Thermal Spray Powder, Oerlikon Metco," 2014. [Online]. Available at: https://www.oerlikon.com/ecomaXL/files/metco/oerlikon_DSMTS-

0122.1_Pure_Yttria_Powders.pdf&download=1. [Přístup získán 7 July 2018].

[33]   „Aluminum Oxide, Al2O3 Ceramic Properties,“ Accuratus, 2013. [Online]. Available at http://accuratus.com/alumox.html [Přístup získán 15 7 2018].

[34]   „Alumina, Advanced ceramic solutions for extreme environments,“ International Syalons (Newcastle) Limited, 2001-2017. [Online]. Available at: http://www.syalons.com/advanced-ceramic-materials/alumina-ceramics/. [Přístup získán 5 12 2017].

[35]   „CeramTec Products and Applications;CeramTec,“ CeramTec,, 6 2018. [Online]. Available at https://www.ceramtec.com/products/. [Přístup získán 13 6 2018].

[36]   „Ceramics from Keranova AB, Keranova,“ Keranova AB, Emmylundsvagen 16, January 2017. [Online]. Available: http://www.keranova.se/Engelsk/Exceltabell_E.htm. [Přístup získán 27 12 2017].

[37]   Shirai T., et. al., „Structural Properties and Surface Characteristics on aluminum Oxide Powders,“ セラミックス基盤工学研究センター年報, Ceramics Research Laboratory, Nagoya Institute of Technology,Hon-machi 3-101-1, Tajimi, Gifu 507-0033, JAPAN, sv. Vol. 9, pp. Vol. 9, p. 29-31, 2009.

[38]   Fiedler H., „The Effect of Structure on the Thermal Conductivity of Plasma Sprayed Alumina, Material Research Society,“ v Vol. 30 (Symposium L - Plasma processing and synthesis of material 1), 1983.

[39]   Ma W. , Dong H., Ceramic thermal barrier coating materials, 1518 Walnut Street, Suite 1100, Philadelphia, 1518 Walnut Street, Suite 1100,: Woodhead Publishing, 1518 Walnut Street, Suite 1100, Philadelphia, USA, 2011.

[40]   Marcinauskas L., et. al., „Effect of torch power on the microstructure of plasma sprayed Al2O3 coatings,“ Surface and Interface analysis, no. 48, Vol.. 7, 2016.

[41]   Sathish S., Geetha M., „Microstructure and corrosion Behaviour of Plasma Sprayed Bilayered Ceramic Coatings,“ Transactions of the Indian Ceramic Society, no. 74, Vol.. 2, pp. 97-103, 2015.

[42]   „Material Product Data Sheet Aluminum Oxide 40% Titanium Dioxide Powders, Oerlikon Metco,“ 2014. [Online]. Available:

https://www.oerlikon.com/ecomaXL/files/metco/oerlikon_DSMTS-0083.2_Al2O3_40TiO2.pdf&download=1. [Přístup získán 7 3 2018].

[43] „Parameter Optimization of Amalgamated Al2O3-40% TiO2 Atmospheric Plasma Spray Coating on SS304 Substrate Using TLBO Alrorithm," *Journal of Surface Engineered Materials and Advanced Technology,* Vol.. 6, pp. 6, p. 89-105, , 2016.

[44] N. Greeves, „TiO2 - Rutile," The university of Liverpool, 2008-2018. [Online]. Available: http://www.chemtube3d.com/solidstate/_rutile(final).htm. [Přístup získán 9 1 2018].

[45] Zavareh M. A., „Plasma thermal spray of ceramic oxide coating on carbon steel with enhanced wear and corrosion resistance for oil and gas applications," *Ceramics International, no.* 40, pp. 14267-14277, 2 June 2014.

[46] „Titanium Dioxide - Titania (TiO2), AZO MAterials, AZo Network Site," AZo Network Site, 2017. [Online]. Available at https://www.azom.com/properties.aspx?ArticleID=1179. [Přístup získán 27 12 2017].

[47] Yan D., et. al., „Corrosion Behavior in Boiling Dilute HCl Solution of Different Ceramic Coating Fabricated by Plasma Spraying," *Journal of Thermal Spray Technology, No.* 4, Vol.. Vol. 13, 2004.

[48] Fukumoto M., et. al., Effect of Connected Pores on the Corrosion Behaviour of Plasma Spraying Alumina Coating, Surf.Coat. Technol., 1989, Vol 39/40, pp. 711-720.

[49] UTU I.-D., et. al., „Sliding Wear Behavior of Remelted Al2O3-TiO2 Plasma Sprayed Coatings," *Trans Tech Publications, no.* 254, pp. 231-236`, 2016.

[50] Kamp L., et. al., „Caremic Coated Piston Rings for Internal Combustion Engines," v *WTC2005*, Washington, D. C., USA, 2005.

[51] Fauchais P. L., et. al., „Plasma-Sprayed Metals and coatings," v *Thermal spray fundamentals, From powder to part*, New York, Springer Science + Business Media New York, 2014, pp. 454-465.

[52] Abdullah M., et.al., „Structural and optical characterization of Cr2O3 nanostructures: Evaluation of its dielectric properties," 25 February 2014. [Online]. Available: https://aip.scitation.org/doi/full/10.1063/1.4867012. [Přístup získán 2018].

[53]   Dong S, et. al., „Microstructure and properties of Cr2O3 coating deposited by plasma spraying and dry-ice blasting,“ *Surface and Coatings Technology,* Vol.. 225, pp. 58-65, 11 December 2012.

[54]   Zamani P., Z. Valefi, „Microstructure, phase composition and mechanical properties of plasma sprayed Al2O3, Cr2O3 and Cr2O3-Al2O3 composite coatings,“ *Surface and Coatings Technology,* Vol.. 316, pp. 138-145, 14 March 2017.

[55]   „Chromic Oxide, Pubchem,“ National Center for Biotechnology Information, U. S. National Library, 30 6 2018`. [Online]. Available: https://pubchem.ncbi.nlm.nih.gov/compound/Chromium_III__oxide#section =Top. [Přístup získán 7 4 2018].

[56]   Smyth J. R., S. D. Jacobsen, „Comparative Crystal Chemistry of Dense Oxide Minerals,“ *Reviews in Mineralogy,* Vol.. 40, 2000.

[57]   Yang K., et. al., „Microstructure and mechanical properties of Al2O3– Cr2O3 composite coatings produced by atmospheric plasma spraying,“ *Surface and Coatings Technology,* Vol.. 206, pp. 1262-1371, 6 September 2011.

[58]   Islam M. M., et. al., „Stress Concentration in the Bulk Cr2O3: Effect of temperature and Point Defects,“ *Journal of chemistry,* Vol.. 2017, pp. 8, 2017.

[59]   Hones P., et. al., „Influence of deposition parameters on mechanical properties of sputter-deposited Cr2O3 thin films,“ *Journal of Materials Research, no.* 14, Vol.. 9, pp. 3623-3629, 1999.

[60]   Khangure S. S., et. al., „Sliding wear performance of plasma-sprayed Ni-20Cr Coating on AISI 309 SS Stell,“ v *Proceeding of the International Conference on Research and Innovations in Mechanical Engineering*, Ounjab, India: Springer, pp. 434-437, 2013,.

[61]   Khan M. Adam, et. al., „Sliding wear behavior of plasma sprayed coatings on nickel based superalloy,“ *Surface Engineering, no.* 33, Vol.. 1, pp. 35-39, 2017.

[62]   Cui S., et. al., „Tribological Behavior of Plasma-Sprayed Al2O3- 20 wt.%TiO2 Coating,“ *Journal of Materials Engineering and Performance, no.* 26, Vol.. 5, pp. 2086-2094, 10 April 2017.

[63]   Barati N., et. al., "Al2O3-ZrO2 nanostructured coatings using DC plasma electrolytic oxidation to improve tribological properties of Al substrates," *Applied Surface Science,* no. 356, pp. 927-934, 30 November 2015.

[64] Ekتröm M., et. al., „Evaluation of internal thermal barrier coatings for exhaust manifolds,“ *Surface and Coatings Technology, no.* 272, pp. 198-212, 2015.

[65] Nusair Khan A., Lu J., „Manipulation of air plasma spraying parameters for the production of ceramic coatings,“ *Journal of Materials Processing Technology, no.* 209, pp. 2508-2514, 2009.

[66] Newby N., „Nikon Introduces SMZ1500 Stereo Microscope with Highest Optical Performance, Largest Zoom Range Available,“ Nikon Instruments, 28 July 2000. [Online].Available at: https://www.nikoninstruments.com/cz_CZ/About-Nikon/News-Room/US-News/Nikon-Introduces-SMZ1500-Stereo-Microscope-with-Highest-Optical-Performance-Largest-Zoom-Range-Available. [Přístup získán 7 1 2018].

[67] Klyatskina E., et. al., „A study of the influence of TiO2 addition in Al2O3 coatings sprayed bysuspension plasma spray,“ *Surface and Coatings Technology, no.* 278, Vol.. 25-29, 2015.

[68] Anderson H., „Scanning electron microscope,“ Microscopemaster, 2010-2018. [Online]. Available: https://www.microscopemaster.com/scanning-electron-microscope.html. [Přístup získán 7 7 2018].

[69] Jurči P., Nástrojové oceli ledeburitického typu, Praha: České vysoké učení technické v Praze, 2009, .

[70] Standards A., „G 99-95a, Standard Test Method for Wear Testing with a Pin=on=Disk Apparatus,“ 100 Barr Harbor Drive, PO Box C700, West Conshohocken, 2000, pp. 1-6.

[71] Bull R. D., „Characterization of hard coatings. In: Bunshah RF,,“ v *Handbook of hard coatings*, Norwich, N.Y, Park Ridge: Noyes publications, William Andrew Pub, 2001, pp. 181-228.

[72] „International organisation for standardization,“ 06 2015. [Online]. Available: Available at https://www.iso.org/standard/51692.html. [Přístup získán 3 6 2018].

[73] „Salt Spray, Salt Fog and Corrosion Testing, Element, Element Materials Technology,“ Element Materials Technology, 2017. [Online]. Available: https://www.element.com/product-qualification-testing-services/salt-spray-salt-fog-corrosion-testing. [Přístup získán 5 5 2018].

[74] „T91/P91 Steel, MTS Ferrous and Nonferrous Alloy Piping,“ HeBei Metals Industrial Limited., 2016. [Online]. Available at:

http://www.metalspiping.com/t91-p91-steel.html. [Přístup získán 12 září 2017].

[75] Andreson H., „Nikon Stereo Microscopes,“ MicroscopeMaster, 2010-2018. [Online]. Available: https://www.microscopemaster.com/nikon-stereo-microscopes.html. [Přístup získán 6 July 2018].

[76] Q.-S. Metal, „Q235A Included in 3 standards (China),“ Quantor Ltd. , 1991-2017. [Online]. Available: http://metaldata.info/reports/Q235A.pdf. [Přístup získán 23 9 2017].

[77] Chatha S. S., et. al., High temperature hot corrosion behavior of NiCr and Cr3C2–NiCr coatings on T91 boiler steel in an aggressive environment at 750 °C, Punjab: Surface and Coatings Technology, 2012, 206.

[78] Liu Z., et. al., „Improving corrosion and wear performance of HVOF-sprayed Inconel 625 and WC-Inconel 625 coatings by high power diode laser treatments,“ *Surface and Coatings Technology, ScienceDirect,* Vol.. 201, no. 201, p. 7149-7158, 2007.

[79] Miha L. L., et. al., „In vitro Study of the Effectiveness to Fractures of the Aesthetic Fixed Restorations Achieved from Zirconium and Alumina,“ *Revista de chimie,* Vol.. 6, no. 65, 6, p. 725-729, June 2014.

[80] Robert V. Hillery, Bartlet N., Coatings for High temperature Structural Materials: Ternds and opportunities, Washington D.C.: National Academy press, 1996.

[81] Sathyaseelan B., et. al., „Phase Transition Behavior of Nanocrystalline Al2O3 Powders,“ *Soft Nanoscience Letters,* pp. 69-74, October 2013.

[82] Van de Voorde M. H., G. W. Meetham, Materials for High Temperature Engineering applications, IX editor, Verlag Berlin Heidelberg: Springer, 2000, Vol. 9, pp. 19-20.

[83] Zhang T., et. al., „Fromation mechanism of the lubrication film on the plasma sprayed NiCoCrAlY-Cr2O3-AgMo coating at high temperatures,“ *Surface and Coating Technology, Elsevier B. V.,* Vol. 319, pp. 47-54, 2017.

[84] Handbook of thermal spray technology. Materials Park, OH: ASM International, 2004. s. 47-73, 171-172, 180-182, 225-226, 263. ISBN 0871707950.

LIST OF PICTURES

LIST OF TABLES

LIST OF ATTACHMENTS

ATTACHMENTS

Name	$R_{p0,2}$ [MPa] at the temperature °C									
	148.8	204.4	260	315.5	371.1	426.6	482.2	537.7	593.3	648.8
P91 ASME B31.3 [a]	195.1	194.4	193.7	190.9	184.1	171.7	153.7	124.1	71	29.6

[a] ASME 31.3 – Process Piping

Attachment 1: Minimum values of the yield strength ($R_{p0,2}$) at elevated temperatures of P91 [11]

Name	$R_{p0,2}$ [MPa] at the temperature °C											
	-28.8 to 37.7	93.3	148.8	204.4	260	315.5	371.1	426.6	482.2	537.7	593.3	648.8
P91/T91 ASME B31.1 [b]	167.5	167.5	167.5	166.9	166.1	163.4	157.9	146.9	131.7	112.4	66.2	29.6

[b] ASME 31.1 – Power Piping

Attachment 2: Minimum values of the yield strength ($R_{p0,2}$) at elevated temperatures of P91/T91 [11]

Name	$R_{p0,2}$ [MPa] at the temperature °C in MPa										
	100	150	200	250	300	350	400	450	500	550	600
X10CrMoVNb9-1	410	395	380	370	360	350	340	320	300	270	215

Attachment 3: Minimum values of the proof strength $R_{p0,2}$ at elevated temperatures of X10CrMoVNb9-1 [10]

Temperature [°C]	Modulus of Elasticity [GPa]	Thermal Conductivity [W/mK]	Linear Expansivity [10^{-6}/°C]	Specific Heat [J/kg·K]	Density [kg/m^3]
20	218	26	0.0	440	7770
50	216	26	10.6	460	
100	213	27	10.9	480	
150	210	27	11.1	490	
200	207	28	11.3	510	
250	203	28	11.5	530	
300	199	28	11.7	550	
350	195	29	11.8	570	
400	190	29	12.1	630	
450	186	29	12.1	630	
500	181	30	12.3	660	
550	175	30	12.4	710	
600	168	30	12.6	710	
650	162	30	12.7	860	

Attachment 4: Physical properties of P91/T91 at different temperatures [74]

Parameter	Value
Plasma-forming gases and flow rates	Ar, 40 slpm; H$_2$, 10slpm
Carrier gas and flow rate	Ar, 3-4 slpm
Torch power	32-33 kW
Cooling	Air, 0-50 psi
Spray distance	6.5 cm
Coating thickness	70-300 μm

Attachment 5: Atmospheric plasma spray process parameters used to deposit forsterite coatings [23]
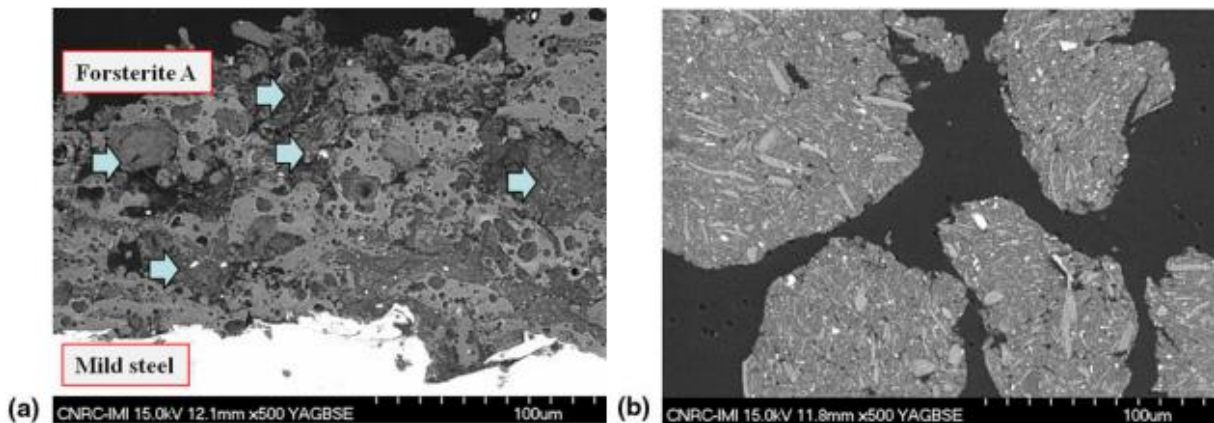
Attachment 6: (a) SEM micrograph of the type-A forsterite coating produced with a 150 μm powder granulometry. (b) Cross-section SEM micrograph of the forsterite particles present in the powder A [23]
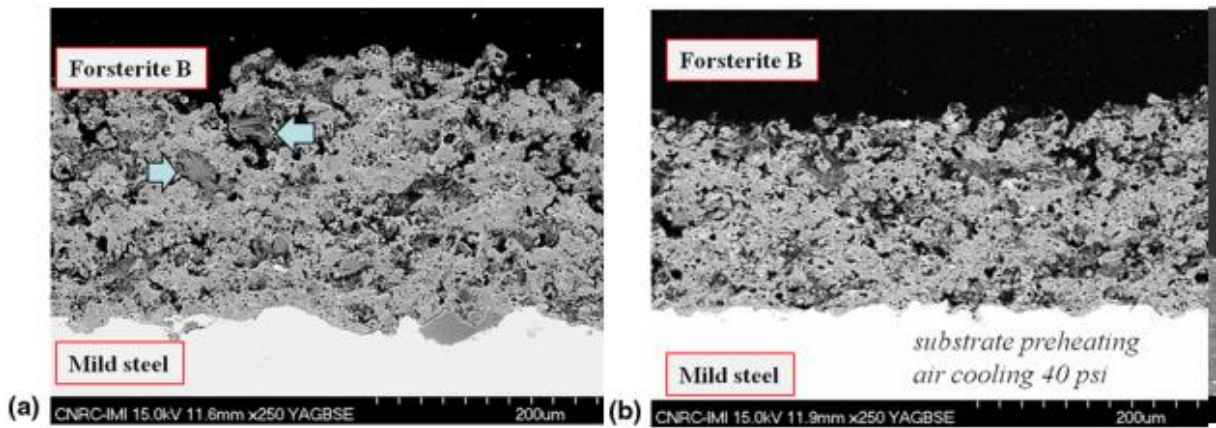
Attachment 7: SEM micrographs of the cross-section of type-B forsterite coatings produced using the powder B for two spray conditions: (a) no substrate preheating and (b) with substrate preheating [23]
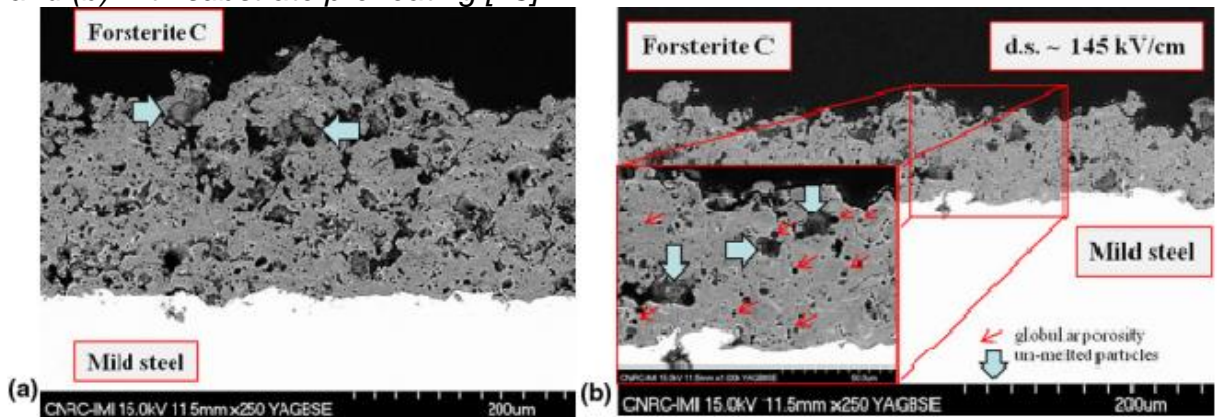
Attachment 8: SEM micrographs of the cross-section of type-C forsterite coating produced using the powder C [23]
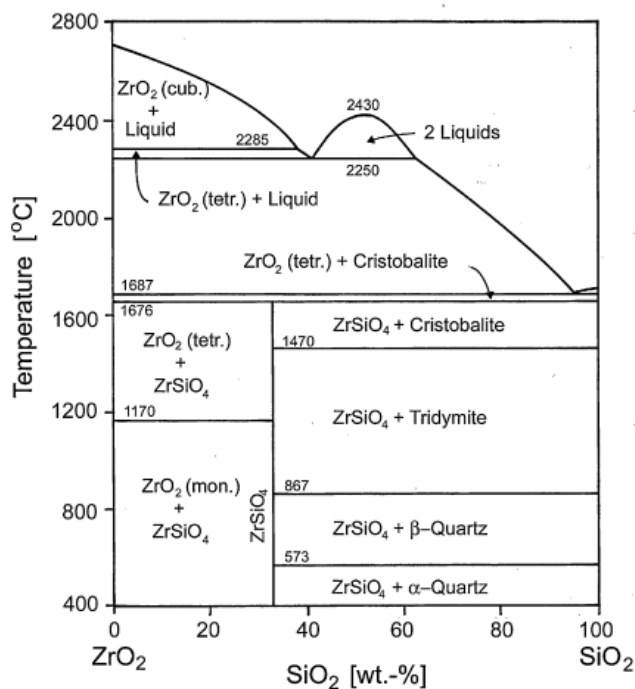
Attachment 9: Phase diagram of ZrO_2-SiO_2 [26]
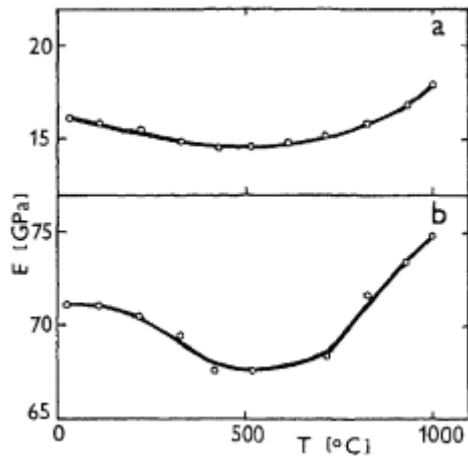
Attachment 10: Young's modulus of plasma-sprayed ZrSiO₄ as function of temperature: curve (a) as sprayed; curve (b) annealed for 3 h. at 1300 °C. [30]
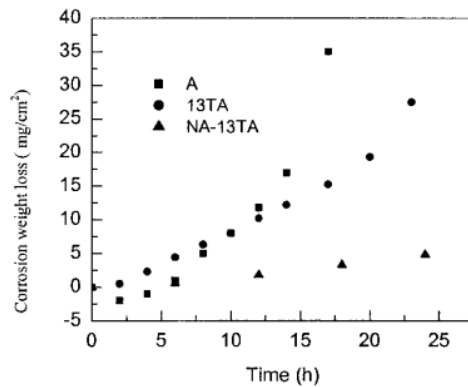
Attachment 11: Corrosion weight loss of the samples with three ceramic coatings in a boiling 5% HCl solution for 24 h. [47]
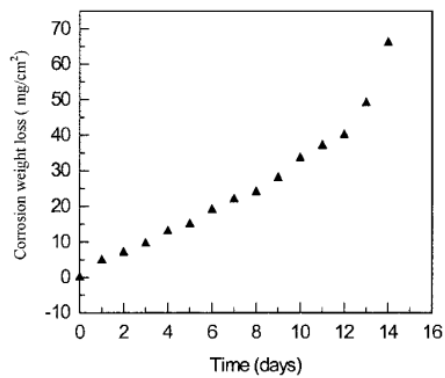
Attachment 12: Corrosion weight loss of samples with the NA-13TA gradient composite ceramic coatings in the boiling 5% HCl solution for 14 days. [47]
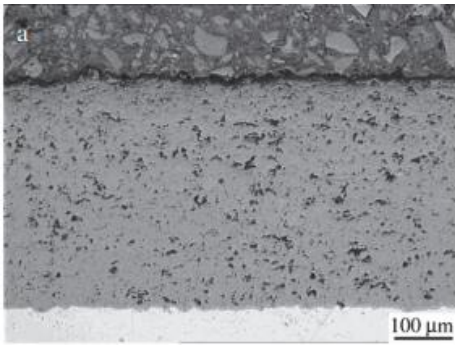
Attachment 13: OM micrograph of Cr_2O_3 coating plasma sprayed *[53]*
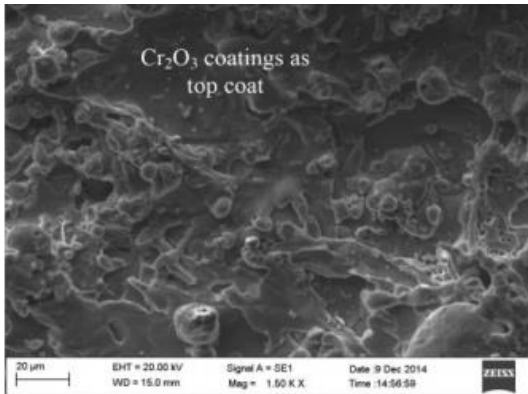
Attachment 14: The surface morphology of NiCr-Cr_2O_3 coating before the wear [61]
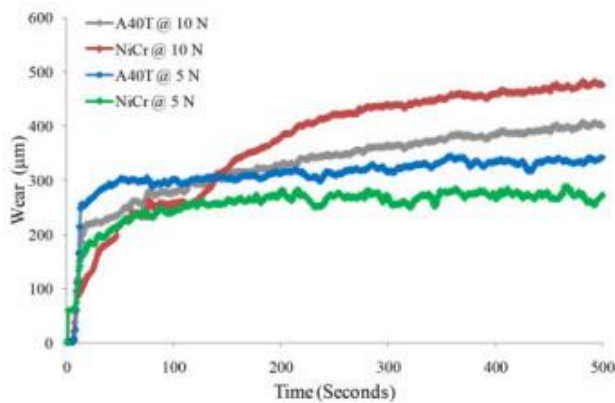
Attachment 15: The progress of sliding wear with respect to applied load at constant velocity (1 m/s) [61]
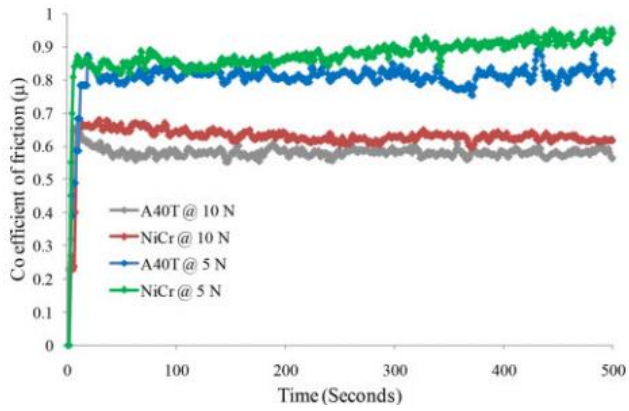
Attachment 16: The coefficient of friction with respect to applied load for A40T and NiCr-Cr₂O₃ coating [61]
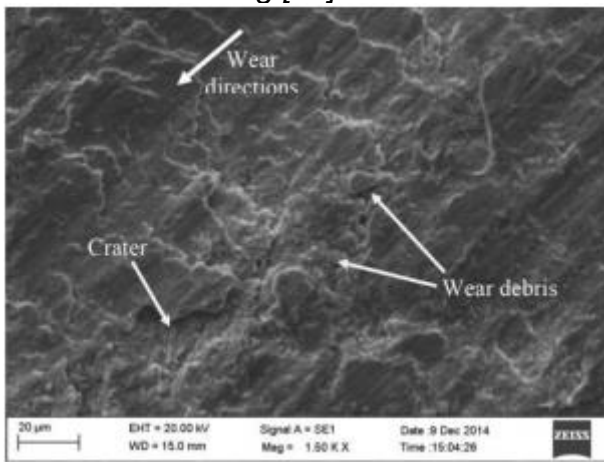
Attachment 17: Wear morphology of NiCr-Cr₂O₃ coated disc under 10N load [61]
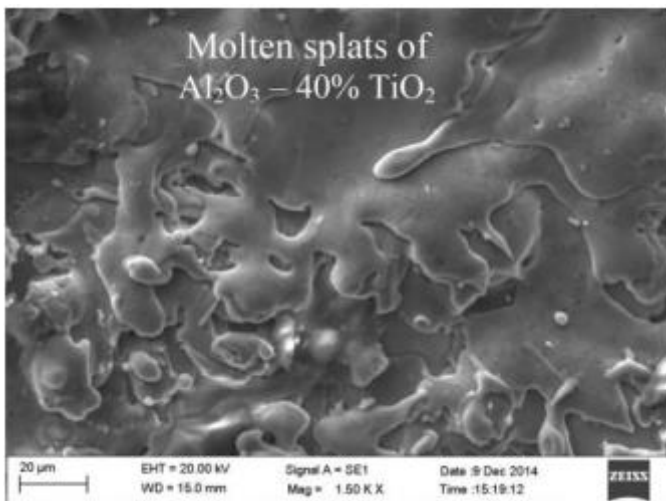
Attachment 18: Surface morphology of A40T coating before sliding wear [61]
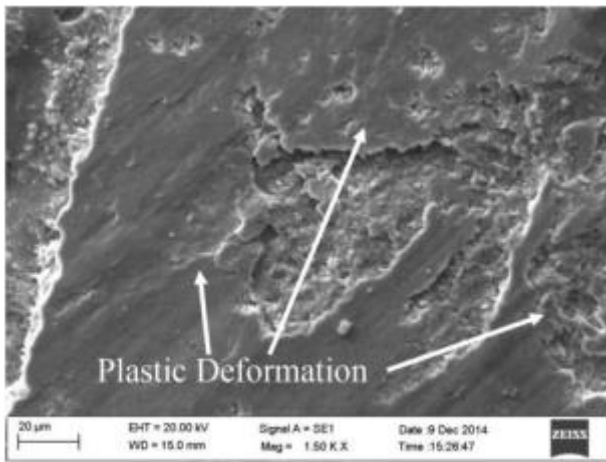
Attachment 19: Wear and surface morphology of A40T coating after sliding under 10 N. [61]
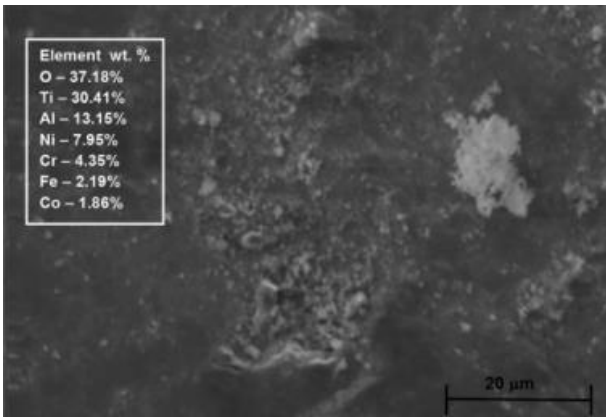
Attachment 20: Analysis (EDS) of A40T coating after sliding wear of 10 N. [61]

Powders	Voltage [V]	Current [A]	Spraying distance [mm]	Argon flow rate [slpm]	Hydrogen flow rate [slpm]	Mass flow rate [g/min]
Ni-Al	42	430	100	0.8	0.26	70
Al$_2$O$_3$-20 wt.%TiO$_2$	52	560	100	0.8	0.26	80

Attachment 21: Parameters of plasma spraying [62]

Attachment 22: Stereo microscope SMZ 1500 [75]
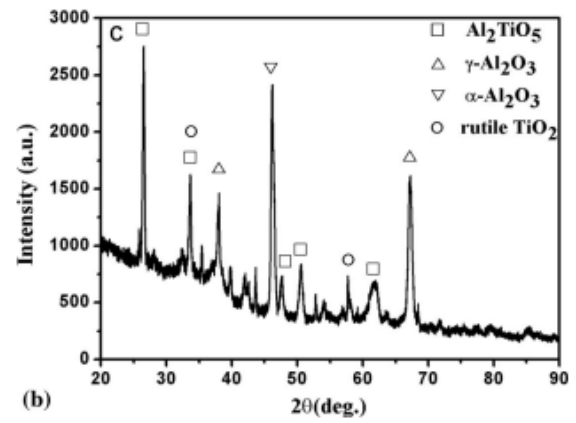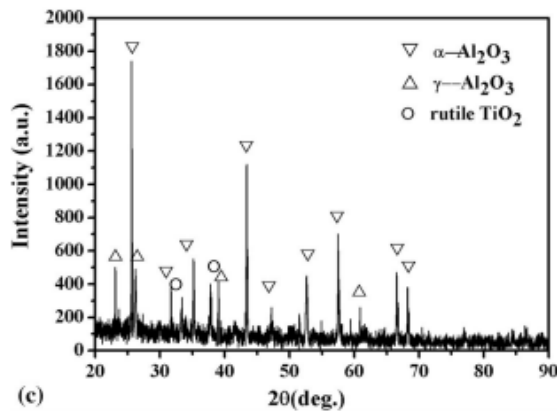
Attachment 23: The XRD spektra of a) Al_2O_3-20 wt.% TiO_2 powder and b) Al_2O_3-20 wt.%TiO_2 coating [62]
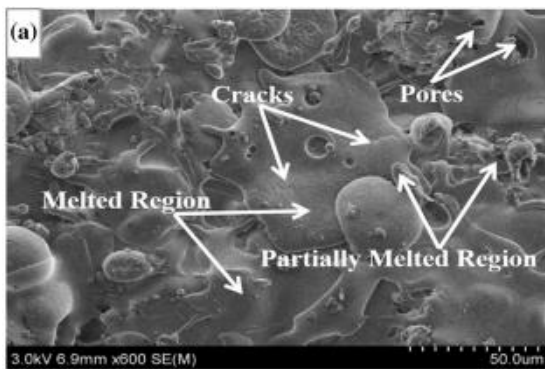
Attachment 24: SEM morphology of Al_2O_3-20 wt.% TiO_2 [62]

Sample	Load [N]	Wear volume V[mm³]	Width of wear tracks [µm]	Specific wear rate K [10⁻⁶ mm³/Nm]
Grade D steel	5	1.74	1591.2	413.1
	10	2.77	1852.6	328.8
	15	3.58	2009.8	283.3
Al_2O_3-20 wt.% TiO_2	5	0.014	325.6	3.3
	10	0.040	457.9	4.8
	15	0.057	514.1	4.5

Attachment 25: Volume loss and specific wear rate of the substrate and the Al_2O_3-20 wt.% TiO_2 coating [62]
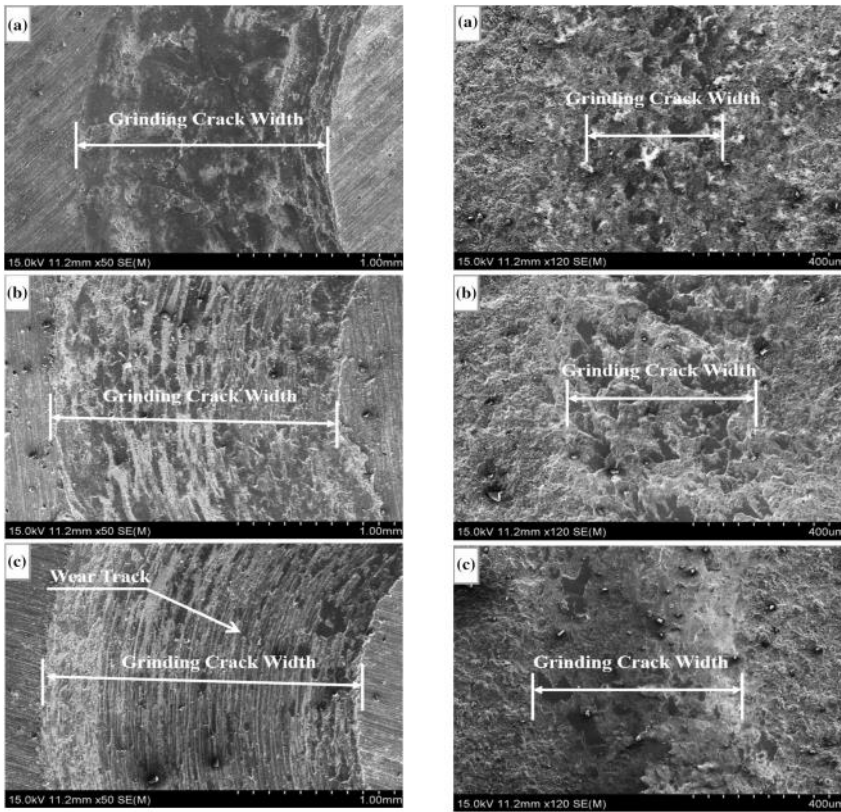
Attachment 26: SEM image of worn surface of the Grade D steel (on the left) and the the Al_2O_3-20 wt.% TiO_2 coating (on the right) for the load of (a) 5 N, (b) 10 N and (c) 15 N [62]

Top coating:	Thickness [μm]
8YSZ	381±13
Nano-8YSZ	261±23
$La_2Zr_2O_7$	294±7
Mullite ($3Al_2O_3 \cdot 2SiO_2$)	440±21
Forsterite ($2MgO \cdot SiO_2$)	301±9

Attachment 27: Thickness of different thermal barrier coatings applied with plasma [64]
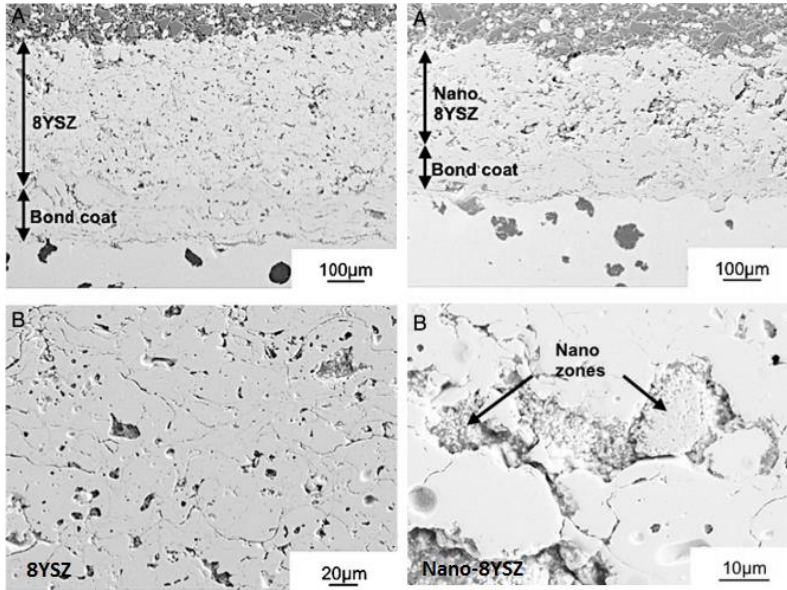
Attachment 28: SEM images of 8YSZ on the left and Nano-8YSZ on the right of (A) microstructure of coating system and (B) microstructure of coatings [64]
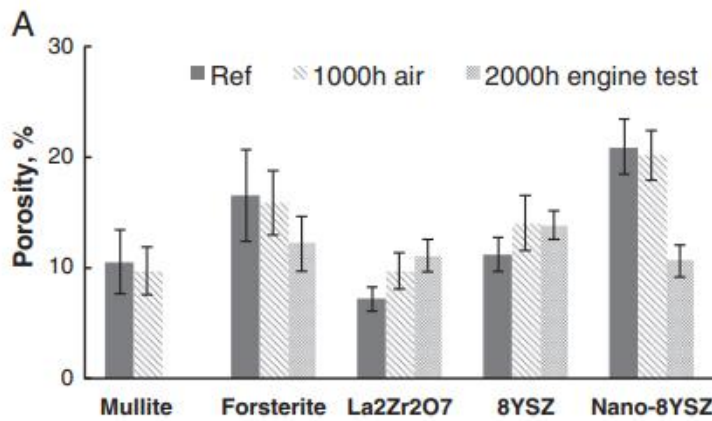
Attachment 29: Porosity for plasma-sprayed samples as-coated and samples thermally cycled in air for 1000 h. and diesel exhaust gas for 2000 h. [64]
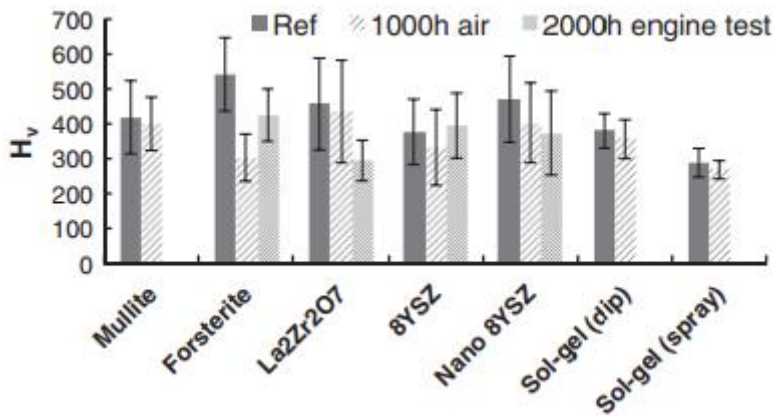
Attachment 30: Vickers hardness (HV) for plasma-sprayed samples in as-sprayed condition and samples thermally cycled in air for 1000 h. and diesel exhaust gas for 2000 h. [64]
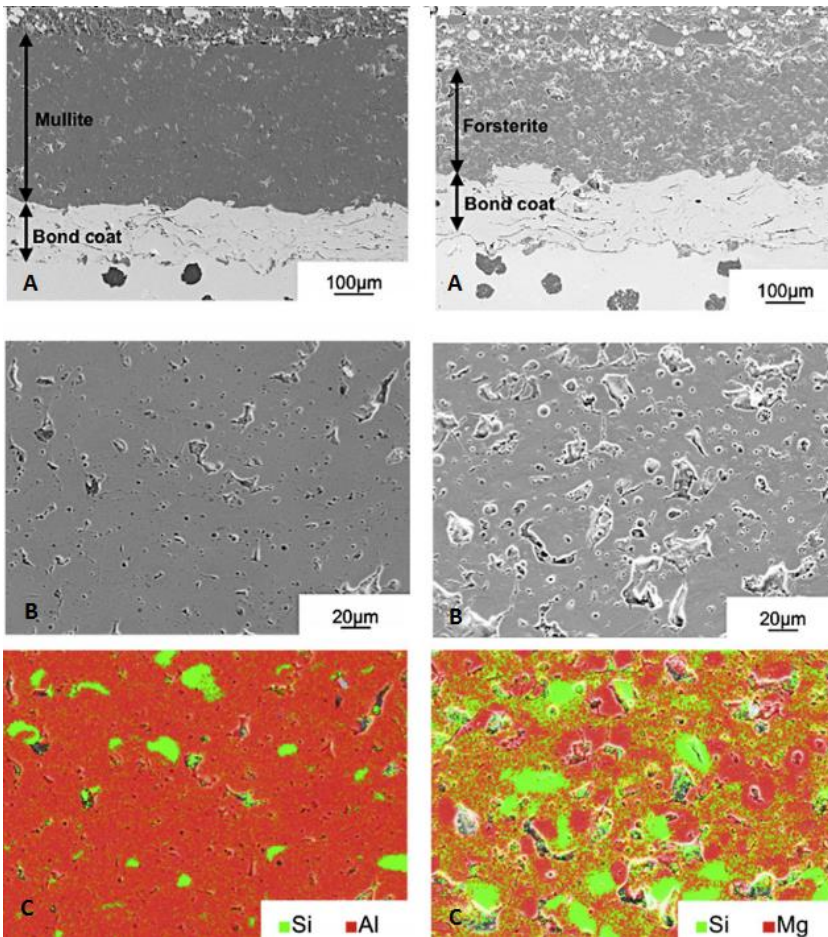
Attachment 31: SEM pictures of microstructure (A, B) and EDX quant map (C) of Mullite (on the left) and Forsterite (on the right) [64]
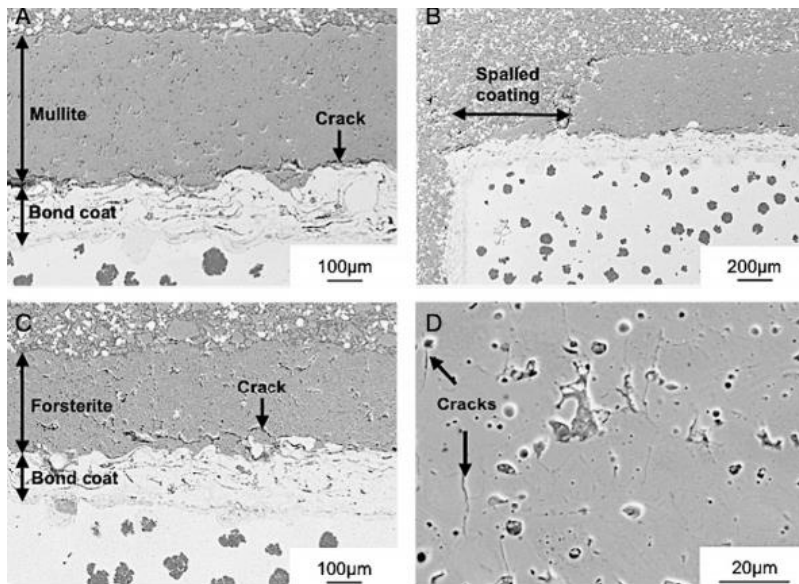
Attachment 32: SEM images of the coating microstructure after thermal cycling in air for 1000 h showing (A) mullite system, (B) spallation of mullite, (C) forsterite system, (D) cracks in forsterite [64]
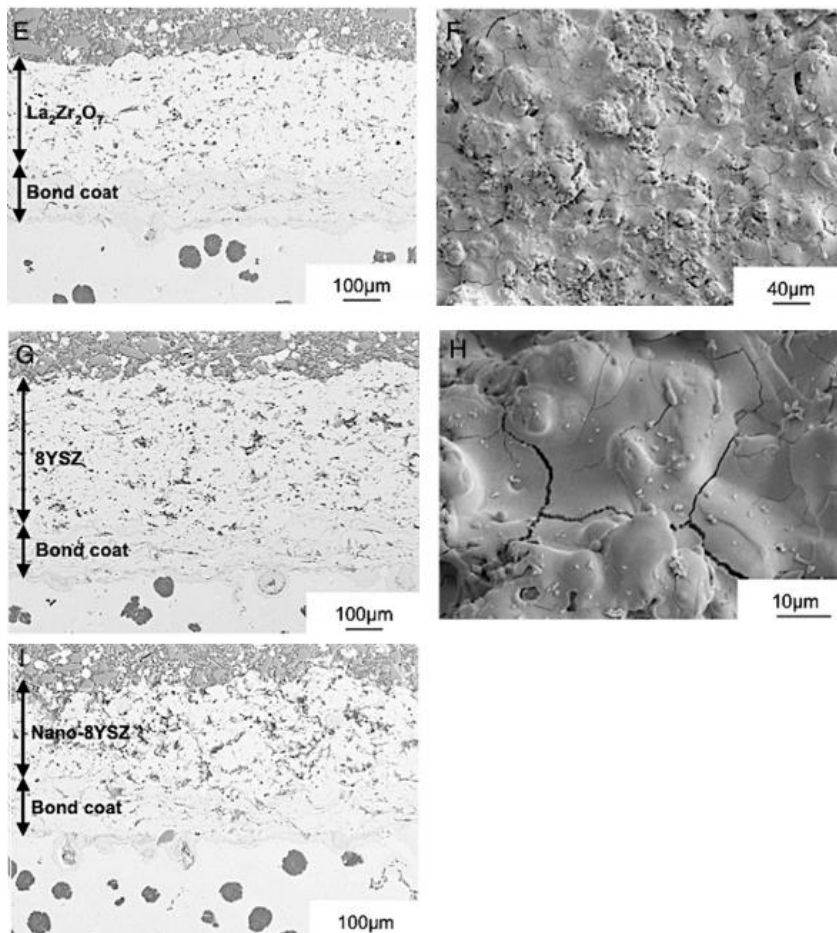
Attachment 33: SEM images of the coating microstructure after thermal cycling in air for 1000 h showing (E) La2Zr2O7 system, (F) La2Zr2O7 (topographical view), (G) 8YSZ system, (H) 8YSZ (topographical view), and (I) nano-8YSZ system [64]

Thickness [μm]	Spraying distance [mm]	Current [A]	Primary gas flow rate [SLPM]	Number of cycles to failure		
				Water quenched	Pressurized air quenched	Long cycling
377± 14	80	600	32	90	800	53
532± 12	80	600	32	35	755	26
688± 9	80	600	32	10	260	4
562± 13	80	600	32	26	174	8
371± 10	125	550	32	59	228	6
289± 10	125	650	32	65	510	16
286± 4	125	600	46	70	880	46
314± 10	125	600	39	46	358	8
355± 14	125	600	32	40	176	5

Attachment 34: Parameters of spraying YSZ coatings and their failure life [65]

Number of measurement	Al_2O_3	AT40	Olivine	$ZrSiO_4$	$ZrSiO_4$ - Y_2O_3	$NiCr$-Cr_2O_3
1	41,08	46,23	46	49,8	49,23	58,5
2	41,85	47,33	47,03	52,55	49,8	60,13
3	45,8	49,85	49,88	57,6	51,75	61,15
4	48,78	50,08	51,63	57,93	59,5	61,9
5	49,25	51,53	51,65	65,27	61,03	62,95
6	49,28	51,88	52,13	65,45	61,45	63,25
7	53,57	52,75	61,9	67,38	63,58	63,48
8	57,43	53,85	63,68	70,98	64,13	64,43
9	59,68	54,2	73,28	71,45	67,23	64,95
10	60,3	54,75	73,95	71,53	67,73	65,63
11	60,58	55,65	74,6	75,6	67,85	66,2
12	60,63	57,28	74,6	75,95	71,1	66,5
13	62,95	60,43	75,53	76,08	71,48	68,88
14	64,77	63,33	76,2	77,03	72,38	69,43
15	70	65,15	78,43	79,6	75,98	69,5
HRA (Mean value)	55,1	54,3	63,4	67,6	63,6	64,5
Standard deviation	8,702089	5,445862	12,41002	9,362532	8,292287179	3,326547

*Attachment 35: Hardness HRA of tested coatings as-sprayed*

Number of measurement	Al_2O_3	AT40	Olivine	$ZrSiO_4$	$ZrSiO_4$-Y_2O_3	$NiCr$-Cr_2O_3
1	39,58	36,73	44,35	32,78	38,28	63,15
2	44,55	60,4	47,03	33,33	39,93	63,55
3	44,75	61,45	56,55	37,65	42,78	65,55
4	49,7	62,03	64,13	40,45	46,93	65,68
5	51,25	62,15	64,73	47,83	48,8	66,45
6	51,33	62,28	65,35	52,38	49,68	67,3

7	53,95	65,83	68,8	58,98	49,9	69,35
8	55,19	66	71,2	59,08	53,33	69,75
9	57	68,88	75,93	64,58	56,68	69,8
10	57,13	69,03	76,63	65,7	56,88	70,8
11	57,18	70,68	77,78	67,15	57,85	71,5
12	58,18	74,05	77,85	67,78	58,68	72,7
13	58,48	75	81,7	69,55	66,33	73,25
14	59,4	77,85	82,48	70,93	71,75	74,15
15	74,65	77,95	84,33	77,1	75,98	74,48
HRA (Mean value)	54,2	66,0	69,3	56,4	54,3	69,2
Standard deviation	8,190051	10,07701	12,37549	14,66411	10,97197352	3,731711

Attachment 36: Hardness HRA of tested coatings after heat treatment at 650 °C for 10 hours

Temperature (°C)	Start μ	Stabilized μ
23 °C	0.15	0.37
200 °C	0.14	0.40
400 °C	0.77	0.79
600 °C	0.73	0.73
750 °C	0.74	0.75

Attachment 37: Coefficient of friction (μ) for Al_2O_3 coating at different temperatures

A)

B)

C)

D)
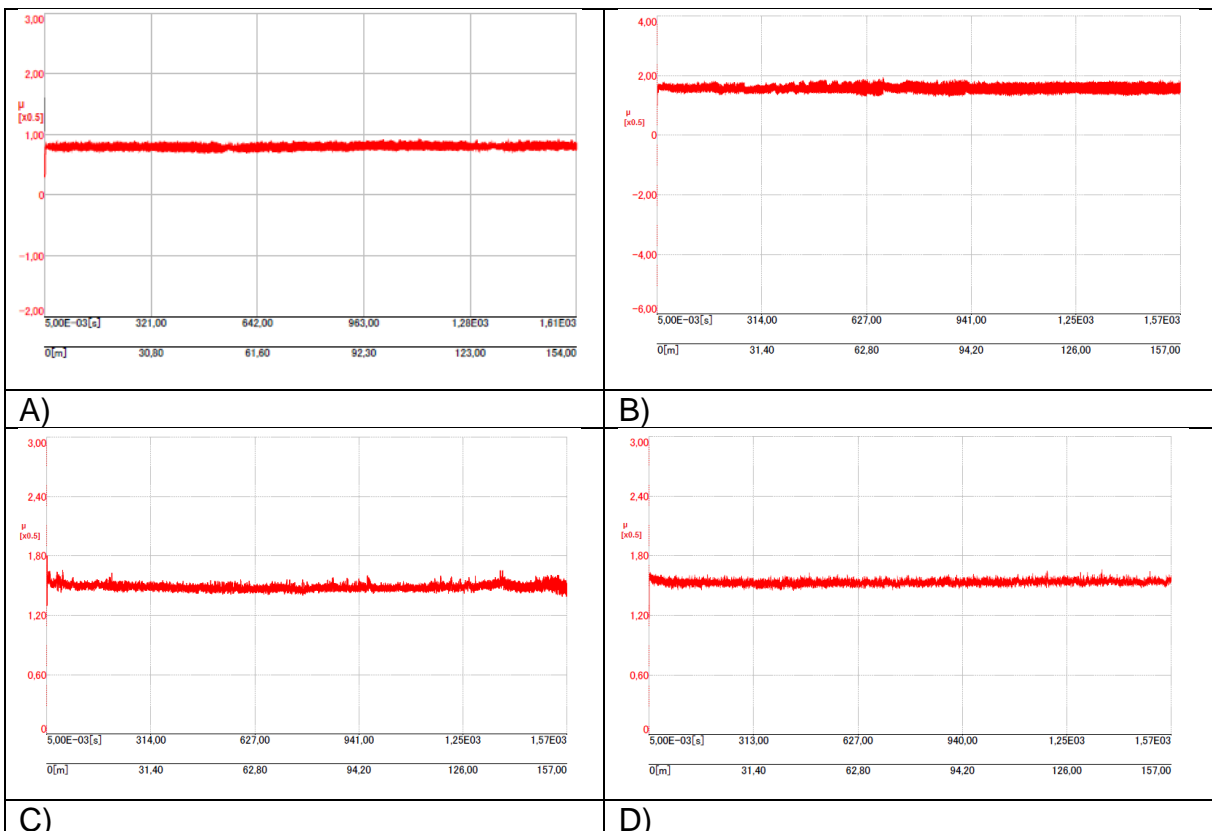
Attachment 38: Friction coefficient of Al_2O_3 coating at A) 200 °C, B) 400 °C, C) 600 and D) 750 °C

Al₂O₃			
Temperature	Disk volume loss [mm³]	Specific wear rate K of the coating [10^{-3} mm³/Nm]	Pin volume loss [$\times 10^{-3}$ mm³]
23 °C	1.46	1.86	36.16
200 °C	18.10	23.05	301.02
400 °C	26.84	34.17	223.17
600 °C	28.96	36.87	171.27
750 °C	22.16	28.22	211.48

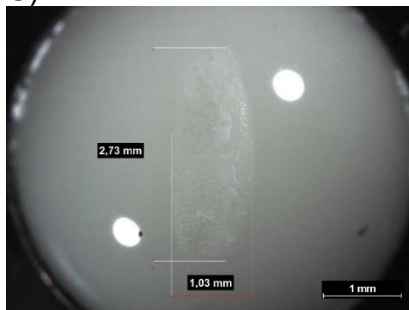*Attachment 39: Coating volume loss, pin volume loss and wear rate of Al₂O₃ coating at different temperatures*
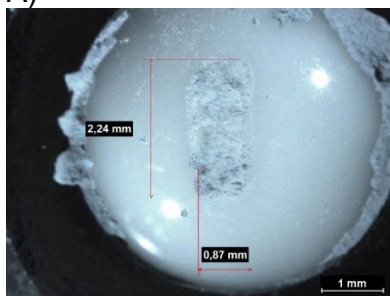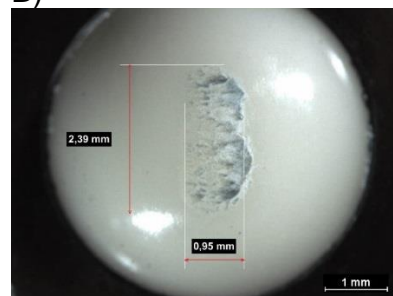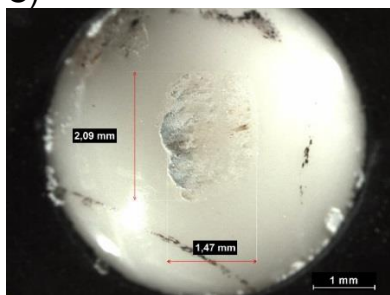
A)
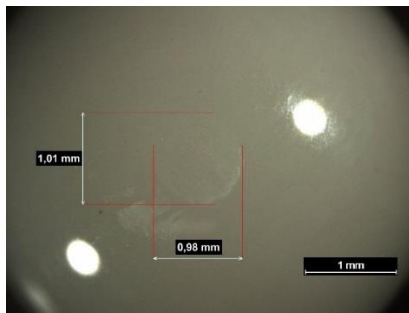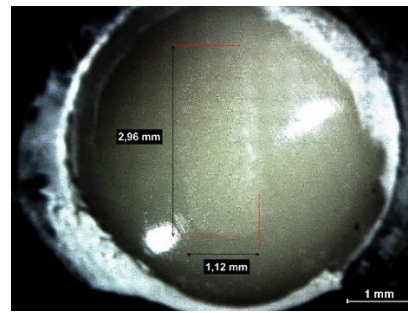
B)
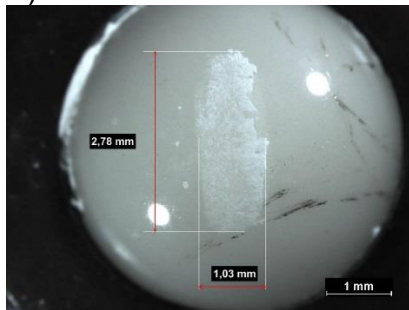
C)
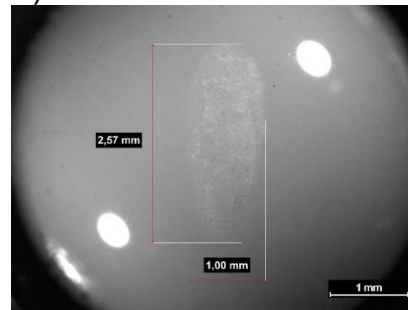
D)

E)

Attachment 40: Wear of the pin from coating Al₂O₃ at A) 23 °C, B) 200 °C, C) 400 °C, D) 600 °C and E) 750 °C

Temperature (°C)	Start μ	Stabilized μ
23 °C	0.81	0.83
200 °C	0.71	0.89
400 °C	0.69	0.87
600 °C	0.68	0.82
750 °C	0.57	0.81

Attachment 41: Coefficient of friction (μ) for AT40 coating at different temperatures

A)

B)

C)

D)

E)
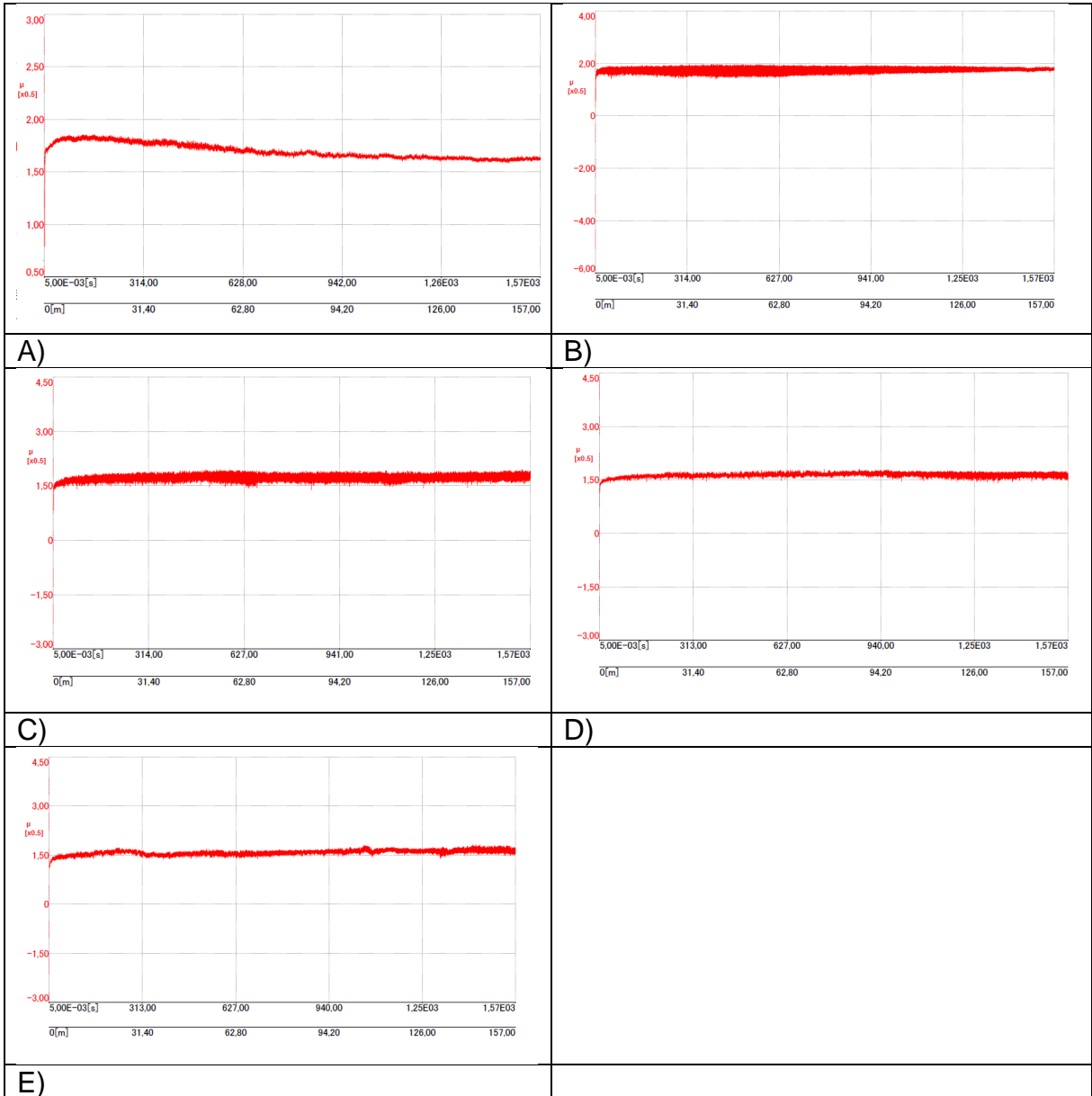
Attachment 42: Friction coefficient for AT40 coating at A) 23 °C, B) 200 °C and C) 400 °C, D) 600 and E) 750 °C

AT40			
Temperature	Coating volume loss [mm^3]	Specific wear rate K of the coating [10^{-3} mm^3/Nm]	Pin volume loss [x10^{-3} mm^3]
23 °C	1.63	2.07	26.52
200 °C	10.66	13.57	159.88
400 °C	10.36	13.18	97.90
600 °C	10.81	13.77	130.70
750 °C	11.44	14.57	169.33

Attachment 43: Coating volume loss, pin volume loss and wear rate of AT40 coating at different temperatures

A)
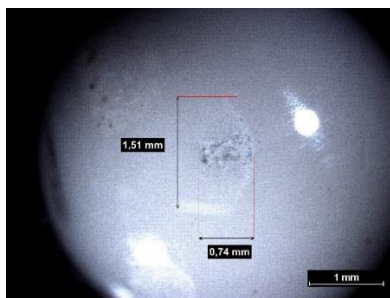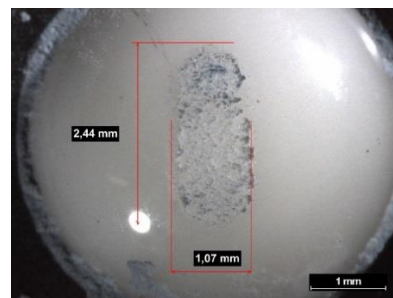
B)

C)

D)

E)

Attachment 44: Wear of the pin from coating AT40 at A) 23 °C, B) 200 °C, C) 400 °C, D) 600 °C and E) 750 °C

Temperature (°C)	Start μ	Stabilized μ
23 °C	0.17	0.80
200 °C	0.61	0.87
400 °C	0.67	0.93
600 °C	0.55	0.69
750 °C	0.51	0.58

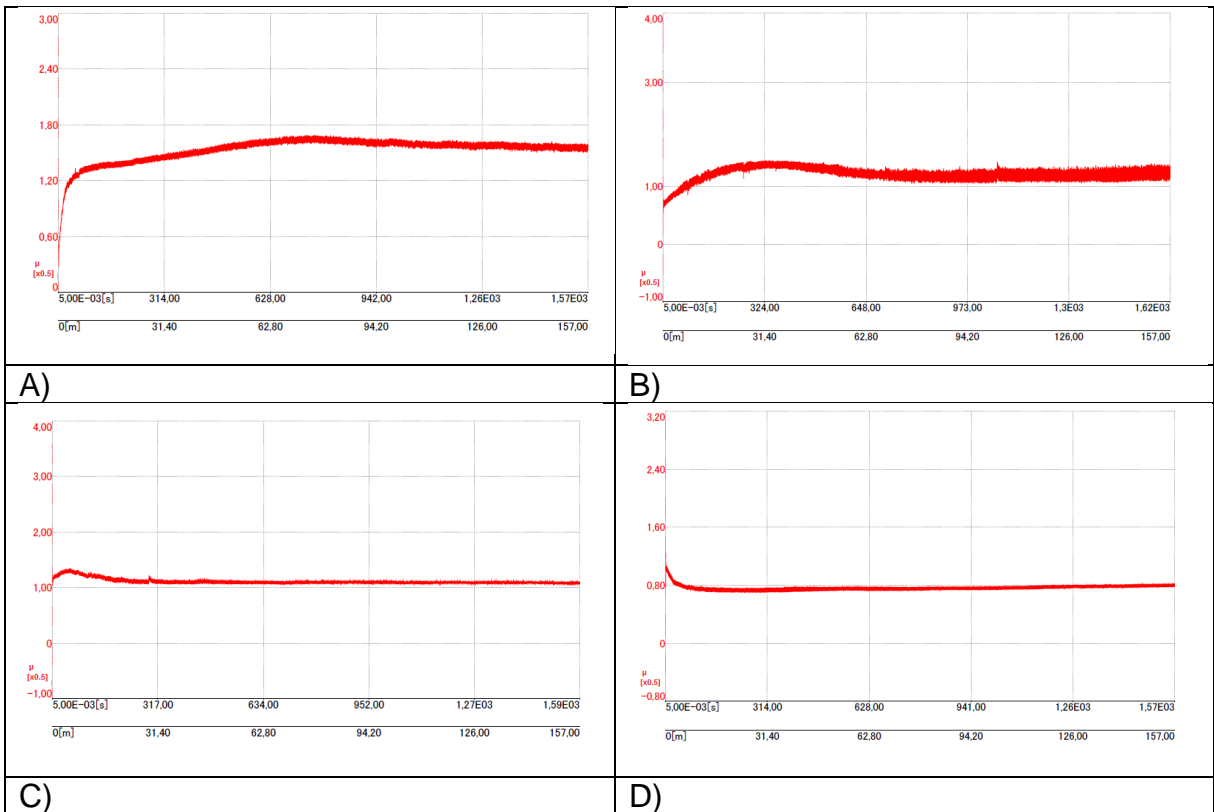*Attachment 45: Coefficient of friction (μ) for olivine coating at different temperatures*
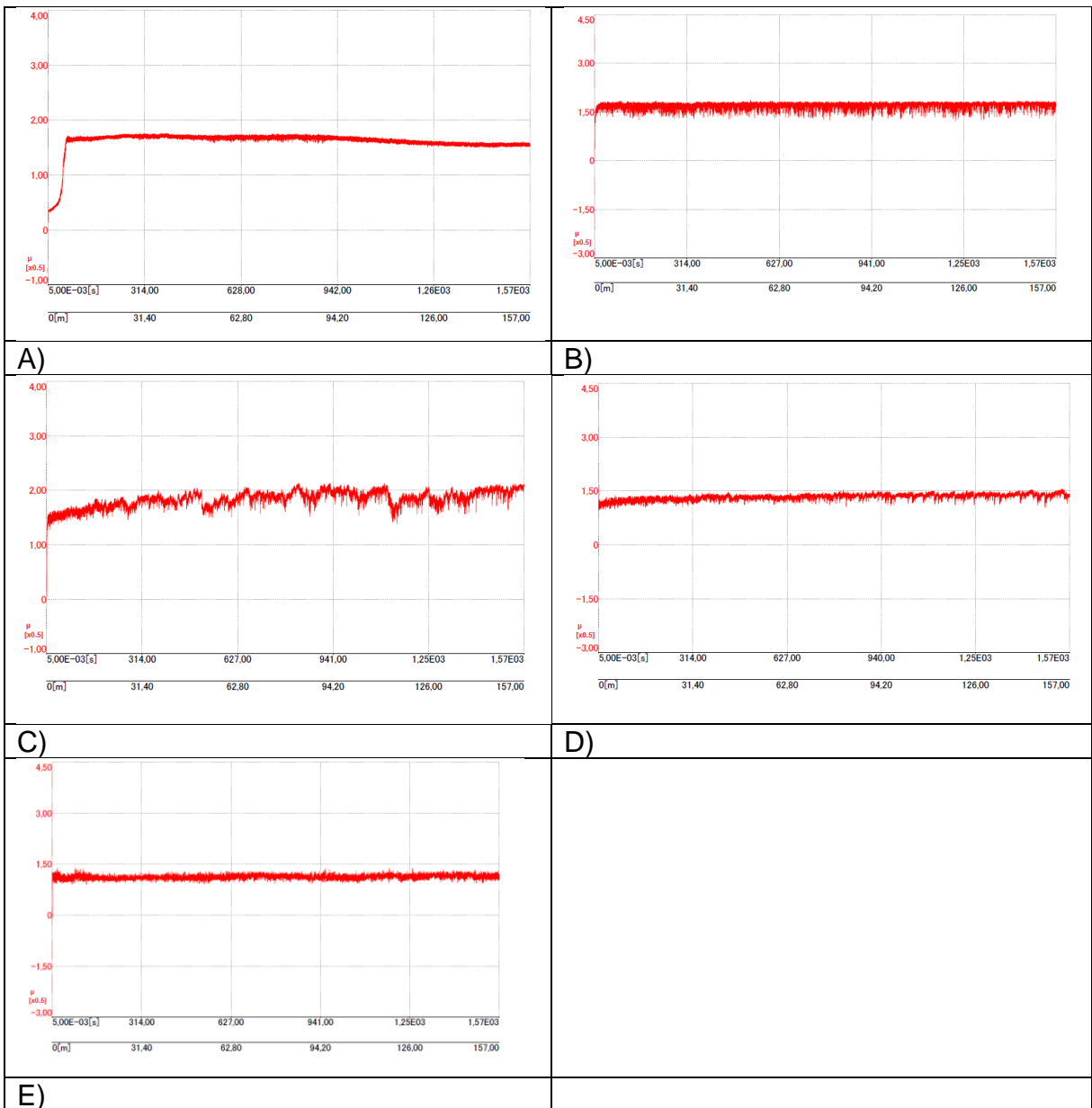
Attachment 46: Friction coefficient of Olivine coating at A) 23 °C, B) 200 °C, C) 400, D) 600 °C and E) 750 °C

Olivine			
Temperature	Wear volume of the coating [mm^3]	Specific wear rate of the coating K [10^{-3} mm^3/Nm]	Wear volume of the pin [x10^{-3} mm^3]
23 °C	2.14	2.72	40.54
200 °C	16.74	21.32	615.29
400 °C	9	11.46	232.87
600 °C	3.26	4.16	91.68
750 °C	5.38	6.84	126

Attachment 47: Coating volume loss, pin volume loss and wear rate of olivine coating at different temperatures

Temperature (°C)	Start μ	Stabilized μ
23 °C	0.17	0.80
200 °C	0.31	0.63
400 °C	0.56	0.54
600 °C	0.52	0.38
750 °C	0.54	0.35

Attachment 48: Coefficient of friction (μ) for NiCr-Ni$_2$O$_3$ coating at different temperatures

Attachment 49: Friction coefficient of NiCr-Cr$_2$O$_3$ coating at A) 23 °C, B) 200 °C, C) 400 °C, D) 600 °C

NiCr-Ni$_2$O$_3$			
Temperature	Coating volume loss [mm^3]	Specific wear rate K of the coating [10^{-3} mm^3/Nm]	Pin volume loss [x 10^{-3} mm^3]
23 °C	1.31	1.67	21.28
200 °C	0.65	0.83	26.52
400 °C	0.86	1.09	41.86
600 °C	0.51	0.65	30.53
750 °C	0.20	0.26	28.98

Attachment 50: Coating volume loss, pin volume loss and wear rate of NiCr-Ni$_2$O$_3$ coating at different temperatures

A)   B)   C)

D)   E)
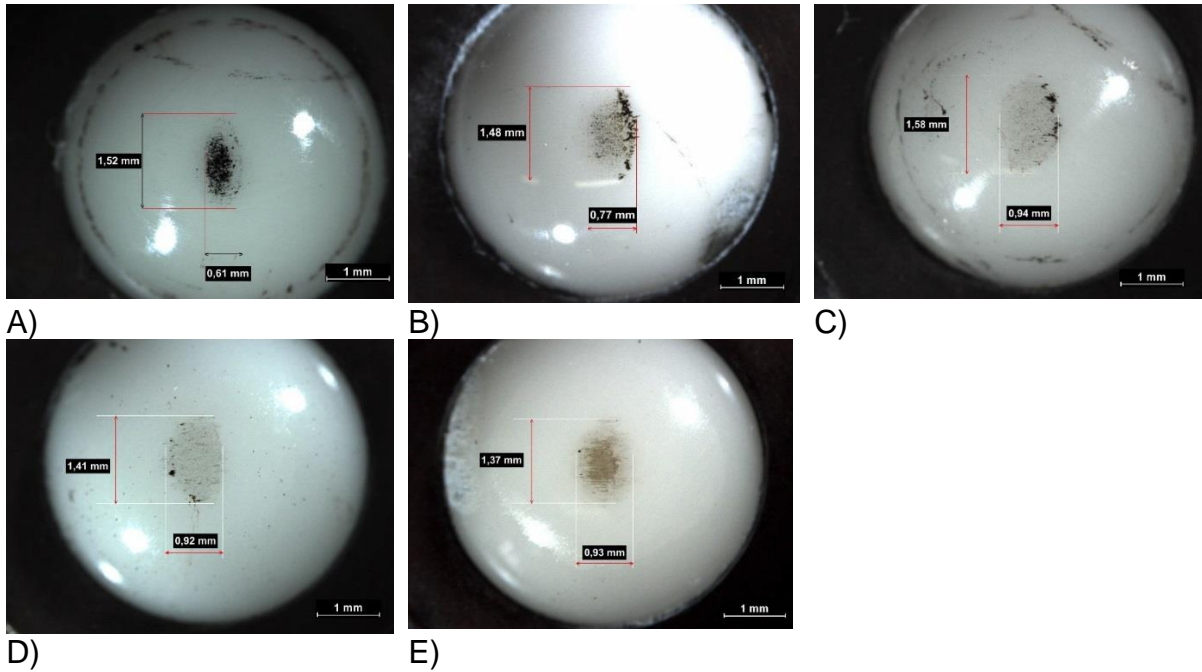
Attachment 51: Wear of the pin from NiCr-Cr$_2$O$_3$ coating at A) 23 °C, B) 200 °C, C) 400 °C, D) 600 °C and E) 750 °C

Element	Weight%	Atomic%
Oxygen	42.64	74.11
Silicon	12.26	12.14
Zirconium	45.10	13.75

Attachment 52: Chemical composition of ZrSiO₄ coating as sprayed done on SEM

Element	Weight%	Atomic%
Oxygen	36.81	69.5
Silicon	12.86	13.83
Zirconium	50.33	16.67

Attachment 53: Chemical composition of ZrSiO₄ coating after wear test at 750 °C (Spectrum 3)

Temperature (°C)	Start μ (1st batch)	Stabilized μ (1st batch)	Start μ (2st batch)	Stabilized μ (2st batch)
23 °C	0.12	0.43	-	-
200 °C	0.31	0.79	0.56	0.82
400 °C	0.46	0.79	0.54	0.81
600 °C	0.54	0.74	0.53	0.76
750 °C	0.53	0.71	0.50	0.78

Attachment 54: Coefficient of friction (μ) for ZrSiO₄ coating at different temperatures

A)

B)

C)

D)

E)
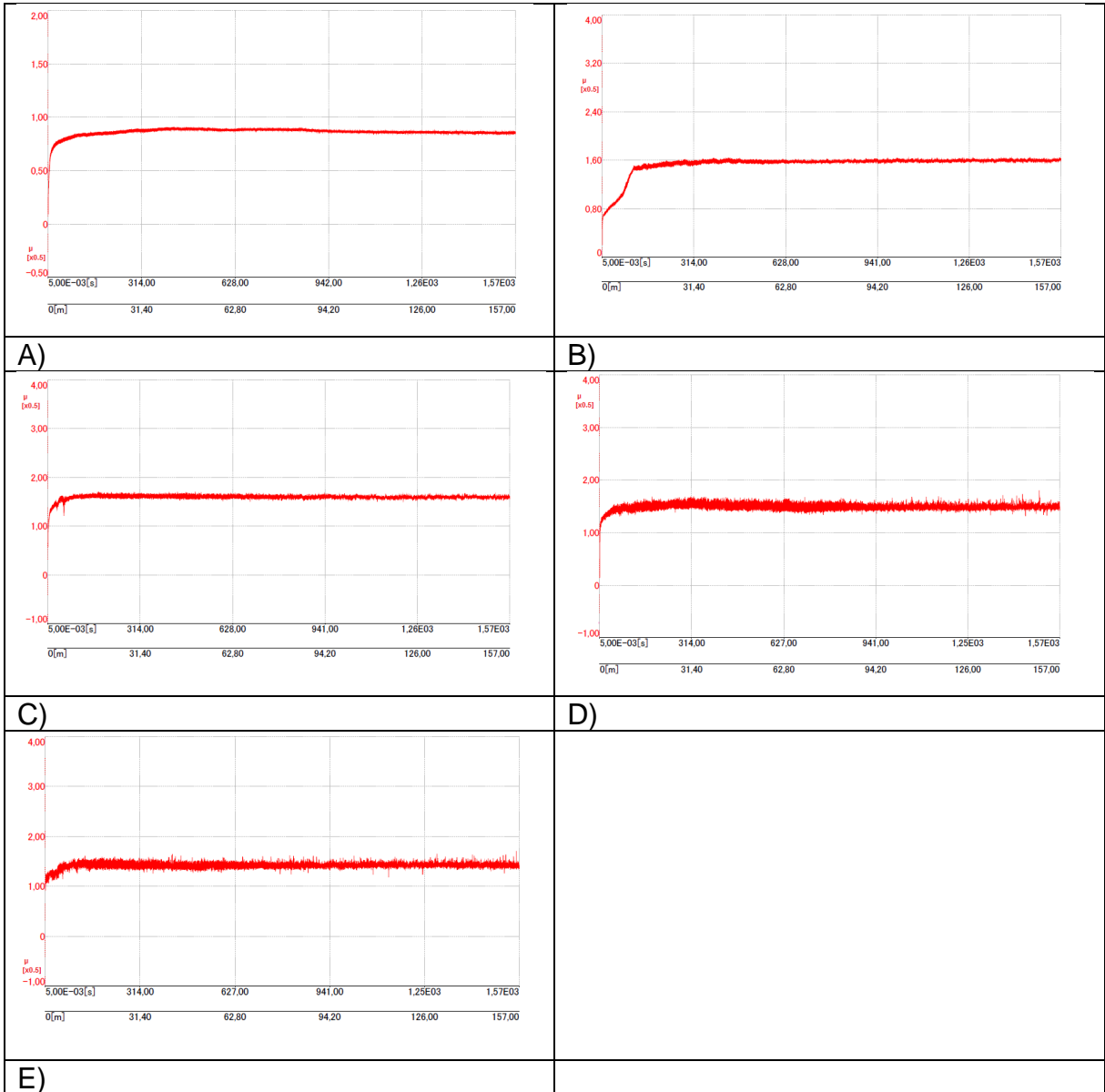
Attachment 55: Friction coefficient of ZrSiO₄ coating (1st batch) at A) 23 °C, B) 200 °C, C) 400 °C, D) 600 °C and E) 750 °C
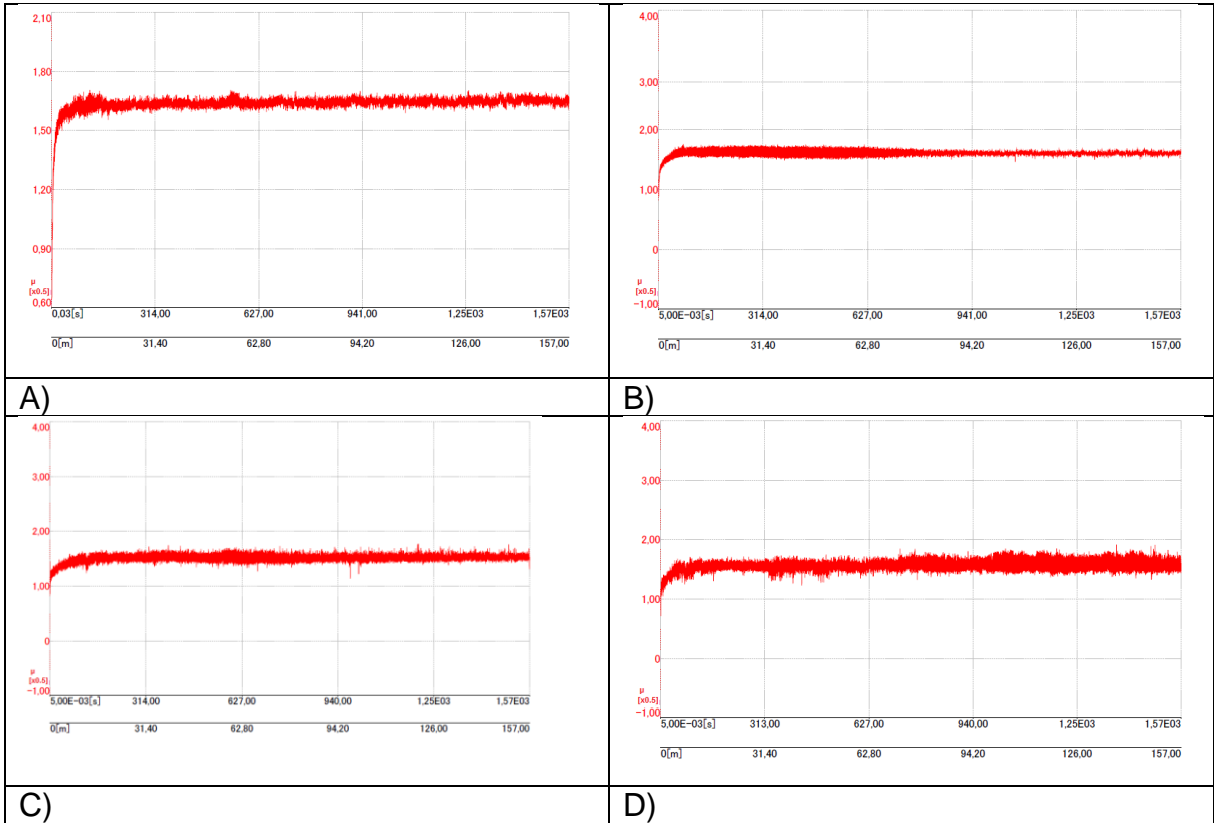
Attachment 56: Friction coefficient of $ZrSiO_4$ coating (2nd batch) at A) 200 °C, B) 400 °C, C) 600 °C and D) 750 °C

ZrSiO₄ (1st batch)			
Temperature	Coating volume loss [mm³]	Specific wear rate K of the coating [10^{-3} mm³/Nm]	Pin volume loss [x 10^{-3} mm³]
23 °C	3.13	3.99	45.31
200 °C	10.17	12.95	119.95
400 °C	15.57	19.83	181.23
600 °C	27.14	34.55	230.42
750 °C	26.2	33.33	263.92

Attachment 57: Coating volume loss, pin volume loss and wear rate of $ZrSiO_4$ at different temperatures (1st batch)

| ZrSiO$_4$ (2st batch)			
Temperature	Coating volume loss [mm^3]	Specific wear rate K of the coating [10^{-3} mm^3/Nm]	Pin volume loss [x 10^{-3} mm^3]
23 °C	-	-	-
200 °C	10.21	12.99	175.20
400 °C	14.22	18.11	189.52
600 °C	26.2	33.35	223.17
750 °C	43.62	55.54	289.21

Attachment 58: Coating volume loss, pin volume loss and the wear rate of ZrSiO$_4$ at different temperatures (2st batch)
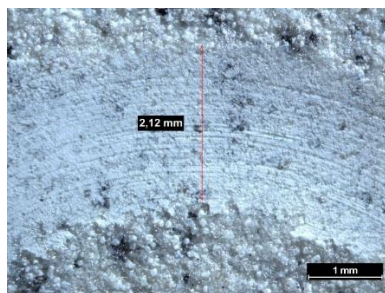
A)
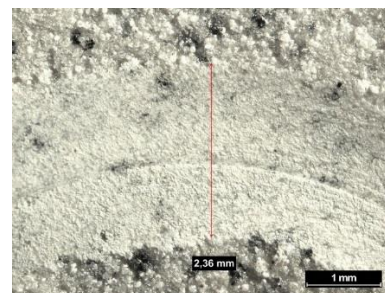
B)
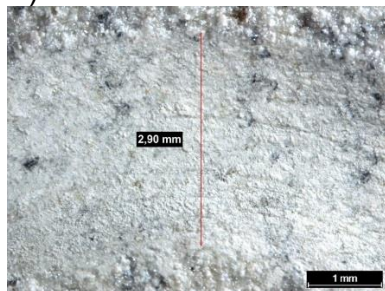
C)

D)

Attachment 59: Wear track of the ZrSiO$_4$ coating (2st batch) at A) 200 °C, B) 400 °C, C) 600 °C and D) 750 °C
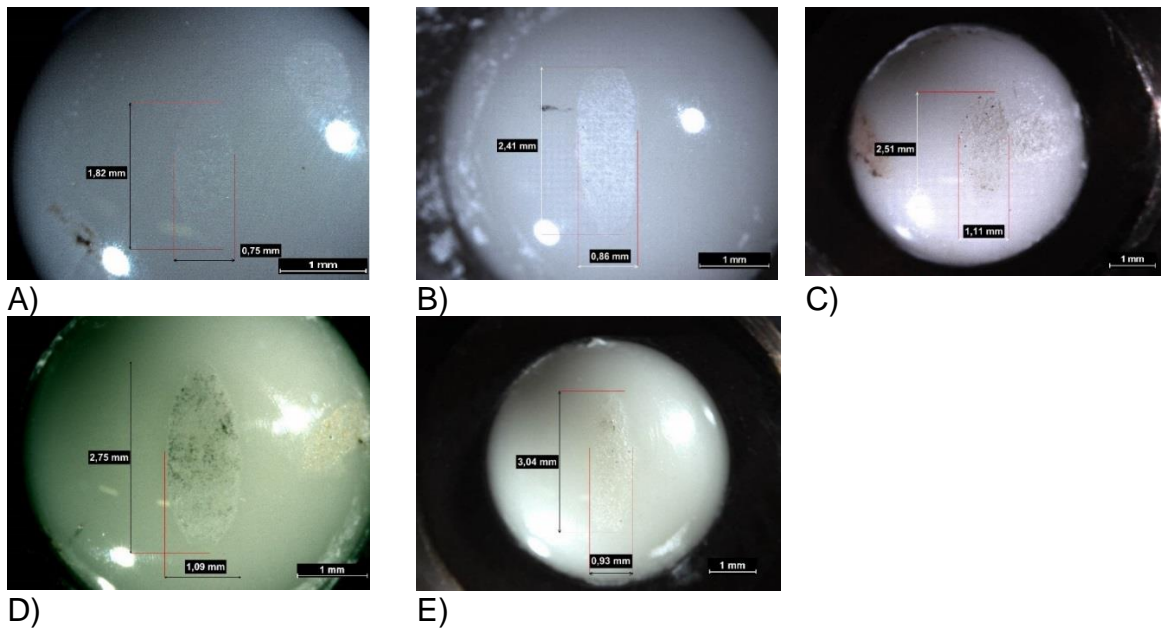
Attachment 60: Wear of the pin from ZrSiO$_4$ coating (1th batch) at A) 23 °C, B) 200 °C, C) 400 °C, D) 600 °C and E) 750 °C
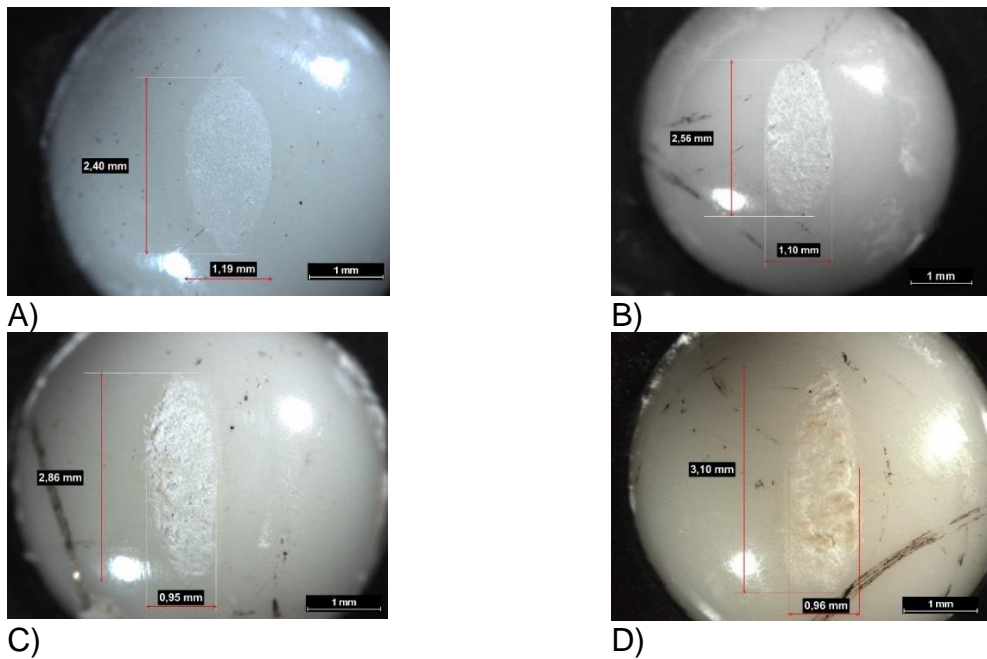
Attachment 61: Wear of the pin from ZrSiO$_4$ coating (2nd batch) at A) 200 °C, B) 400 °C, C) 600 °C

Element	Weight%	Atomic%
Oxygen	39.87	72.44
Silicon	11.63	12.04
Zirconium	41.72	13.30
Yttrium	6.79	2.22

Attachment 62: Chemical composition of ZrSiO$_4$-Y$_2$O$_3$ coating as-sprayed

Element:	Weight%	Atomic%
Oxygen	34.18	69.69
Silicon	8.11	9.42
Yttrium	27.86	10.22
Zirconium	29.85	10.67

Attachment 63: Chemical composition of $ZrSiO_4$-Y_2O_3 coating after wear test at 750 °C

Temperature (°C)	Start μ (1st batch)	Stabilized μ (1st batch)	Start μ (2st batch)	Stabilized μ (2st batch)
23 °C	0.47	0.83	-	-
200 °C	0.21	0.79	0.38	0.84
400 °C	0.46	0.82	0.35	0.83
600 °C	0.52	0.78	0.61	0.81
750 °C	0.58	0.85	0.54	0.77

Attachment 64: Coefficient of friction (μ) for $ZrSiO_4$-Y_2O_3 coating at different temperatures
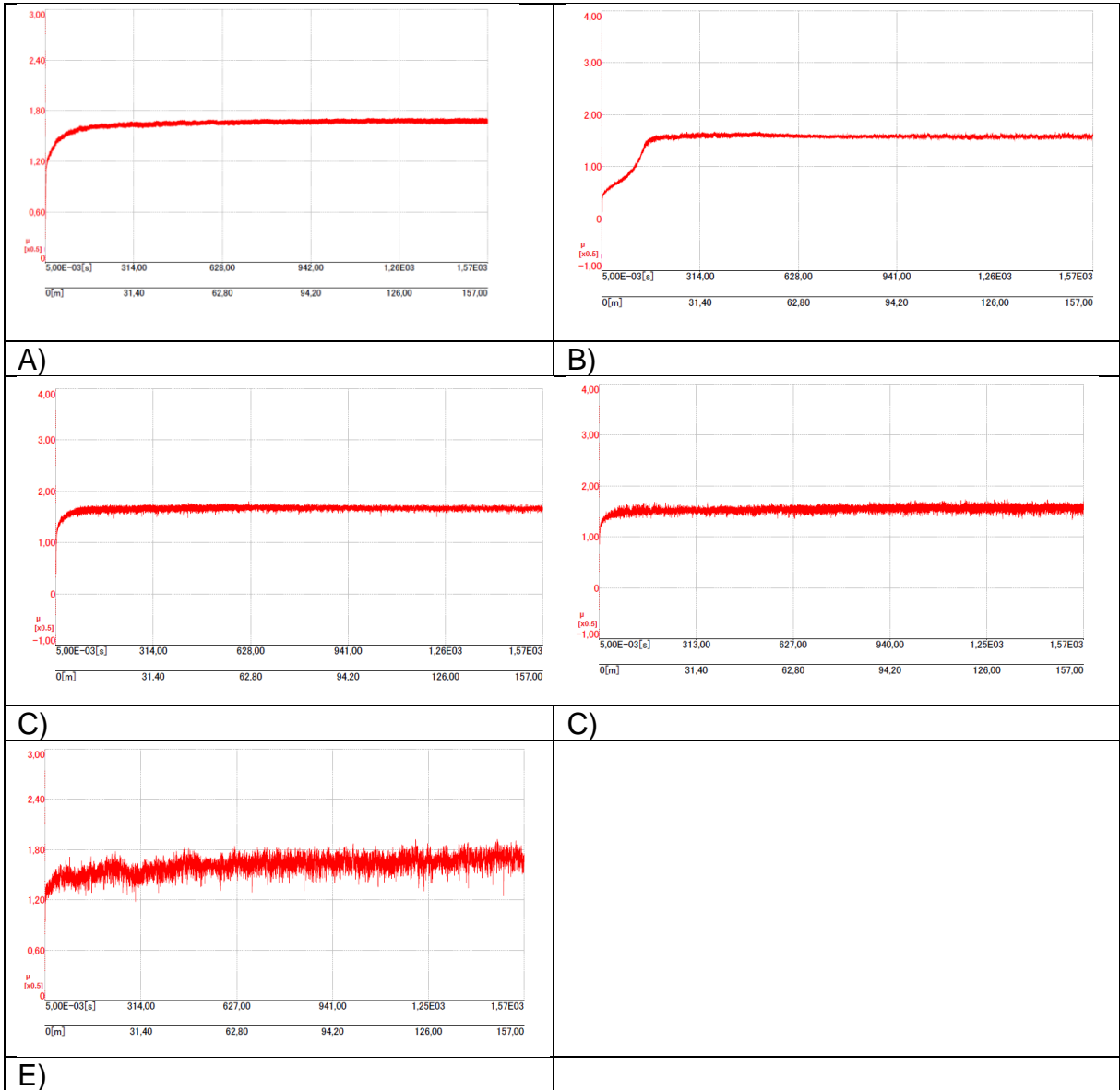
Attachment 65: Friction coefficient of ZrSiO$_4$-Y$_2$O$_3$ coating (1st batch) at A) 23 °C, B) 200 °C, C) 400 °C, D) 600 °C and E) 750 °C
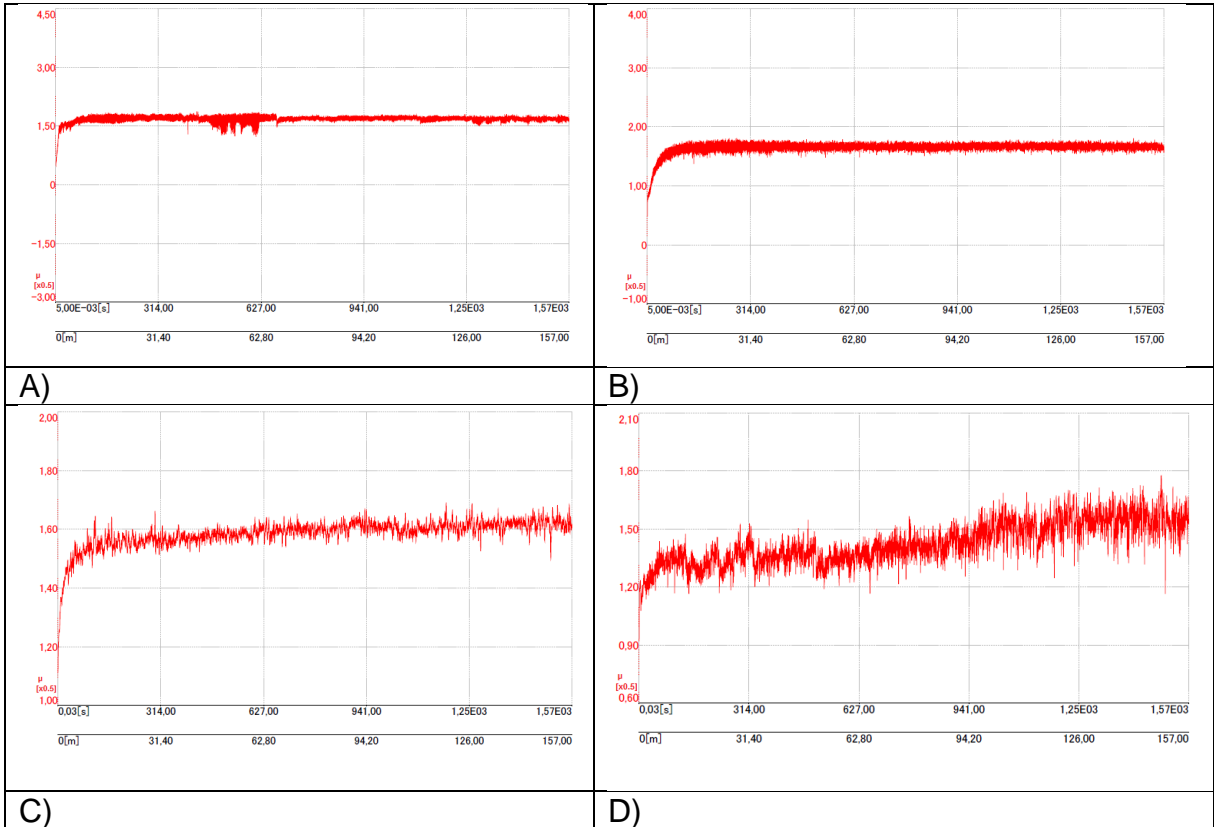
Attachment 66: Friction coefficient of ZrSiO₄-Y₂O₃ coating (batch 2st) at A) 200 °C, B) 400 °C, C) 600 °C and D) 750 °C

ZrSiO₄-Y₂O₃ (1ˢᵗ batch)			
Temperature	Coating volume loss [mm³]	Specific wear rate K of the coating [10⁻³ mm³/Nm]	Pin volume loss [x 10⁻³ mm³]
23 °C	6.07	7.73	41.86
200 °C	14.74	18.77	165.5
400 °C	15	18.58	165.5
600 °C	15.98	20.34	159.88
750 °C	8.18	10.41	90.48

Attachment 67: Coating volume loss, pin volume loss and the wear rate of ZrSiO₄-Y₂O₃ coating at different temperatures (1ˢᵗ batch)

ZrSiO$_4$-Y$_2$O$_3$ (2st batch)			
Temperature	Coating volume loss [mm^3]	Specific wear rate K of the coating [10^{-3} mm^3/Nm]	Pin volume loss [x 10^{-3} mm^3]
23 °C	-	-	-
200 °C	10.24	13.04	159.87
400 °C	17.12	21.80	175.2
600 °C	16.13	20.54	145.59
750 °C	9.62	12.25	112.69

Attachment 68: Coating volume loss, pin volume loss and wear rate of ZrSiO$_4$-Y$_2$O$_3$ at different temperatures (2st batch)
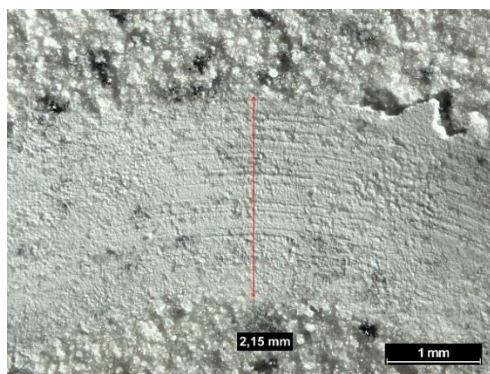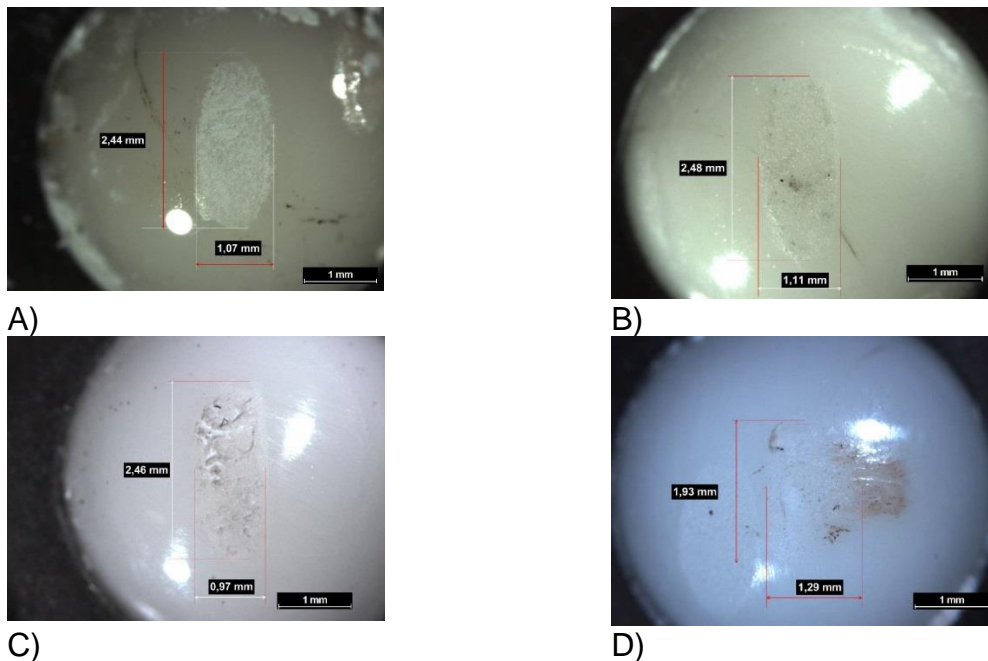

A)

B)
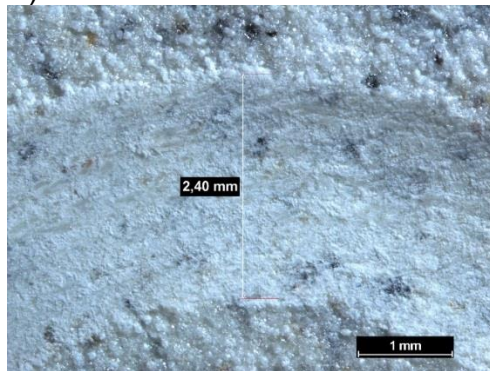
C)

D)

Attachment 69: Wear track of the ZrSiO$_4$-Y$_2$O$_3$ coating (2st batch) at A) 200 °C, C) 400 °C, D) 600 °C and E) 750 °C
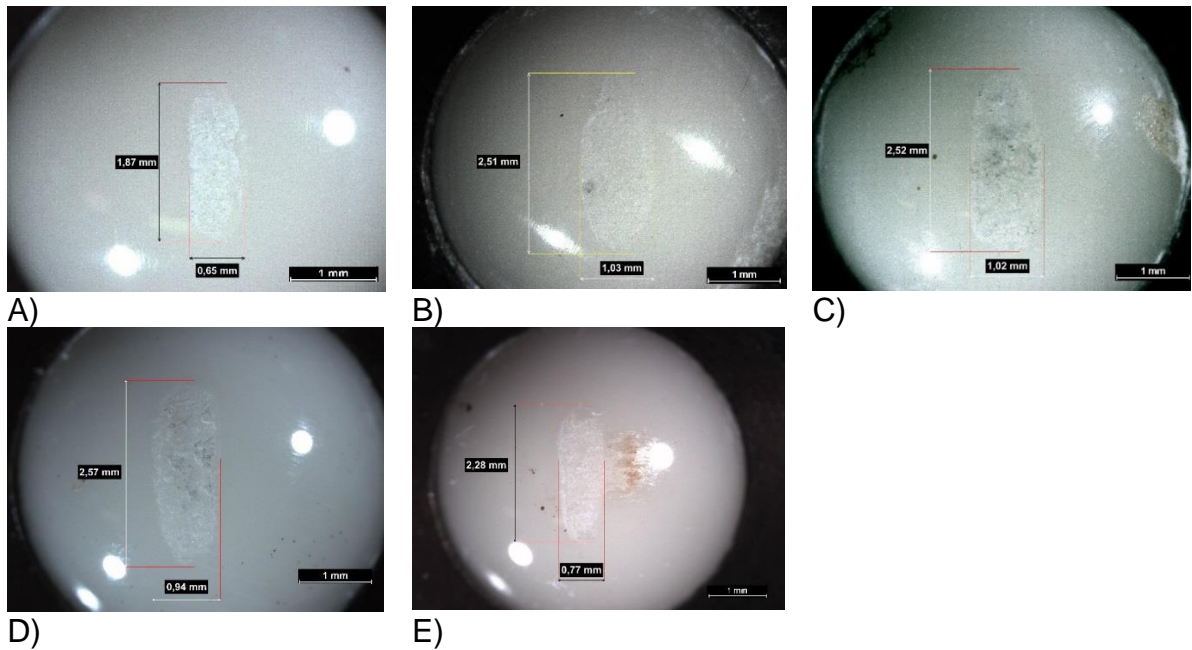
Attachment 70: Wear of the pin from ZrSiO₄-Y₂O₃ coating (batch 1ᵗʰ) at A) 23 °C, B) 200 °C, C) 400 °C, D) 600 °C and E) 750 °C

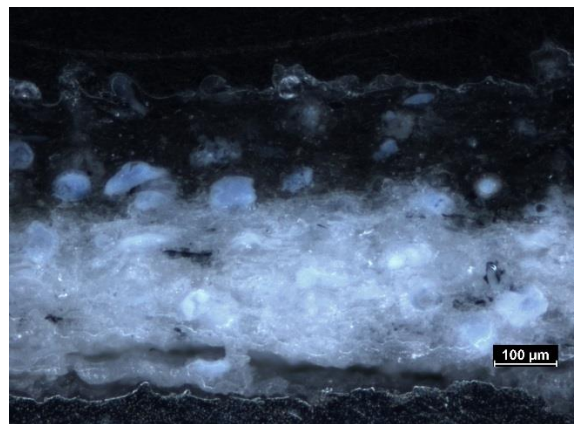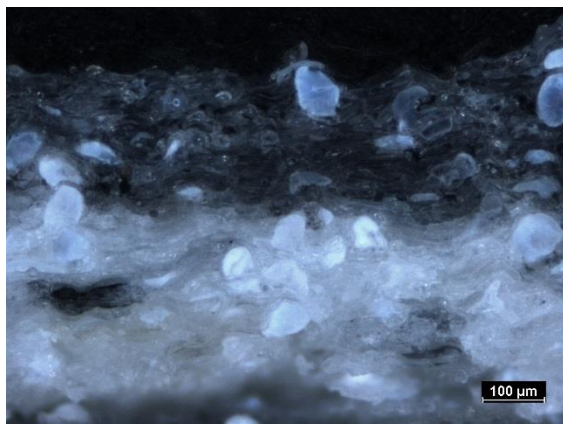*Attachment 71: Wear of the pin from ZrSiO₄-Y₂O₃ coating (batch 2ᵗʰ) at A) 200 °C, B) 400 °C, C) 600 °C and D) 750 °C*

Element	Weight%	Atomic%
Oxygen	17.49	52.16
Silicon	3.18	5.39
Yttrium	70.22	37.68
Zirconium	9.11	4.76

Attachment 72: Chemical composition of ZrSiO₄-Y₂O₃ coating after wear test at 750 °C (Spectrum 2)
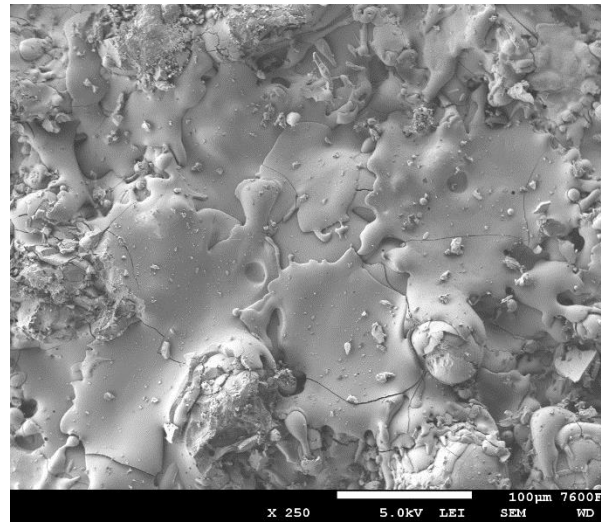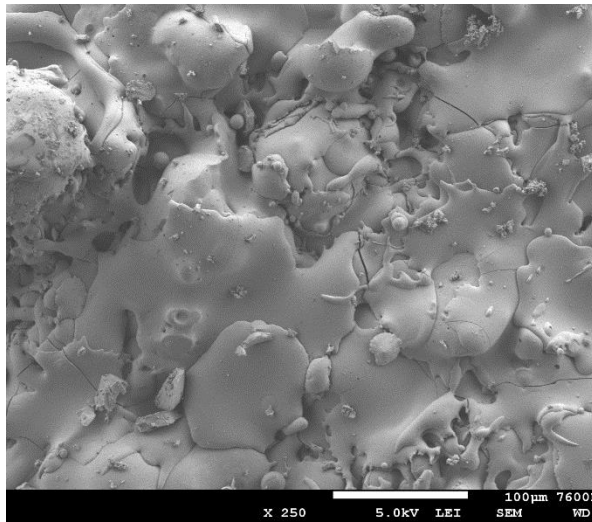
Attachment 73: SEM picture of A) $ZrSiO_4$ and B) $ZrSiO_4$ -Y_2O_3

Attachment 74: Microscopic picture of the structure of A) $ZrSiO_4$ coating and B) $ZrSiO_4$-Y_2O_3 coating